SPIN DEPENDENT SCATTERING IN MAGNETIC MULTILAYERS GROWN BY MBE

Paul Anthony Ryan

Submitted in accordance with the requirements for the degree of
Doctor of Philosophy

University of Leeds
Department of Physics and Astronomy
December 1998

The candidate confirms that the work submitted is his own, and that appropriate credit has been given where reference has been made to the work of others.

Acknowledgements.

I would like to thank everyone who has helped me during my PhD. Thanks to Bryan Hickey for his advice and guidance as my supervisor. Thanks also to Mike Walker for his training on the MBE machine, and to John Turton and all of the technicians in the workshop at Leeds. In addition, thanks must go to past and present members of the Condensed Matter Group in Leeds, for their help and encouragement over the last three years. Much of the work in this thesis has been in collaboration with the Physics Department at Durham University, headed by Brian Tanner. I would like to thank Ian Pape, Tom Hase, Brian Fulthorpe and all of the others members of the group for their hard work and stimulating conversation during the long nights at the Daresbury SRS, and subsequent collaborators meetings.

Finally, I would like to thank my family for their constant support, and most of all to Rachel, for her love, patience and encouragement throughout this PhD.

Abstract.

This thesis presents studies on magnetic multilayers grown by molecular beam epitaxy (MBE). The interface morphology of Co/Cu(111) has been investigated using a variety of x-ray scattering techniques. The interface structure was varied between samples by altering the deposition temperatures of the buffer layer and multilayer. The low angle specular and diffuse scatter has been simulated using a simulation program based on the distorted wave Born Approximation, available from Bede Scientific [1]. The parameters extracted from these simulations have been compared to those obtained from the simulations of high angle diffraction scans, and the trends in the structural parameters compared to trends in the giant magnetoresistance (GMR). The roughness at the interface was highly correlated, and the magnitude of the correlated component of the roughness was inversely proportional to the GMR. Two length-scales were found in the majority of the samples, and changes in the magnitudes of these length-scales correlated with changes in the deposition temperatures.

A study of Fe/Au(100) and (111) multilayers was undertaken to investigate the effect of the crystal orientation on the GMR. Oscillations were present in the AF-coupling in the (100) orientation, but not observed in the (111). The oscillation periods of 15±2Å and 7±2Å are in good agreement with previously published results by others. The GMR and saturation conductivity of the (100) were higher than that of the (111) multilayers. This can be explained in terms of electron channelling. Fe/Au(100) is a candidate for electron channelling, where there is a quantum confinement of an electron spin channel when the magnetic layers in the multilayer are in the ferromagnetic alignment, and no such confinement in the anti-parallel state. Fe/Au(111) should not exhibit this phenomenon. An x-ray characterisation was undertaken to confirm that the enhancements in the GMR and conductivity was not due to increased interface roughness, poor epitaxial growth or defects in the (111) multilayers. The interface roughness was found to be three times greater in the (100), and the Au spacer layers were of comparable quality in both orientations.

Contents.

List of Figures.

List of Tables.

Abbreviations.

Listed below are common abbreviations and symbols used in the text. Any exceptions to this usage are indicated locally in the text.

Å	Angstrom (10^{-10}m)
AF	anti-ferromagnetic
BA	Born Approximation
bcc	body-centred cubic
$C(R)$	height-height correlation function
d	interplanar spacing
DWBA	distorted wave Born Approximation
f	atomic form factor
f', f''	anomalous scattering factors
fcc	face-centred cubic
FWHM	full width half maximum
GMR	giant magnetoresistance
H	applied magnetic field
h	roughness exponent
I	intensity
M	magnetisation
MBE	molecular beam epitaxy
ML	monolayer
n	refractive index
$\boldsymbol{q}$	scattering vector
R	reflectivity
RHEED	reflection high energy electron diffraction
RKKY interaction	Ruderman-Kittel-Kasuya-Yosida interaction
rms	root-mean-square
T	Tesla
t	thickness
β	absorption
δ	dispersion
Λ_B	bilayer periodicity
λ	wavelength
θ	sample angle in specular scan
θ_c	critical angle
2θ	detector angle
ρ_o	resistivity in zero field
ρ_s	resistivity in saturation field
σ	interfacial roughness
σ_c	correlated roughness
σ_u	uncorrelated roughness
ω	sample angle in transverse diffuse scans
ξ	lateral correlation length of interfacial roughness

Publications.

The relation of structure to giant magnetoresistance in Co/Cu multilayers.
T.P.A. Hase, I. Pape, B.K. Tanner, H. Laidler, **P. Ryan** and B.J. Hickey.
J. Magn. Magn. Mater. **177-181**, (1998) 1164-1165.

Determination of the copper layer thickness in spin valves by grazing incidence x-ray fluorescence.
T.P.A. Hase, B.K. Tanner, **P. Ryan**, C.H. Marrows and B.J. Hickey.
IEEE Trans. Mag. **34**, (1998) 831-833.

Experimental Evidence for Electron Channelling in Fe/Au(100) Multilayers.
P.A. Ryan, B.D. Fulthorpe, D.T. Dekadjevi, B.K. Tanner and B.J. Hickey.
Submitted to Nature, 1998.

Chapter 1: Introduction.

The physical properties of thin magnetic films and multilayers have been under investigation for many years. The nature of the interaction between magnetic layers, separated by a non-magnetic spacer, was one of the topics under investigation. The magnetic layers always appeared to be ferromagnetically coupled, irrespective of the thickness of the spacer layer. However, as the growth of thin films improved, the thickness and number of defects within a layer became more controllable. With these improvements, the interaction between magnetic layers was observed to be anti-ferromagnetic (AF) in Gd/Y multilayers in 1986 [2]. Subsequently, this led to the discovery of the Giant Magnetoresistance effect (GMR) in 1988 [3], which is defined as

$$GMR = \frac{\rho_o - \rho_s}{\rho_s} \quad \text{..... (1.1)}$$

where ρ_o and ρ_s are the resistivities in zero and saturation field respectively. This was quickly identified as being due to spin-dependent scattering of electrons within the multilayer. It is now generally agreed that the majority of electron scattering occurs at the interfaces within the multilayer, and that this scattering is spin-dependent [4].

GMR materials are of great technological importance. They are used in the new generation of hard disk drive read heads [5]. In a storage medium, such as a magnetic disk, the information is stored using alternate bits magnetised in opposite directions (either longitudinally or perpendicular). The information is read back by detecting the stray fields from these magnetised regions. The GMR head responds directly to the field, unlike a conventional inductive head, by exhibiting a change in resistance proportional to the magnitude of the field. This enables the density of data to be constant over the whole of the disk, increasing the storage density.

Another application being investigated is the use of a GMR device as MRAM (magnetic random access memory). These would offer a non-volatile system with very high storage densities, as the limitation of one transistor per cell in the current memory technologies does not apply.

As the resistance change in the GMR devices is field-dependent, there are many other applications in the magnetic sensors industry [6]. GMR devices are being introduced into ABS braking systems, traction control, magnetic switches and isolators.

Two predominant growth procedures currently used in the manufacture of magnetic multilayers are magnetron sputtering and Molecular Beam Epitaxy (MBE). The sputtered samples are grown at a faster rate than the MBE samples, but in a higher deposition pressure. Sputtered samples tend to have some texture, but do not generally exhibit a high crystal orientation. MBE samples are generally thought to be of high crystalline quality.

Sputtered samples are grown at fast deposition rates, typically 1-2Å/s, in a base pressure of 10^{-7} Torr, but growth pressure of 10^{-4} Torr. Due to the energetic nature of the growth, the interfaces are normally very flat, with an rms roughness of approximately 2Å, and a typical GMR of 80% at low temperature in Co/Cu multilayers with 20 repeats [7].

However, this growth method normally produces samples of a preferred texture, but not of good crystal orientation.

MBE samples are grown at a much slower rate than the sputtered. Growth rates are typically 0.2Å/s, in a pressure of 10^{-11} Torr. The samples are of high epitaxial quality because of this low deposition rate and pressure. This leads to rough interfaces with an rms roughness of approximately 4-10Å, dependant on the materials, deposition conditions and the substrate used. These multilayers produce substantially lower GMR values than of sputtered multilayers, with the MBE-grown samples not normally exceeding 50% at low temperatures [8]. However, growth conditions can be varied to produce structural differences between multilayers. With the use of different substrates, the crystal orientation of multilayers can be varied and its dependence on the GMR studied.

1.2. Aims of this Thesis.

This thesis investigates the importance of the interface morphology in GMR materials. There are two parts to this investigation: (i) the effect of interface roughness on the GMR, and (ii) the role of specular reflections of electrons at the interfaces within the multilayer. To provide samples with different interface roughness, and of different orientations, the multilayers were all prepared by MBE.

The first part of this thesis investigates the effect of interface morphology on the GMR in Co/Cu(111) multilayers grown by MBE onto epi-polished sapphire $(11\bar{2}0)$ substrates. Co/Cu multilayers were chosen as they exhibit large GMR values, thus changes in the GMR due to structure are more readily observed. In addition to this, Co/Cu is a well-known immiscible system below temperatures of approximately 400°C. More specifically, the bulk solubility for Cu into Co at 422°C is 0.4% [9], so Co and Cu do not form intermetallic compounds at interfaces.

In the bulk form, fcc Co has a lattice parameter of 3.5447Å and Cu has the lattice parameter 3.6150Å. If Cu and Co (111) planes are stacked along the fcc [111] direction, the in-plane misfit is 1.9%. This allows Co and Cu to have pseudomorphic growth and coherent interfaces, with compression of the Cu and expansion of the Co lattice. The low temperature equilibrium structure of bulk Co is hcp, but complete fcc stacking of thin Co layers in Co/Cu multilayers is normally observed [10].

The temperature of the substrate during the deposition of the multilayer was varied to change the interface structure, and the transport and magnetic properties were measured. Low and high angle x-ray scattering was then utilised to determine the structure and interface morphology of the multilayers. In previous studies of the interface morphology using x-ray scatter, only the specular scatter has been considered. However, the presence of other layers in the superlattice, for example buffer and capping layers, can cause changes in the specular scatter which may be interpreted as changes in the multilayer structure. Safa and Tanner [11] have shown that the height of the multilayer Bragg peak, normally thought to be a measure of the roughness at the interface within the multilayer, can be altered by the thickness of a Au capping layer. Therefore, diffuse scatter must also be considered to obtain reliable values of the roughness at interfaces.

The specular and diffuse scatter at low angles was simulated to obtain information about the interface morphology. In addition to this, the high angle diffraction was simulated, by H. Laidler and D. Dekadjevi at the University of Leeds, to obtain information relating to the thickness of the individual layers. The resulting structural parameters were then related to the transport and magnetic results.

The second part of the thesis concerns the effect of the crystal orientation on the transport properties of multilayers. In 1992, Hood and Falicov [12] first introduced the possibility that an electron may reflect from an interface within a magnetic multilayer with no change in the component of momentum in the plane of the sample, a so-called specular reflection. This reflection had been observed for many years at the metal / vacuum interface in single films of noble metals [13]. If an electron can reflect at both interfaces of a layer, it may be confined to that layer. This confinement, often called electron channelling, is of great importance in any system of dimensions on the nanometre scale. Stiles [14] calculated the reflection coefficients of electrons at the interface between combinations of magnetic and non-magnetic metals, and showed that these reflection coefficients are dependent on the crystalline orientation of the interface. For certain systems, there is a spin-asymmetry in the reflection coefficients, with only one spin having a high probability of being reflected at the interface. If the moments of the ferromagnetic layers are aligned anti-parallel, each spin of the electrons will only be reflected at one interface within the layer. The conductivity of the multilayer is then the average of the conductivities of the two spin channels. However, in the ferromagnetic alignment, one spin of the electrons will have a high probability of reflection at both interfaces within the layer, leading to a spin-channel of electrons being confined to that layer. This confinement leads to a GMR if the electrons are confined to a layer of low resistivity. A further consequence of electron channelling is an enhancement of the saturated conductivity.

A good candidate for electron channelling is Fe/Au(100), whereas the (111) orientation of these multilayers is not expected to exhibit electron channelling. To investigate whether electron channelling was present in Fe/Au(100) multilayers, the GMR and saturated conductivity of the two orientations of multilayers was studied as a function of Au spacer thickness. The interface morphology and the structure of the individual layers within the multilayer were determined by utilising x-ray scattering to attempt to explain any changes in electron transport properties between orientations.

1.3. Characterisation Techniques.

All of the samples studied in this thesis were grown in the VG-80 MBE machine at the University of Leeds. Several characterisation techniques have been employed to study electron transport, magnetic and structural properties of these multilayers. The low temperature GMR and resistivity was measured in a Thor cryostat, and the magnetic characterisation was carried out using room temperature MOKE (magneto-optical Kerr effect), both at the University of Leeds. The structure was investigated using x-ray techniques at the University of Leeds, Station 2.3 at the Daresbury SRS and BM16.3 at the ESRF, Grenoble. These x-ray studies were carried out in collaboration with Prof. B.K. Tanner's group at Durham University.

The interface morphology was investigated using grazing incidence x-ray scattering. If only the specular scatter is considered, information about the interface morphology is

limited to the total interface width, and this may be confused by other layers present in the sample. By analysing the diffuse scatter in addition to the specular scatter, the degree of lateral correlation and the length-scale of the roughness can be extracted. The specular and diffuse scans were simulated using commercially available software, based on the distorted wave Born Approximation, from Bede Scientific [1]. These simulations gave values for the correlated and uncorrelated components of the roughness, the lateral correlation length and the roughness exponent within the multilayer.

The grazing incidence geometry is sensitive to changing electron density gradients. It is used to study the interface morphology but provides no information concerning the crystallinity of the multilayers. To obtain this information, high angle diffraction scans were carried out on the multilayers. These scans provide information about the thickness of individual layers, strain within the multilayer, and the crystalline quality of the layers. Transverse diffuse scans at high angle were also carried out to obtain information about the lateral structure of the multilayer.

1.4. Structure of the Thesis.

Chapter 2 describes the theory and experimental details of x-ray scattering. The theory behind routine x-ray characterisation is discussed, along with the more specialised theories behind the simulation software throughout this study. The practical details of the simulation software are also examined, with illustrations of the effects of varying the parameters within the software on the resulting simulation. The experimental details of the diffractometer at the University of Leeds, and Station 2.3 at the Daresbury SRS are outlined. Routine characterisation was carried out at the University of Leeds, and more in-depth studies were feasible the Daresbury SRS, due to the properties of synchrotron radiation. These properties include increased intensity, the high degree of beam collimation, and the tuneable wavelength that enables the anomalous dispersion effect to be employed.

The GMR and magnetisation are discussed in chapter 3. Theories derived to explain the GMR are outlined, and the concept of electron channelling is introduced. The cryostat used to measure the transport properties at low temperature is described, along with the MOKE apparatus.

In chapter 4, the effect of the interface morphology on the GMR in Co/Cu(111) multilayers is investigated. The specular and diffuse x-ray scattering is simulated to extract the structural parameters relating to the interface morphology. These parameters are then compared to the transport results to obtain the important parameters in the optimisation of the GMR.

Chapter 5 describes a characterisation study of two orientations of Fe/Au multilayers. Due to the difference between the reflection coefficients, as predicted by M.D. Stiles, Fe/Au(100) is a good candidate to exhibit electron channelling whereas Fe/Au(111) is not. Evidence for electron channelling was sought by studying differences in the transport properties between orientations. The GMR, resistivity and MOKE in each orientation were measured as a function of spacer thickness. The crystallinity and interface morphology was investigated, using x-ray diffraction and reflectivity respectively. It was thus possible to compare the epitaxial quality of the different

orientations, to determine whether the transport properties were affected by the quality of the multilayer.

Finally, chapter 6 summarises the main conclusions reached, and outlines plans for further work.

Chapter 2: Theory and Methods of X-ray Characterisation.

2.1. Introduction.

X-ray characterisation has become an important tool in determining the structure of thin films and magnetic multilayers. However, until recently only the specular scatter had been considered, with the result that merely the thickness and total interface width of buried layers could be determined. In the last few years, the diffuse scatter has been utilised making it possible to extract more information about the structure and interface morphology of multilayers. These techniques have been applied to determine the interface morphology of multilayers, to attempt to resolve the role of interfaces on the magneto-transport properties in magnetic multilayers

This chapter is organised as follows. It introduces the basic x-ray reflectivity and diffraction theory, and how these are routinely used to characterise samples in a basic manner. An overview of more advanced characterisation methods is given, where the diffuse scatter from multilayers is utilised. The experimental apparatus used to undertake these measurements is described, at both the University of Leeds and Station 2.3 at Daresbury SRS. The modelling of the reflectivity data is discussed, with an overview of the theory involved in the simulation software used. A systematic variation of the fitting parameters used in the simulation software is shown, to illustrate a strategy that can be used to determine the structure of a multilayer by simulating the specular and diffuse scatter.

2.2. Bragg's Law.

The use of x-ray diffraction and reflectivity are standard tools in the basic characterisation of magnetic multilayers, to compare the thickness and orientation of samples with those expected from the growth. The scattering of the x-rays is a two-step process; (i) the x-rays are scattered by the electrons present in the sample, and (ii) these scattered x-rays then interfere to produce peaks in the x-ray scan. The position of the peaks can be predicted by Bragg's Law

$$2d\sin\theta = n\lambda \quad \text{..... (2.1)}$$

where d is the interplanar spacing, λ the x-ray wavelength, n the diffraction order and θ the scattering angle. In reciprocal space, this can be written [15] as

$$\Delta \boldsymbol{K} = \boldsymbol{G} \quad \text{..... (2.2)}$$

where $\Delta \boldsymbol{K} = \boldsymbol{K}_o - \boldsymbol{K}_1$ is the scattering vector, and $\mathbf{G} = h\mathbf{i} + k\mathbf{j} + l\mathbf{k}$, the reciprocal lattice vector. The given reflection can be labelled by the Miller indices (h,k,l). Not all planes give rise to reflections, as the position and scattering factor of the atoms within the unit cell must be considered. The intensity is proportional to the square of the structure factor of the reflection, F_{hkl}, where

$$F_{hkl} = \sum_{1}^{N} f_n \exp\left(2\pi i \mathbf{G}.\mathbf{r_n}\right) \quad \text{..... (2.3)}$$

f_n is the atomic form factor, and r_n is the position of the *nth* atom in the unit cell. The summation is over N atoms within the unit cell.

For a diffraction profile of a multilayer, the zero-order diffraction peak corresponds to a *d*-spacing which is a weighted averaged of the lattice parameters of the magnetic and non-magnetic layers, the weighting factor corresponding to the relative thicknesses in the bilayer. However, in a multilayer there is a further periodicity present, that of the bilayer repeat Λ_B. This is equivalent to another unit cell being present in the growth direction, with an increased size corresponding to that of the periodicity of the multilayer. Therefore, there are additional reciprocal lattice points present due to this periodicity, and these points are separated by $2\pi/\Lambda_B$ Å^{-1}. These additional points are seen as satellite reflections in the diffraction scan, as illustrated in Figure 2.1.

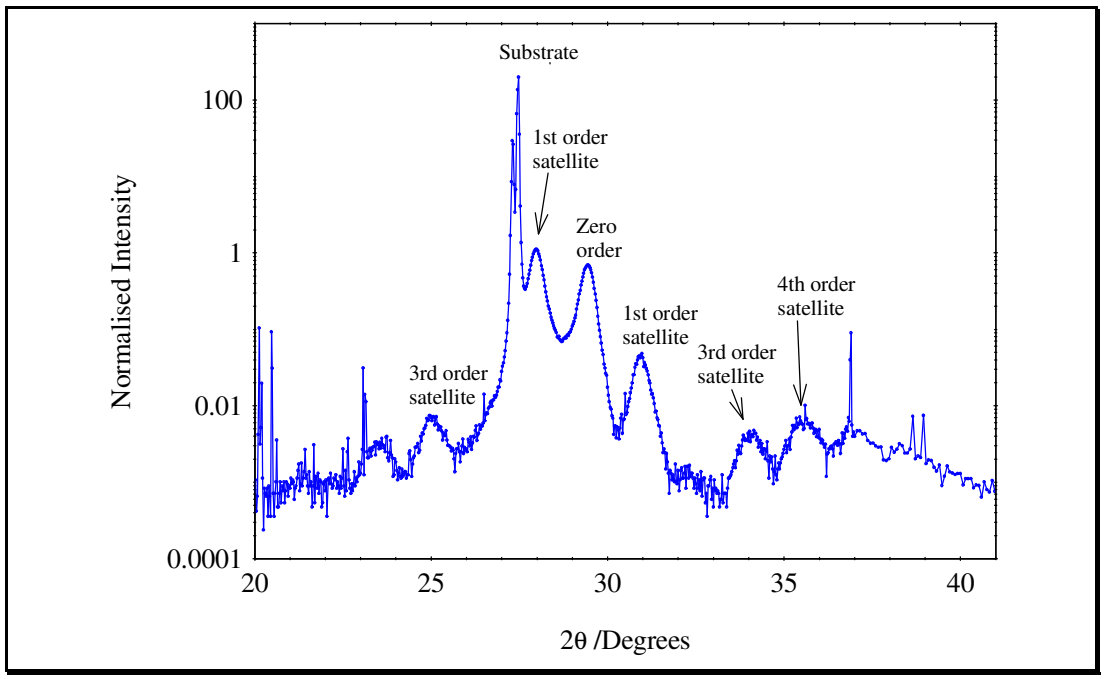

Figure 2.1: Diffraction profile of a (Fe10Å/Au30Å)$_{20}$ multilayer illustrating the zero order multilayer peak and satellites.

The bilayer thickness can also be determined from grazing incidence measurements. At these small angles, surface effects are important, so the x-rays are subject to Snell's law. The refractive index of x-rays in metals is just below unity, and is often written in the form

$$n = 1 - \delta - i\beta \quad \text{..... (2.4)}$$

where δ is related to the quantum mechanical dispersion and β to the absorption of the medium. δ depends on the wavelength of the incident radiation and the electron density of the surface layer. As the refractive index is less than unity, at grazing incidence the x-rays are externally reflected. Neglecting absorption within the sample, the critical angle, θ_c, at which the x-rays start to penetrate the top surface, is given by [16]

$$\theta_c = \sqrt{2\delta} \quad \text{..... (2.5)}$$

The bilayer repeat within the multilayer can act as a pseudo-crystal, and give rise to a diffraction peak in the low angle reflectivity, as seen in Figure 2.2. However, at grazing incidence refraction of the x-ray beam will occur within the sample so a correction to Bragg's Law must be made. The corrected form is [17]

$$\sin^2\theta = \left(\frac{n\lambda}{2\Lambda_B}\right)^2 + 2\delta \quad \text{..... (2.6)}$$

Fringes are also seen in the fall-off of the low-angle scan (Figure 2.2). These are known as Kiessig fringes, and are an interference effect between the waves reflected from the top surface of the multilayer and the multilayer / substrate interface. The position of these fringes is given by [18]

$$\theta_m^2 = (m+k)^2\left(\frac{\lambda}{2t}\right)^2 + 2\delta \quad \text{..... (2.7)}$$

where t is the total thickness, m is the order of the fringe maximum and $k = 1/2$ for constructive interference, to account for a change of phase on reflection at the film/substrate interface. These fringes are routinely used to check the thickness of samples after growth, and to obtain thickness calibration factors for the different materials within the MBE machine to ensure that the correct layer thickness can be deposited.

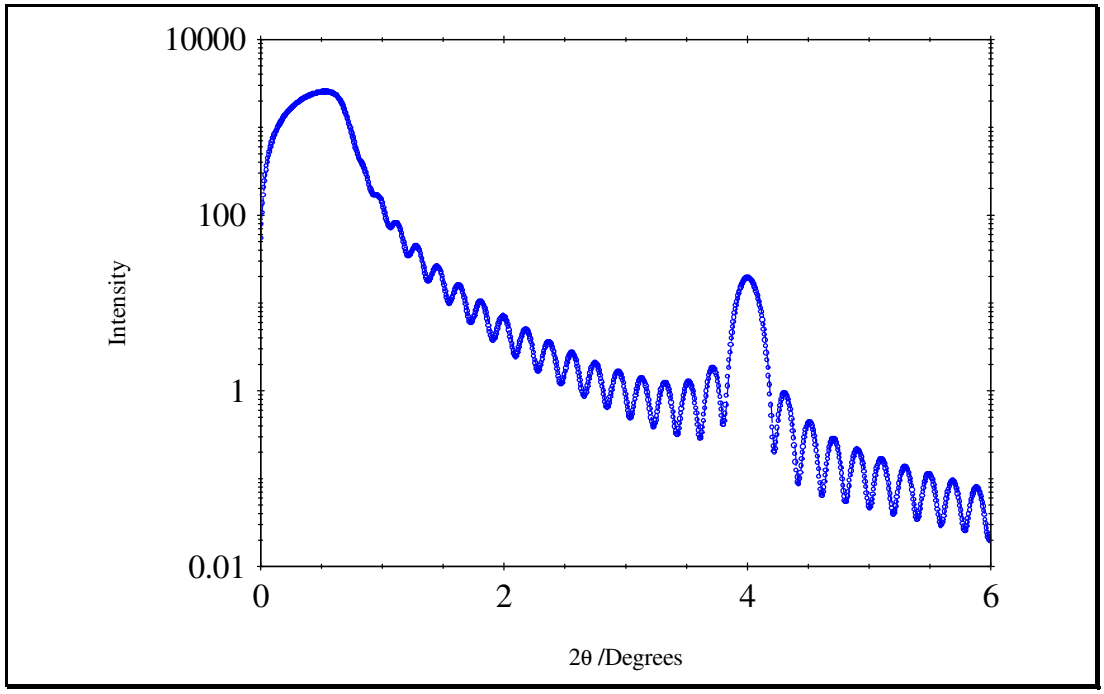

Figure 2.2: Low angle reflectivity simulation of a {Co(12Å)/Cu(8Å)}$_{20}$ multilayer, illustrating the Bragg diffraction peak and Kiessig fringes.

Fringes are sometimes observed between satellites in the high angle diffraction data. Although these are often referred to as thickness fringes, they are only related to the number of bilayers present in the multilayer, not the total film thickness. For a multilayer there will be *N-2* fringes between satellites, where *N* is the number of bilayers present.

The damping of the Kiessig fringes and the height of the Bragg peak are very sensitive to roughness present at the interfaces. The total roughness at each interface can be split into three components, which are outlined below.

2.2.1. Types of Roughness Present in Magnetic Multilayers.

At low angles of incidence, the height distribution along the growth direction and the lateral distribution of the roughness can be investigated. The height distribution is

assumed to be a Gaussian distribution of the interface height from a plane. The roughness is defined as the rms value of this distribution. The lateral distribution is defined by a height-height correlation function, which relates the the heights of two points on the same surface. The height distribution occurs due to different types of disorder present at the interface. For small angles of incidence ($2\theta < 15°$) the length-scale probed by the x-rays is of the order of 2000Å [19]. Disorder on this length scale can be separated into two main classes: interdiffusion and geometrical roughness.

Interdiffusion, often called graded roughness, is a measure of the amount of mixing of the two metals at the interface and manifests itself as a gradient in the electron density at the interface [20]. This does not cause scattering into the diffuse, so technically it is not a roughness. However, it causes a change in phase of the x-rays, leading to destructive interference and hence a reduction in the scattered intensity.

Geometrical roughness can be separated into correlated and uncorrelated components. These components describe the nature of the propagation of the roughness between interfaces in a multilayer. Correlated roughness is where the spacial frequencies of the roughness are replicated from interface to interface throughout the multilayer. It is normally considered to be low frequency roughness, and is shown schematically in Figure 2.3. Uncorrelated roughness is not replicated through the stack of the multilayer, but is a random roughness, normally of a high spacial frequency.

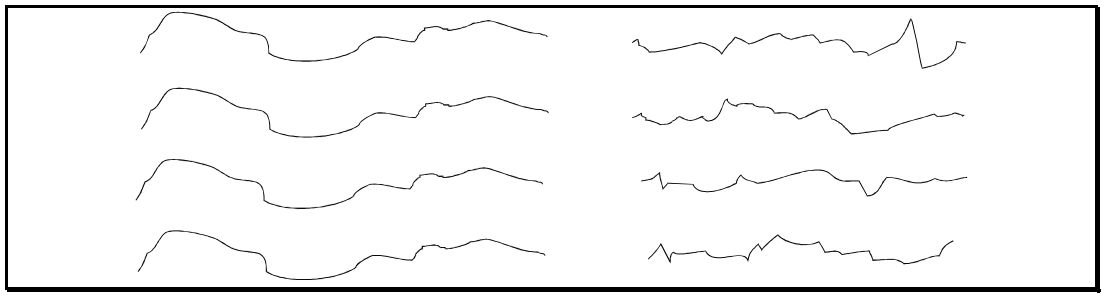

Figure 2.3: A schematic comparison between correlated (left) and uncorrelated (right) roughness.

The components of the roughness can be determined from the diffuse scatter obtained from the multilayers, as detailed later in this chapter.

High angle diffraction and diffuse scatter can be utilised to investigate crystaline quality and the average grain size within multilayers. These can have an effect on the transport properties of multilayers due to electron scattering from defects and grain boundaries. The grain size can be measured from the FWHM of diffuse rocking curves at high angles. The crystalline quality of multilayers is harder to quantify, as a direct measure of the number of defects present within a layer is not possible, but a qualitative comparison between samples is possible from the height and width of the peaks in the high angle diffraction scans.

2.2.2. Anomalous Dispersion.

The scattering contrast between materials in a multilayer is proportional to the difference in the scattering factors. Away from any absorption edges, the scattering factor is approximately the atomic number, *Z*. Therefore, for a Co/Cu system, the difference in the scattering factors is very small. To enhance this scattering difference, the incident energy is tuned to the absorption edge of one of the elements within the multilayer. These absorption edges for x-rays are found at the excitation energies of the

electrons in the K or L shells. This effect, called the anomalous scattering effect, was discussed by Waseda [21] and demonstrated on Fe/Mn superlattices by Nakayama *et al* [22].

At wavelengths close to, and at, the absorption edge, the scattering is increased and there is a change of phase in the scattering. The scattering factor can be treated as complex

$$f = Z + f' + if'' \quad \text{..... (2.8)}$$

where *f'* and *f''* are known as the dispersion corrections. Figure 2.4 illustrates the wavelength dependence of the dispersion corrections for Cu, and the difference between the scattering factors of Co and Cu as a function of wavelength. Away from any absorption edge, there is little difference between the Co and Cu. Close to the absorption edge, *f* is greatly altered and now the difference in the scattering factors between the elements is large, enabling the interface morphology of the Co/Cu interface to be studied.

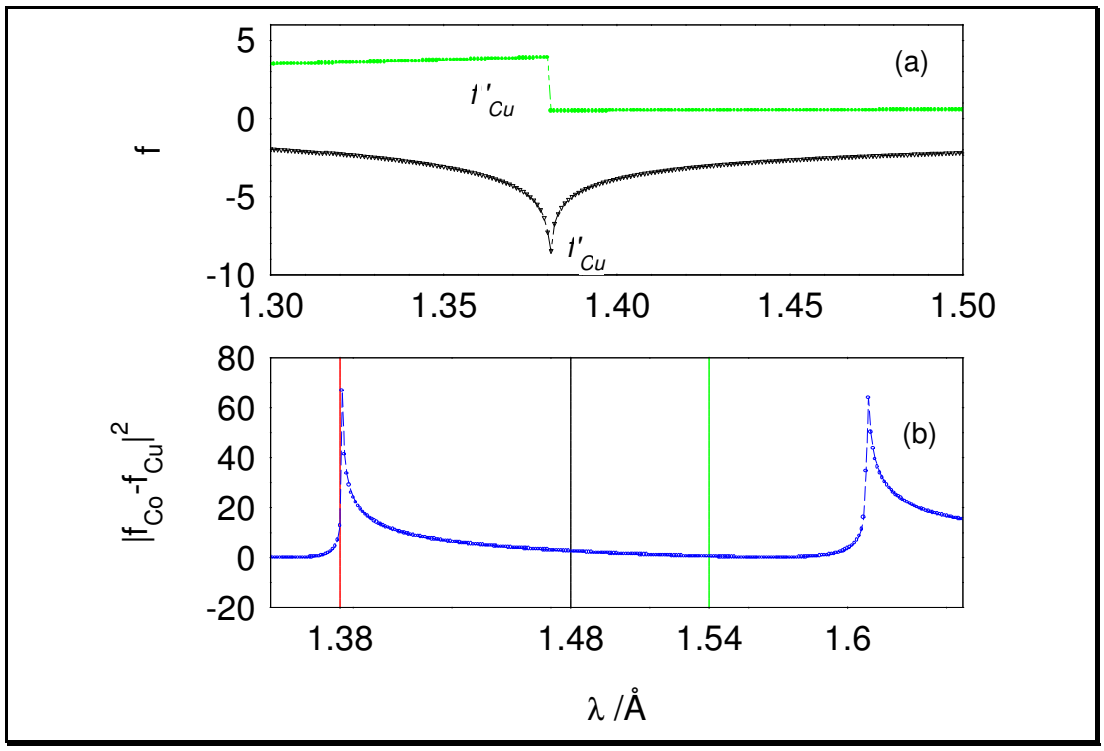

Figure 2.4: (a) shows the wavelength dependence of the anomalous dispersion correction factors for Cu at and well away from the absorption edge (produced using XASF program written by M. Wormington [23]). (b) illustrates the difference in scattering factors between Co and Cu at the wavelengths used in this study.

By tuning the wavelength to the Cu edge, enhancement in the scatter from the Co/Cu interfaces is seen. The critical angle and Kiessig fringes remain unchanged, but the scatter in the region of the Bragg peak is enhanced with the utilisation of the anomalous dispersion. This can be illustrated by comparing the specular scan at and away from the absorption edge, as seen in Figure 2.5.

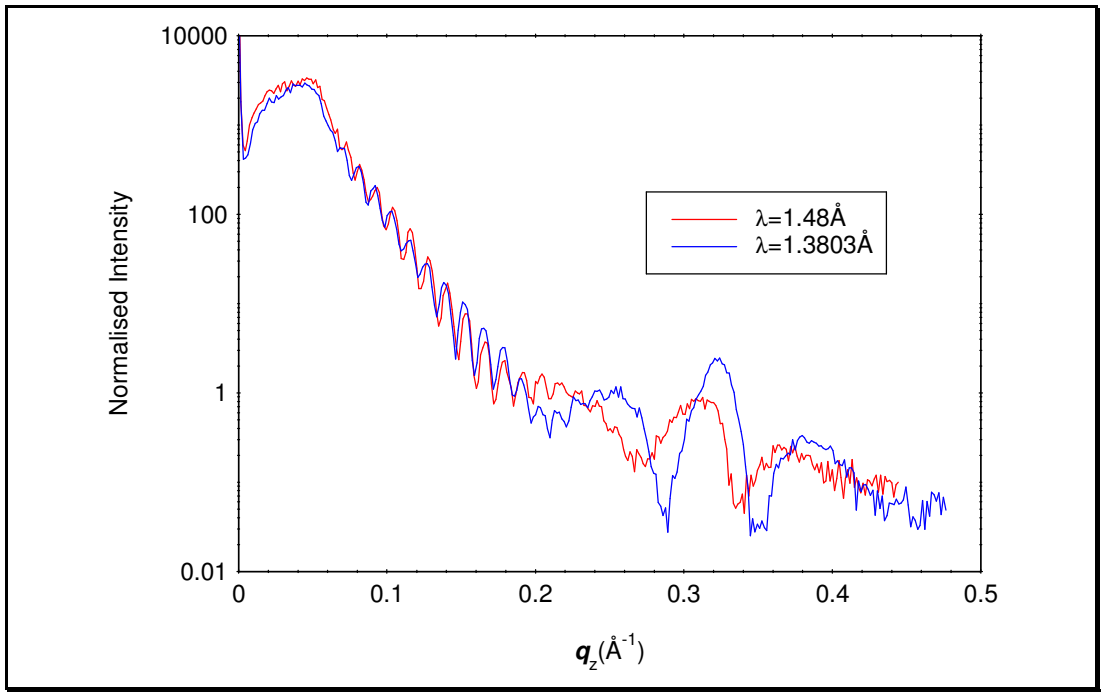

Figure 2.5: Specular scans on a Co/Cu multilayer, close to, and away from, the Cu absorption edge.

This enhancement in the scatter at the Bragg peak is also seen in the transverse diffuse scan, enabling more information about the morphology of the Co/Cu interfaces to be extracted.

2.3. Experimental.

The experimental work in this thesis has been carried out on a laboratory diffractometer at the University of Leeds, the SRS at Daresbury Laboratories and the ESRF in Grenoble. This section outlines the diffractometer in Leeds, and Station 2.3 at Daresbury.

2.3.1. Siemens Diffractometer.

The diffractometer in Leeds is a Siemens diffractometer, but with a recent upgrade of the machine. It utilises a Cu tube operated at 40kV and 30mA which produce x-rays of wavelengths λ=1.39Å and 1.54Å. The machine is used for both low and high angle studies. For the reflectivity, an incident slit with angular acceptance of 1/8° and a detector slit of 0.1mm are used, whereas for diffraction the incident and detector slits are 1/4° and 0.2mm respectively. These detector slits give an instrument resolution of 2' and 4' respectively. These are an order of magnitude lower than that of the incident beam, set by the incident slits, so serve to control the intensity of the beam. A single bounce Si monochromator can be used, with a Ni filter to reduce the K_β contribution to the beam. Soller slits are placed before the collimating slits to ensure all of the rays incident on the sample are parallel to the focussing plane. These Soller slits consist of parallel thin metal sheets and eliminate the rays inclined at some angle to the plane [24]. A schematic diagram of the diffractometer is given in Figure 2.6.

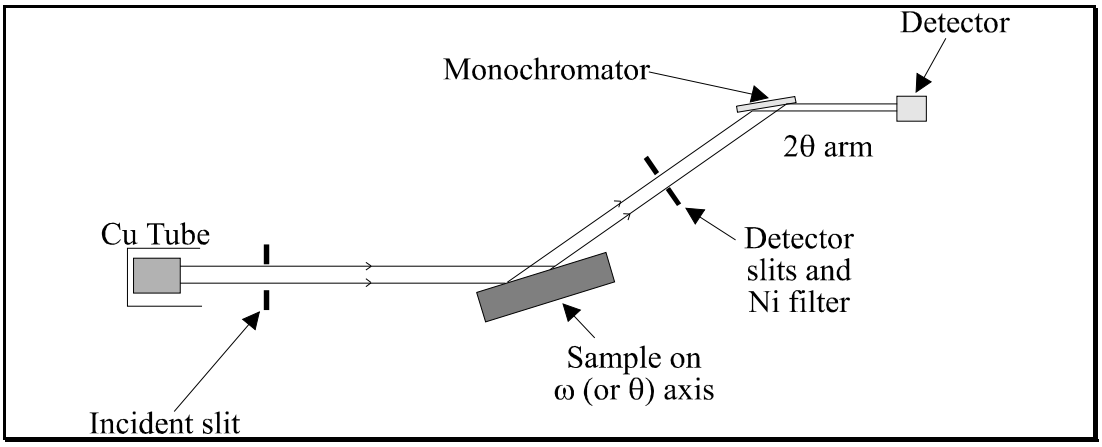

Figure 2.6: Schematic of the Siemens diffractometer.

The recent upgrade of the machine involved connecting the motors, which drive the θ and 2θ axes, to the serial port of the PC. The scintillation detector was connected to a digital counter, which can now be read using the same PC. This enables the PC to control all of the necessary functions to carry out scans automatically, which was not possible before the upgrade. A step size of 0.005° can be used, along with the possibility of choosing the count-time required at each point in the scan.

The full aligning procedure for the diffractometer was developed by M.J. Hall and is detailed in his PhD thesis [25]. It was found that this procedure was only necessary when the diffractometer appeared to be significantly out of alignment. By placing a fluorescent screen in the goniometer, if the beam could be seen on the screen, and the beam did not move across the screen as it was rotated, the diffractometer could be assumed to be close to alignment. Once this was established, the exact position of the beam through the diffractometer was found by scanning the detector through the beam (with a Cu block in front of the detector to protect it) and the offset from zero determined. This offset was subtracted from the 2θ value to give the true position of the detector with respect to the beam. If the offset was ±0.2°, the diffractometer was assumed to be aligned.

Once the diffractometer had been aligned, the sample was mounted on a glass slide and placed in the goniometer. The detector was set to a convenient angle for alignment, typically 1° for low angle scans and the substrate diffraction peak for high angle scans. The sample was aligned by rotating the goniometer until the counts were maximised. The sample was then in the specular condition and the required scans could be carried out automatically using the computer software.

2.3.2. Daresbury SRS.

There are several advantages in using synchrotron radiation: the high beam intensity, a well-collimated beam, and the tunable wavelength allowing anomalous dispersion techniques to be employed.

In the SRS x-rays are produced by the acceleration of a 2GeV electron beam in the storage ring [26]. The beam current is about 200mA at the beginning of the fill and it decays to about 100mA at the end of the fill. Station 2.3 is situated about 15 m tangentially from a pair of 1.2T dipole magnets where x-ray wavelengths of 0.5-3Å are available, with the peak flux being at approximately 1.3Å. The white beam from the synchrotron is intrinsically well-collimated (1 mrad vertical divergence) and then the

beam is filtered by the station silicon monochromator. The monochromatic x-ray is finally incident on to the diffraction instrument, as shown schematically in Figure 2.7.

The diffractometer is a two-circle machine with a sample ω (or θ) axis and a detector 2θ axis. The motorised circles and other motors are driven by electronic and computer-based controllers. The diffractometer was initially designed for high-resolution powder diffraction (HRPD) studies, but is now also used for x-ray reflectivity measurements.

The scattered rays are detected with a Bede Scientific EDRa scintillation detector [27], which uses NaI(Tl) as the scintillating material. The maximum count rate for non-dead time corrected data is 400,000cps, and the minimum count rate is 0.15cps. The experimental background was measured to be 1cps due to scatter within the hutch.

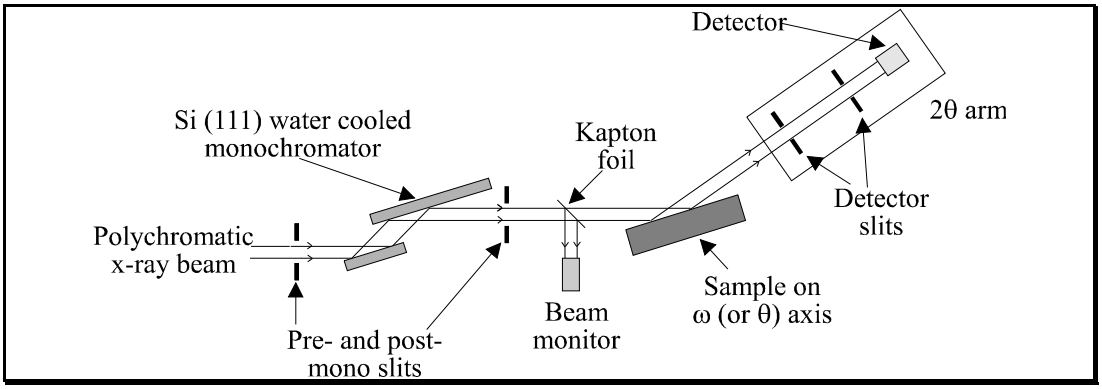

Figure 2.7: Schematic diagram of Station 2.3 at the SRS, Daresbury.

The post-monochromator slits defined the size of the beam, typically 100μm high and 4mm wide. The analyser slits immediately in front of the detector were set at the same height as the incident slits. An additional slit, closer to the sample on the detector arm, was set at 1mm high to reduce air scatter. The width of these slits was 10mm, resulting in very poor resolution in $\boldsymbol{q}_y$. A vacuum can fitted with Kapton® windows was placed between the detector slits to reduce air-scatter.

For diffraction studies at high angles, the heights of the incident and analyser slits were increased (to the same value) to increase the intensity. However, this led to a decrease in the resolution.

2.3.3. Alignment of Station 2.3.

The full procedure for aligning the diffractometer was followed at the start of each beam-time allocation. Since a full description is given elsewhere [28], the procedure is only outlined here.

The main rotation and translation motors are shown in Figure 2.8. These were used in the alignment procedure of the diffractometer, and in the sample alignment. The θ and 2θ axes are encoded to a resolution of 0.72" and 0.36" respectively [26]. The other motors are not encoded so suffer from backlash. However, these motors are only used for the initial alignment, so the backlash is not important.

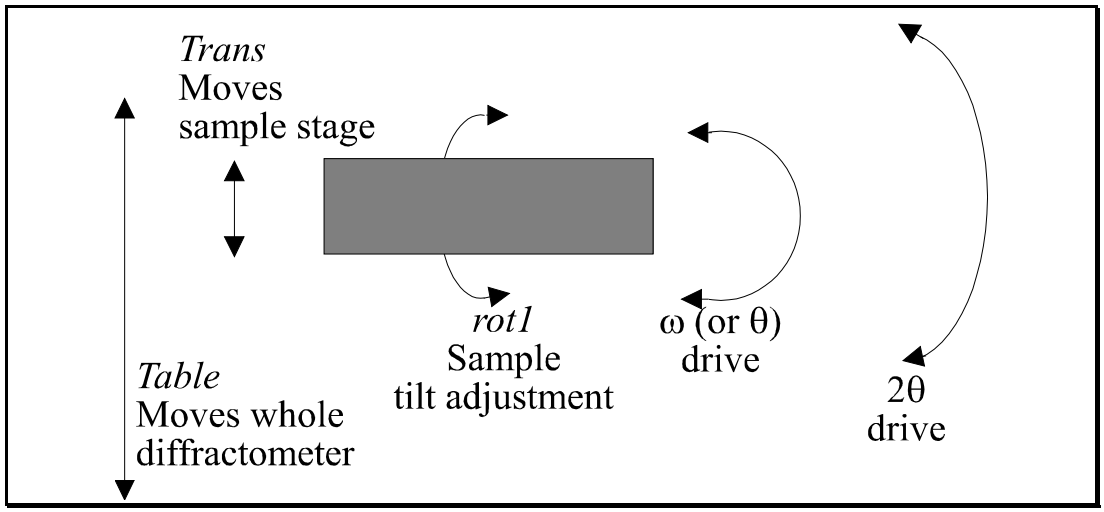

Figure 2.8: Main rotation and translation axes for the diffractomter on Station 2.3, Daresbury.

To ensure the sample stage was on the centre of rotation of the diffractometer, a telescope was focussed onto the surface of the sample stage, and the ω-motor driven so that the stage moved through 180°. The cross-hairs remained in the same position on the sample stage if the stage was in the centre of rotation. If the position varied, the height of the goniometer was adjusted by half the displacement and the procedure repeated until the centre of rotation was attained. Once this was established, the beam size was defined by the post-monochromator slits and the table half-cut so that half of the beam was passing over the surface of the sample stage. The centre of the stage was now on the centre of rotation of the diffractometer.

The next stage was to ensure the centre of rotation of the table is in the middle of the x-ray beam. The sample stage was moved out of the way using the *trans* motor, and the direction of the beam defined by scanning the detector through the main beam. The centre of the beam was defined as $2\theta=0°$. The sample stage was moved back to the original position, and the position of the beam passing over the stage determined using photographic paper. The height of the whole table was adjusted to put the centre of rotation of the diffractometer in the x-ray beam.

Once the position of the beam had been defined, the detector slits could be set. The front slit was set at 100μm high and the width ±0.5mm either side of the centre of the beam. With the height of the back slit set at the same100μm, the calculated acceptance angle of the detector was 613".

Once the diffractometer had been aligned, the sample was placed on the sample holder and the detector positioned at $2\theta = 0°$. With aluminium attenuation placed in the beam to protect the detector, the sample was half-cut using the *trans* motor to obtain half of the beam running over the surface. The ω motor was rocked, to ensure the sample was flat and the half-cut procedure carried out again. The detector was moved to a small angle, typically $2\theta=2°$, and the sample rocked around $\omega=1°$ until the maximum counts were obtained. This position was set to $2\theta/2$. The alignment was checked at a higher value of 2θ to confirm the alignment so that the condition $\omega = 2\theta/2$ was fulfilled.

2.4. Types of X-Ray Scan.

There are three types of x-ray scan utilised in this thesis, specular, off-specular and transverse diffuse scans (often called rocking curves). Each scan probes different regions of reciprocal space, so a detailed map of the structure can be constructed. The areas of reciprocal space probed by the different scans are shown in Figure 2.9.

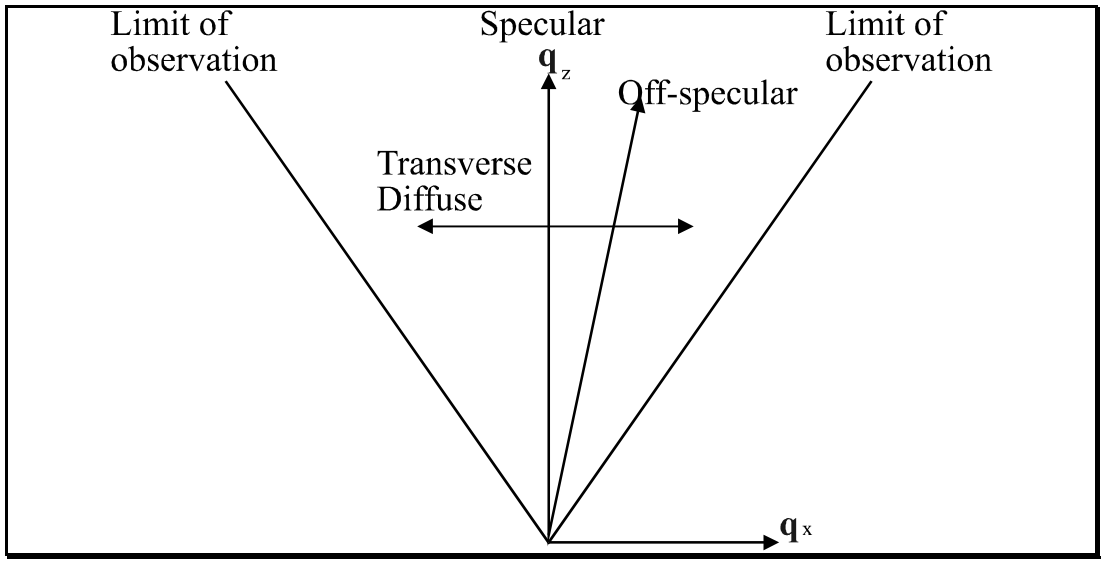

Figure 2.9: Movement scans in reciprocal space.

The z direction is normal to the sample, and the limit of observation is set by the critical angle of the sample. The experimental methods to realise the scans utilised in this thesis are outlined below, along with the information each scan can provide.

2.4.1. θ/2θ Scan

In this scan the sample and detector arm are coupled and rotate together, with the detector rotating at twice the sample rotation rate. As the incident and exit angles of the x-ray beam are equal, the direction of the scattering vector is always normal to the surface of the sample. Therefore, it is only possible to obtain information about vertical periodicity within the structure, without gaining any insight into any lateral variations. This lack of lateral information means only the total interface width can be calculated, and not the components of the roughness which go to make up the interface.

Due to the high intensity of the synchrotron, the specular scan must be split into two parts. The majority of the scan (from 1.5° onwards) is taken normally. However, below 1.5°, the intensity of the scattered beam is too intense for the detector, as total external reflection occurs. To prevent damage to the detector, attenuation is placed in the beam, and a scan from 0-2° is undertaken. This scan can be scaled to the other specular scan to take account of the attenuation.

2.4.2. Off-specular $\theta/2\theta$ Scan.

This is similar to the $\theta/2\theta$ Scan, with the sample offset from the specular condition by a known angle, δ. The scattering vector has a small component in the plane of the sample, dependent on the angle of offset. The relative scattering vectors are

$$q_z = \frac{2}{\lambda}\sin\left(\frac{\phi}{2}\right)\cos(\delta) \quad \text{..... (2.1)}$$

and

$$q_x = \frac{2}{\lambda}\sin\left(\frac{\phi}{2}\right)\sin(\delta) \quad \text{..... (2.2)}$$

where ϕ is the scattering angle.

If there is correlated roughness present, the Bragg peaks are not points in reciprocal space, but extend into q_x. This leads to a Bragg peak in the off-specular scatter [29], but of a lower intensity and a broader width than of that seen in the specular scan. By comparing the height of this Bragg peak with the peak in the specular scatter, a qualitative idea of the degree of correlation can be determined. If the roughness is correlated from the substrate, this argument can be extended to the Kiessig fringes leading to Kiessig fringes in the off-specular scatter [30].

The off-specular scan is important for another reason. When the specular scan is carried out, there is still a component of the diffuse scatter within the specular condition but the off-specular scan provides this diffuse component. By subtracting this scatter from the specular scan, the true specular scatter can be obtained.

2.4.3. Transverse Diffuse Scan.

The transverse diffuse scan, often called a rocking curve, is a method of obtaining the scattering vector in the plane of the sample. With the scattering vector in the plane, information can be gained about the lateral variations within the sample, such as the correlation length and the separation out of the different components of the roughness. An example of such a scan is shown in Figure 2.10.

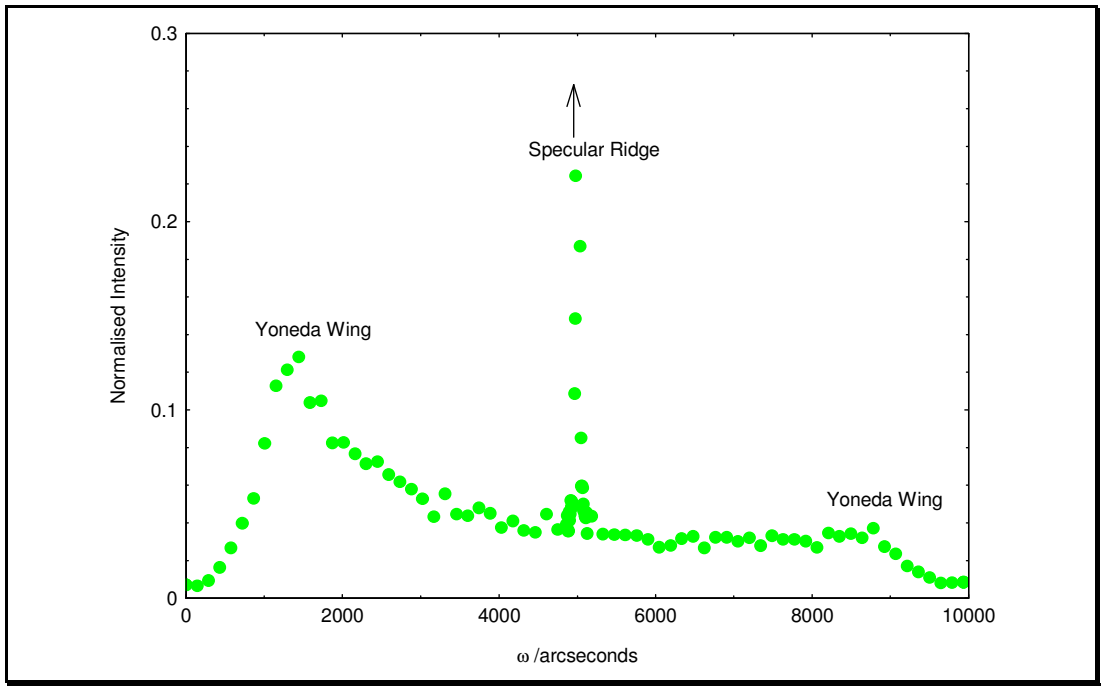

Figure 2.10: Typical transverse diffuse scan, illustrating the Yoneda wings and the specular ridge.

The detector is held fixed at a certain angle, often a Kiessig maximum or a Bragg peak, and the sample is rotated. This can give information about the type of roughness at interfaces. The diffuse scans are the sum of a sharp term, which is a cross-section of the specular ridge, and a diffuse term from scattering off the disorder at interfaces. The width of the specular ridge is defined by the instrumental parameters. In a synchrotron it

is sharp, with a FWHM of 16". If the sample is figured, this will cause the width of the specular ridge to be increased. The diffuse scatter is nothing more than an interference function of scattered waves from roughness at the interfaces. From the reciprocal nature of x-ray scattering, longer periods of roughness on the surface give rise to scatter closer to the centre of the scan. This is because reciprocal space and diffuse scans are Fourier transforms of the spatial frequencies, so the shape of the transverse diffuse scan gives information about the lateral correlation length within the sample.

At the edges of the transverse diffuse scans, there is a rise in intensity, known as the Yoneda wings [31]. These wings occur when the incident beam angle or the scattered beam angle is equal to the critical angle of the sample. At the critical angle, the transmitted beam lies along the surface of the sample. The scattering within the sample is in phase with the beam along the surface, so the magnitude of the electric field of the scattered wave is doubled at the surface. Hence there is an increase in the intensity of the diffuse scatter.

Once the experimental data has been collected, analysis must be carried out to obtain information about the structure of the sample. The main form of analysis in this thesis was in the form of simulating the experimental data to extract the important parameters. An outline of the theory behind the simulation package used is given in the next section, with an overview of the effect of changing parameters within the simulation program.

2.5. X-Ray Reflectivity.

For many years, x-ray reflectivity has been used to study the thickness and roughness properties of thin films. However, until recently only the specular scatter from multilayers had been considered. Consequently, an in-depth analysis of the type of roughness had not been possible. As the nature of the roughness at the interface controls the shape of the diffuse scatter, a mathematical model of the surface must be developed in order to probe the nature of the surface using simulations of the diffuse scatter. The following sections outline the development of the theory behind the simulation programs. The detailed theory is beyond the scope of this experimental thesis, and the references given provide more detail in the development of the theory.

2.5.1. X-Ray Reflectivity - Parratt Recursive Formula.

The early work which utilised x-ray reflectivity was carried out by Parratt [32] using the optical Fresnel transmission and reflection coefficients. He considered the interaction of the electromagnetic wave with the electronic distribution of the medium. By considering the boundary conditions at the interfaces, Maxwell's equations lead to an expression for the Fresnel coefficient for the reflection intensity from the sample. These boundary conditions are that the tangential components and their derivatives of the electric field are equal on each side of the interface. If the ratio of reflected and incident electric vectors at the top of layer *n* is

$$R_n = \frac{a_n^2 E_n^R}{E_n} \quad \text{..... (2.9)}$$

its value at the top of layer *n-1* is calculated by

$$R_{n-1} = \frac{a_{n-1}^4 \left(R_n + F_{n-1}\right)}{R_n F_{n-1} + 1} \quad \text{..... (2.10)}$$

where

$$a_n = \exp\left(-\frac{i\pi f_n d_n}{\lambda}\right) \;;\; a_1 = 1$$

$$F_{n-1} = \frac{(f_{n-1} - f_n)}{(f_{n-1} + f_n)}$$

$$f_n = \left(\phi^2 - 2\delta_n - 2i\beta_n\right)^{1/2} \;;\; f_1 = \phi$$

and d_n is the thickness, $1-\delta_n - i\beta_n$ the refractive index of layer n, and ϕ is the incident angle of the x-rays at the top surface. These functions are defined for the middle of the layer. The calculation is started from the bottom layer, an infinitely thick substrate with $R_N = 0$, and finishes at the top with medium 1 (air). The ratio of intensities is given by

$$\frac{I}{I_o} = \left|\frac{E_1^R}{E_1}\right|^2 \quad \text{..... (2.11)}$$

This method has been used successfully for many years to obtain thickness information and the dispersion of thin films. However, it only considers the Fresnel optical transmission and reflection coefficients and does not consider scattering at interfaces caused by roughness. To gain information about the roughness and quality of interfaces, the scattering of x-rays within the sample must be considered.

To model a rough surface, the reflection coefficient must be modified by a factor which scales with the interface roughness σ. Two forms of this factor are in common use. The first form is the so-called static Debye-Waller factor [33], $\exp\left(-\boldsymbol{q}_z^2\sigma^2\right)$, where $\boldsymbol{q}_z$ is the scattering vector. The second form, due to Névot and Croce [34], is $\exp\left(-\boldsymbol{q}_z\boldsymbol{q}_z^t\sigma^2\right)$, where $\boldsymbol{q}_z^t$ is the scattering vector inside the material after refraction.

2.5.2. Born Approximation.

In their paper in 1988 [35], Sinha *et al* discussed the specular and diffuse scattering from rough surfaces, and the main points raised in this paper are given here. The nature of the surface roughness dictates the shape of the diffuse scatter. A mathematical model of the surface must be assumed to gain information about the surface from the diffuse scatter.

The height, *z(x,y)*, above a surface S_o in the *(x,y)* plane is assumed to be single-valued. The distribution of heights above this surface $\left[z(x',y') - z(x,y)\right]$ is assumed to be a Gaussian random variable whose distribution depends on the relative co-ordinates $(X,Y) = (x'-x, y'-y)$. The distribution of heights, associated with the self-affine surface defined by Mandelbrot [36], is given by $g(X,Y) = AR^{2h}$, where $R = \sqrt{X^2 + Y^2}$, h is the roughness exponent of the interface, sometimes called the Hurst parameter. This is restricted to $0 \le h \le 1$ and gives an indication of the "jaggedness" of the interface, from *h=0* corresponding to a jagged surface, to a smoothly undulating surface for *h* approaching 1. However, this distribution diverges at infinity, so an effective cut-off length ξ for the roughness is introduced. The distribution of heights is now given by

$$g(R) = 2\sigma^2\left[1 - \exp\left(\frac{-R}{\xi}\right)^{2h}\right] \quad \text{..... (2.12)}$$

ξ is known as the correlation length and σ is the total rms roughness at the interface. The proposed height-height correlation function, which relates the height information between two points, separated by *R*, is given by [35]

$$C(R) = \sigma^2 \exp\left[-\left(\frac{R}{\xi}\right)^{2h}\right] \quad \text{..... (2.13)}$$

This correlation function is widely used in simulations using the Born Approximation (BA) and the distorted wave Born Approximation (DWBA) [30,37].

Where the reflectivity is weak, the Born Approximation is used. This is a kinematical description of x-ray scattering, so assumes that there is no multiple scattering. The differential cross-section for scattering at a single interface between two media can be derived from the Born Approximation. This scattering equation can then be split into two distinct parts, corresponding to the specular and diffuse scatter, with the scattering equations

$$S_{spec}(\boldsymbol{q}) = \frac{4\pi^2}{\boldsymbol{q}_z^2}\exp\left[-\boldsymbol{q}_z^2\sigma^2\right]\delta(\boldsymbol{q}_x)\delta(\boldsymbol{q}_y) \quad \text{..... (2.14)}$$

and

$$S_{diff}(\boldsymbol{q}) = \frac{2\pi}{q_z^2}\exp\left(-\boldsymbol{q}_z^2\sigma^2\right)\int_0^\infty R\left[\exp\left(\boldsymbol{q}_z^2\sigma^2 e^{-(R/\xi)^{2h}}\right)-1\right]J_o\left(\boldsymbol{q}_{x,y}R\right)dR \quad \text{..... (2.15)}$$

where $J_0(\boldsymbol{q}_{x,y}R)$ is a Bessel function of the first kind. $S(\boldsymbol{q})$ is defined as the (cross section per unit area surface)/(N^2b^2), where *b* is the Thomson scattering length of the electrons and *N* is the number density of electrons.

The specular part of the scatttering equation can be converted to the reflectivity to yield the normal Perod's law. This is equivalent to Fresnel theory at large angles, modified by an exponential Debye-Waller-like factor due to the total roughness smearing the average surface. The diffuse scatter can be evaluated numerically using the height-height correlation assumed for the system and the scattering equation. However, the specular reflectivity diverges for small $\boldsymbol{q}_z$, so a better model close to the critical angle is required.

2.5.3. Distorted Wave Born Approximation.

The Born Approximation is only valid for weak reflectivity, and no account for total external reflection at the surface is made. For x-ray scattering at grazing incidence, dynamical theory is used to overcome the limitations of the Born Approximation. There are several excellent reviews on this subject (for example, see [30]) and the reader is referred to these for a more detailed explanation of the theory. The distorted wave Born Approximation (DWBA) was developed to incorporate the dynamical approach to allow for multiple scattering within the sample.

The wave is incident on the sample, and scattered by a potential due to the ideal surface. The transmitted and reflected components are calculated from Fresnel theory, and exact solutions are found. These plane waves are then perturbed by a second potential, due to the roughness. At this stage, the waves originating from within the sample, sometimes referred to as the time-reversed states, are considered. These time-reversed states are considered to ensure a unique solution.

The full differential cross-section for this process is given by Sinha *et al* [35]. By expanding the roughness in terms of Gaussian statistics they showed the reflectivity is given by

$$\left|R(k)\right|^2 = F_l^{\,R} \exp(-\boldsymbol{q}_z \boldsymbol{q}_z^t \sigma^2) \quad \text{..... (2.16)}$$

where $F_l^{\,R}$ are the Fresnel reflection coefficients and $\boldsymbol{q}_z^t$ is the wave-vector of the wave transmitted into the medium at the interface. For small values of $\boldsymbol{q}_z^t$ and $\boldsymbol{q}_z$, assuming $\boldsymbol{q}_c\sigma$ is not too large and $\boldsymbol{q}_z \geq \boldsymbol{q}_c$, equation 2.16 is the same as the expression derived by Névot and Croce by a different method [34]. For very large values of $\boldsymbol{q}_z$, when $\boldsymbol{q}_z\sigma >> 1$, the BA and equation 2.16 agree very well, whereas the true DWBA over-estimates the specular reflectivity. To summarise, equation 2.16 seems a good interpolation of the BA and DWBA and a good approximation to the specular scatter.

For the diffuse scatter, it has been shown that the differential scattering cross-section is given by [35]

$$\left[\frac{d\sigma}{d\Omega}\right]_{Diff} = L_x L_y \frac{\left|k_0^2(1-n^2)\right|^2}{16\pi^2}\left|T(k_1)\right|^2\left|T(k_2)\right|^2 S(\boldsymbol{q}_t) \quad \text{..... (2.17)}$$

$\left|T(k_i)\right|$ are the Fresnel transmission coefficients for the incident *(i=1)* and scattered *(i=2)* waves. L_xL_y is the illuminated area on the sample, k_o is the wave-vector of the incident radiation, n is the refractive index and $S(\boldsymbol{q}_t)$ is defined

$$S(\boldsymbol{q}_t) = \frac{1}{\left|\boldsymbol{q}_z^t\right|^2}\exp\left(\frac{-\left[\left(\boldsymbol{q}_z^t\right)^2 + \left(\boldsymbol{q}_z^{t*}\right)^2\right]\sigma^2}{2}\right) \times \iint_{S_o}\left[\exp\left(\left|\boldsymbol{q}_z^t\right|^2 C(X,Y)\right) - 1\right]\left[\exp \mathrm{i}\left(\boldsymbol{q}_x X + \boldsymbol{q}_y Y\right)\right]\mathrm{dX}\mathrm{dY} \quad \text{..... (2.18)}$$

The Fourier transform in equation 2.18 does not, in general, have an analytical solution and it must be calculated numerically. This can be very time consuming and is thus the rate determining step in computations. In order to increase the speed of computation, M. Wormington [38] has developed a method based on look up tables which enable the computer simulations to be carried out on standard PC's.

To calculate the diffuse scatter for a sample containing more than one interface, information about how the morphology at each interface replicates between layers is necessary, so another correlation function is necessary. This is given by [35]

$$C_{l,l'}(R) = \left(\sigma_{u,l}\sigma_{u,l'}\delta_{l,l'} + \sigma_{c,l}\sigma_{c,l'}\right)\exp\left[-\left(\frac{R}{\xi}\right)^{2h}\right] \quad \text{..... (2.19)}$$

where $\delta_{l,l'}$ is the Kronecker delta operator, and the rms roughness of the *lth* interface can be defined in terms of two components, the uncorrelated roughness, σ_u, which does not replicate from layer to layer and the correlated roughness, σ_c, which replicates the interface morphology perfectly. The roughnesses are related by

$$\sigma_{rms} = \left(\sigma_u^2 + \sigma_c^2\right)^{1/2} \quad \text{..... (2.20)}$$

The correlation length and roughness exponent are assumed to be the same for all interfaces. This is then inserted into the scattering equation determined by the DWBA (equation 2.17) and solved analytically to calculate the diffuse scatter. However this

analytical solution can be computationally very demanding as it may involve a large number of terms.

The DWBA is used in the simulation software to model the diffuse scatter. For the specular scatter however, the DWBA is used to simulate the scatter very close to the critical angle, and equation 2.16 used for higher incident angles where the DWBA yields too large a value for the reflectivity. De Boer [39] has recently extended the DWBA to second order to obtain an expression for the reflectivity valid at all angles.

There is no fixed method for fitting the simulations to the experimental data, and much care is needed when carrying out this procedure. In the specular scan there are several features which are influenced by more than one parameter within the simulation. For this reason two simulations are carried out, at different incident energies, for each sample.

The following sections illustrate the effect of systematically changing the main parameters within the simulations to give an idea of the type and magnitude of changes in the resultant curve. From these curves, an idea of a fitting strategy can be extracted.

2.5.4. Simulating the Specular Reflectivity.

For scattering in the specular condition, there is a component of the diffuse scatter present. To convert the data into a form that can be simulated, this diffuse scatter must be accounted for by subtracting the off-specular (or longitudinal) diffuse scatter. Once normalised to the beam, the experimental data is now ready to be simulated. The simulations are carried out using the GIXA programs from Bede Scientific [1].

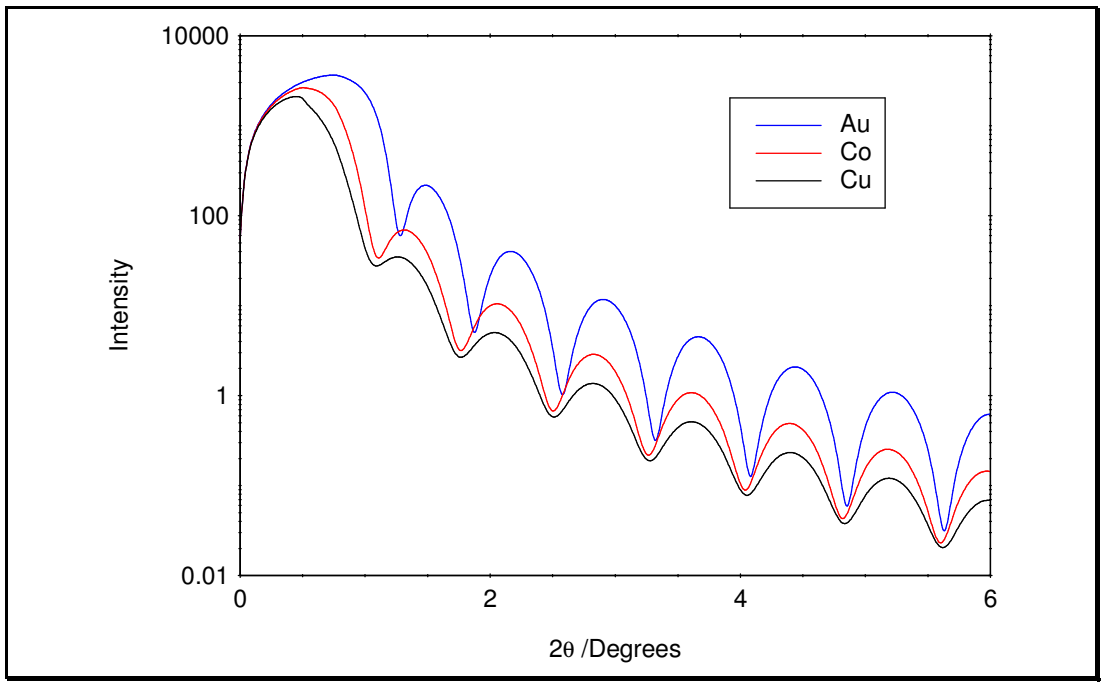

Figure 2.11: Effects of changing the element of a single layer of thickness 100Å.

At very low incident angles the x-rays are externally reflected, as the refractive index for x-rays in a metal is less than that for air. At some angle θ_c, known as the critical angle, the x-rays will start to penetrate the metal. This angle is dependent on the electron density at the surface of the metal and can be varied by changing the top

surface material. Figure 2.11. are the specular simulations of different elements (Au, Cu and Co), of thickness 100Å. The angle at which the intensity drops abruptly is the critical angle, and can be see to vary from element to element. Close to the critical angle, the period of the Kiessig fringes is affected by differences in the disperion between materials, as predicted in equation 2.7. For $\theta >> \theta_c$, the period of the fringes remains constant for all of the elements, as the same thickness is simulated in each case.

In this thesis, the samples under consideration are multilayers. As already shown, the periodicity from the multilayer appears as a diffraction peak, and the position of this peak is dependent on the thickness of the bilayer in the multilayer. Figure 2.12 shows the effect of varying the bilayer thickness on the position of the multilayer Bragg peak. The sample simulated is a Co/Cu multilayer, with the bilayer repeat varying from 15-30Å.

Although the thickness of the bilayer can be determined accurately from the position of the Bragg peak, the relative thicknesses of the two materials can prove more difficult. Figure 2.13 shows the simulations of three Co/Cu multilayers, with a 20Å bilayer, but the relative thicknesses of the Co and Cu varied between simulations.

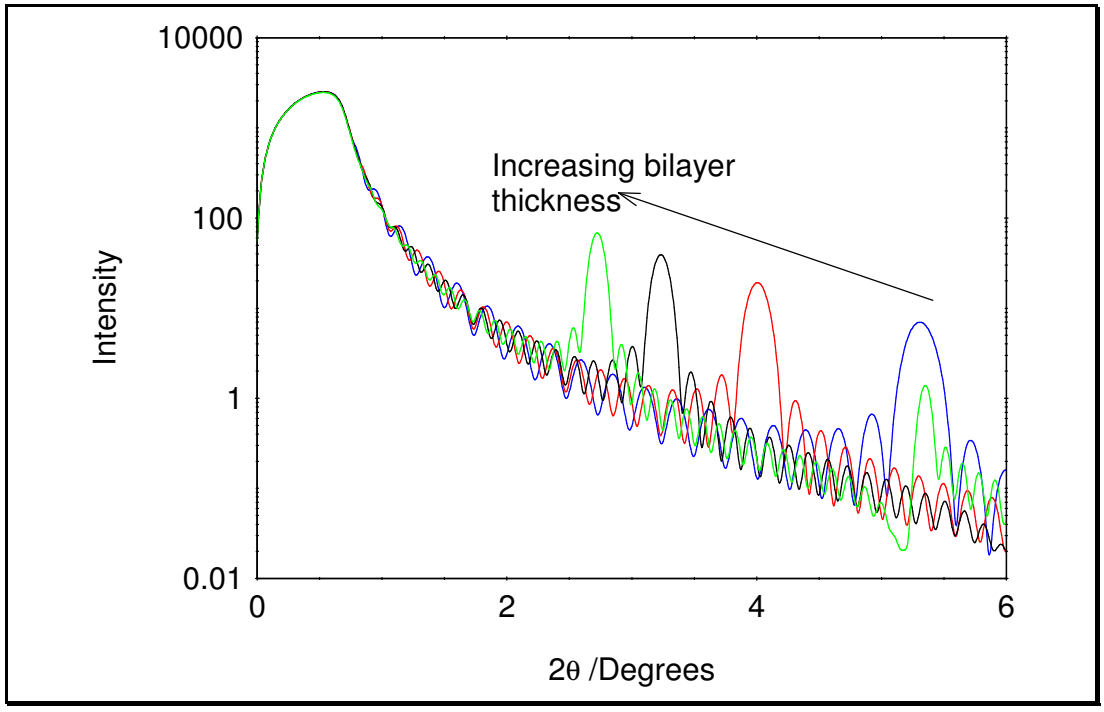

Figure 2.12: Variations of the Co/Cu thickness on the Bragg peak position.

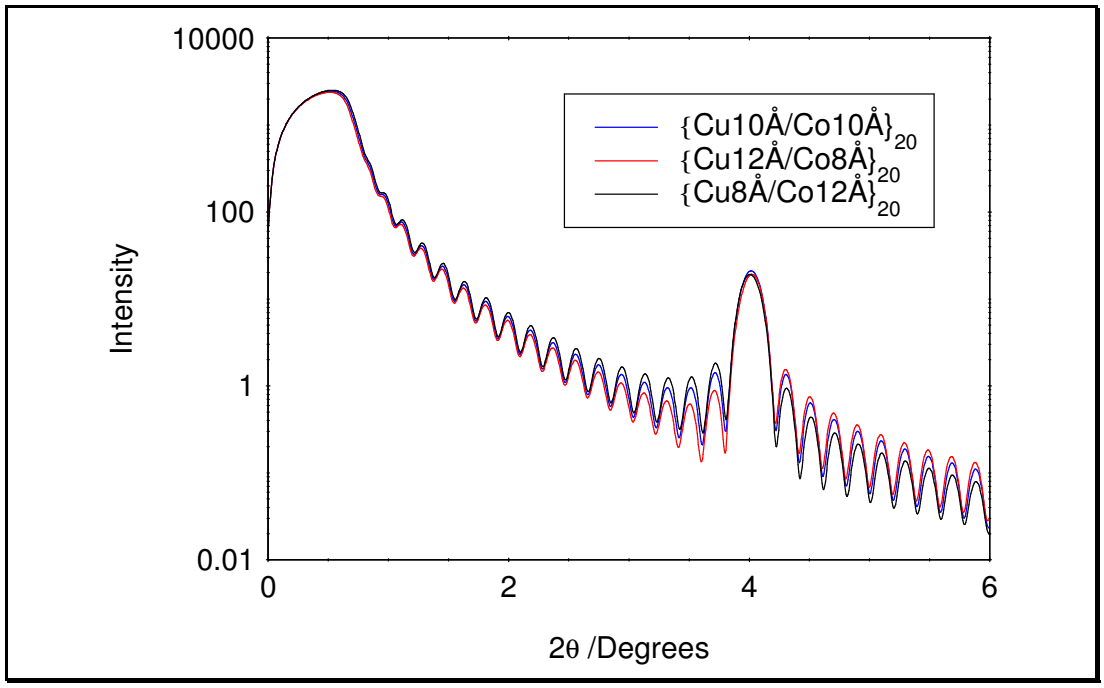

Figure2.13: Effect of varying the ratio of Co and Cu in a multilayer.

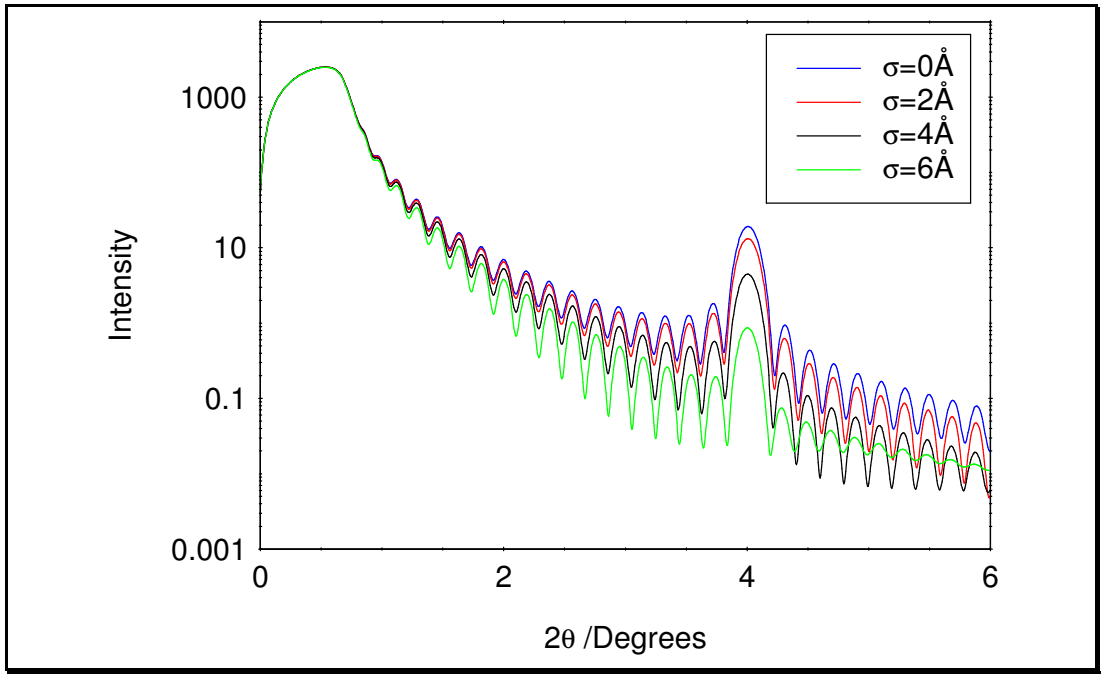

Figure 2.14: Interface roughness causing a reduction in the Bragg peak intensity.

In a real system, there is roughness present at the interface of the Co/Cu, and this roughness affects the height of the Bragg peak [29]. Figure 2.14 compares a $\{Co8Å/Cu12Å\}_{20}$ multilayer with interface roughnesses of 0,2,4 and 6Å. The height of the Bragg peak is reduced with increasing roughness, and the Kiessig fringes close to the Bragg peak are affected.

The multilayers are normally capped using a thin layer of Au, to prevent oxidation whilst ex-situ characterisation is carried out. This cap produces a single layer modulation on the experimental data. A comparison of an uncapped $\{Co8Å/Cu12Å\}_{20}$ multilayer with multilayers capped with different thicknesses of Au is shown in Figure

2.15. By matching the period of this single layer modulation, the thickness of the cap can be determined to within 1Å. The thickness of the capping layer can also have an effect on the height of the Bragg peak [11], and this needs to be kept in mind whilst simulating data.

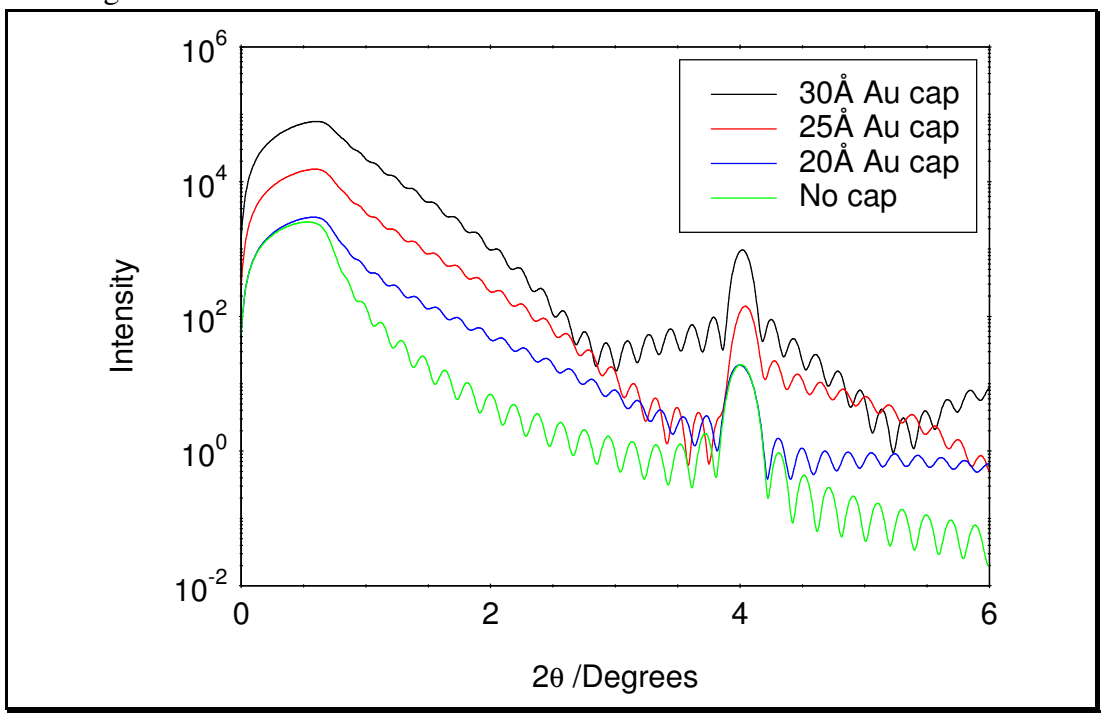

Figure 2.15: Variation of the modulation due to the different cap thicknesses (curves displaced for clarity).

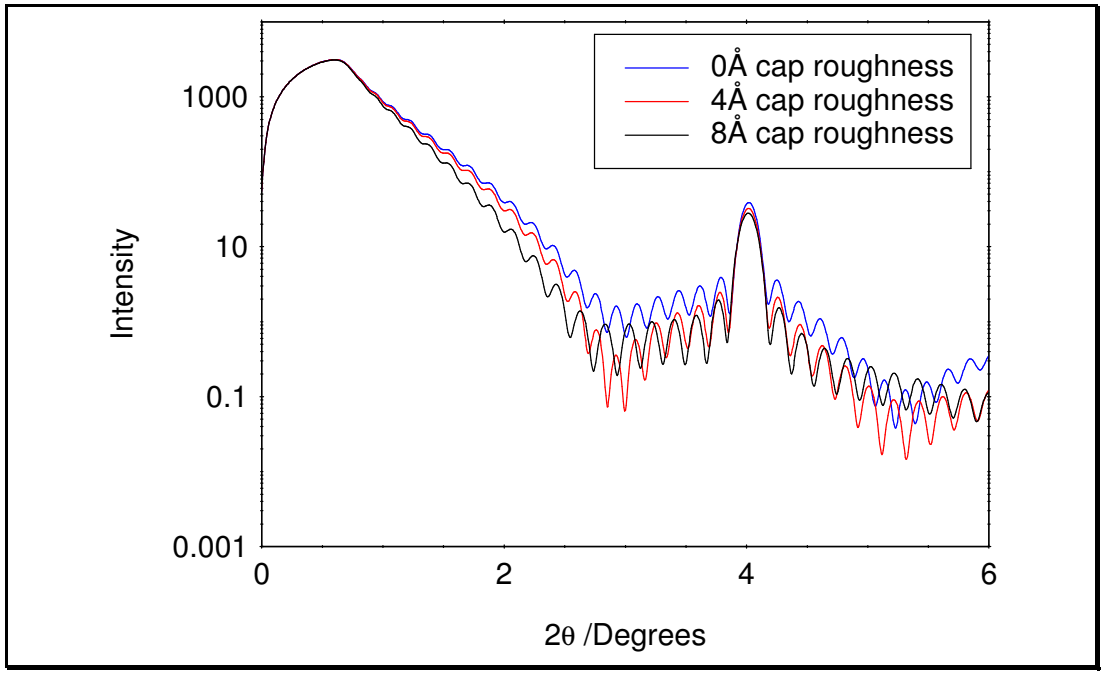

Figure 2.16: Change in the modulation due to capping layer roughness.

Roughness on the cap surface also has an effect. The position of the modulation remains unaffected, but the shape is changed, as shown in Figure 2.16. The fall-off of the curve is increased after the critical angle as the roughness increases, and the depth of the dip in the modulation is also affected.

To ensure epitaxial growth of the multilayer samples, Kwo *et al* [40] first introduced a method utilising a 50Å Nb seed layer to promote good quality growth of rare-earth metals on sapphire substrates. Schreyer *et al* [41] adpated this method by depositing a Cu buffer layer on this seed layer for Co/Cu multilayers, and these Nb seed and Cu buffer layers are now widely used for Co/Cu multilayers. A Cu buffer layer was utilised because of the absence of Cu-Nb alloys reducing problems associated with interdiffusion at this interface. The multilayer is then deposited onto this buffer layer. To show the effect of these extra layers on the reflectivity, a seed and buffer layer was added to the multilayer capped with 30Å Au, and the resulting structure simulated. The comparison of the reflectivity curves is given in Figure 2.17. The similarity of these curves illustrates the difficulty in obtaining information about these layers from the reflectivity. The only visible change is to the period of the Kiessig fringes, and this change in period gives the thickness of these layers.

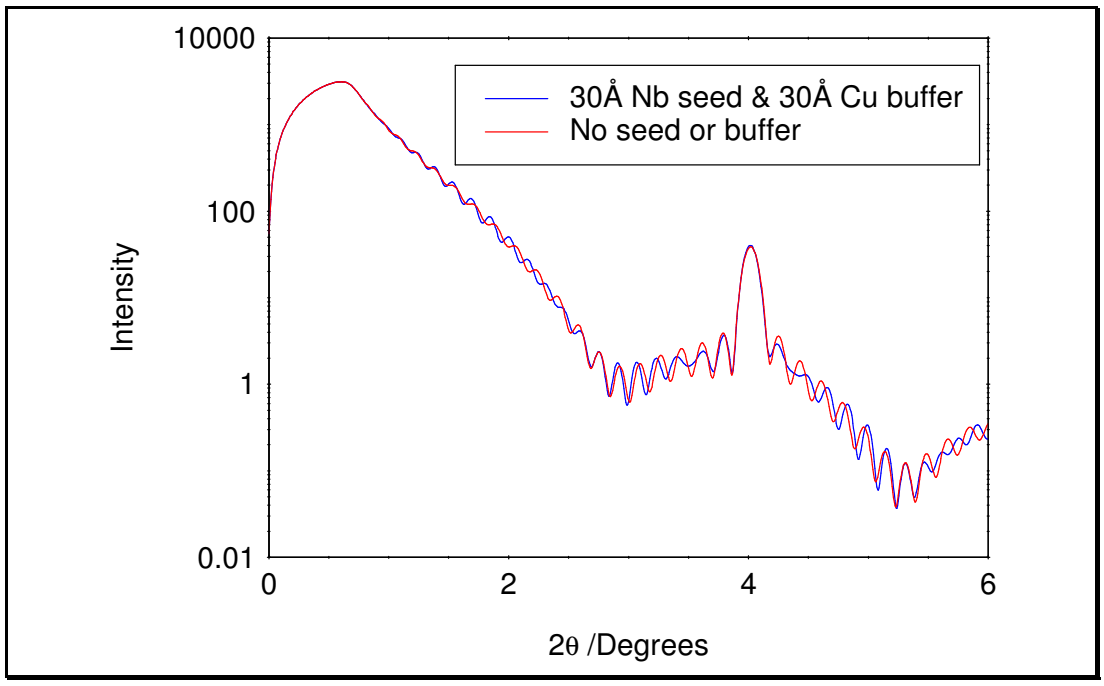

Figure 2.17: Effect of seed and buffer layers on the reflectivity of a multilayer.

Using these trends it is possible to simulate the specular scatter to extract information about the layer thickness and interface roughness. Information concerning the bilayer repeat and capping layers are more readily obtained. The seed and buffer layers have only a small effect on the specular reflectivity, and the thickness of these layers must be deduced from the period of the Kiessig fringes.

2.5.5. Diffuse Scatter from a Single Layer.

To illustrate the effect of the correlation length and roughness exponent on the diffuse scatter, simulations have been carried out on a 100Å layer of Cu on sapphire, with a substrate roughness of 2Å and a Cu roughness of 4Å. The effects of correlated and uncorrelated roughness on the diffuse scatter are demonstrated with the use of full reciprocal space maps.

Varying the correlation length enhances scattering close to the specular ridge, as shown in Figure 2.18. This is caused by the reciprocal nature of reciprocal space. As the length-scale is increased, this leads to scatter at low q_z, close to the specular condition.

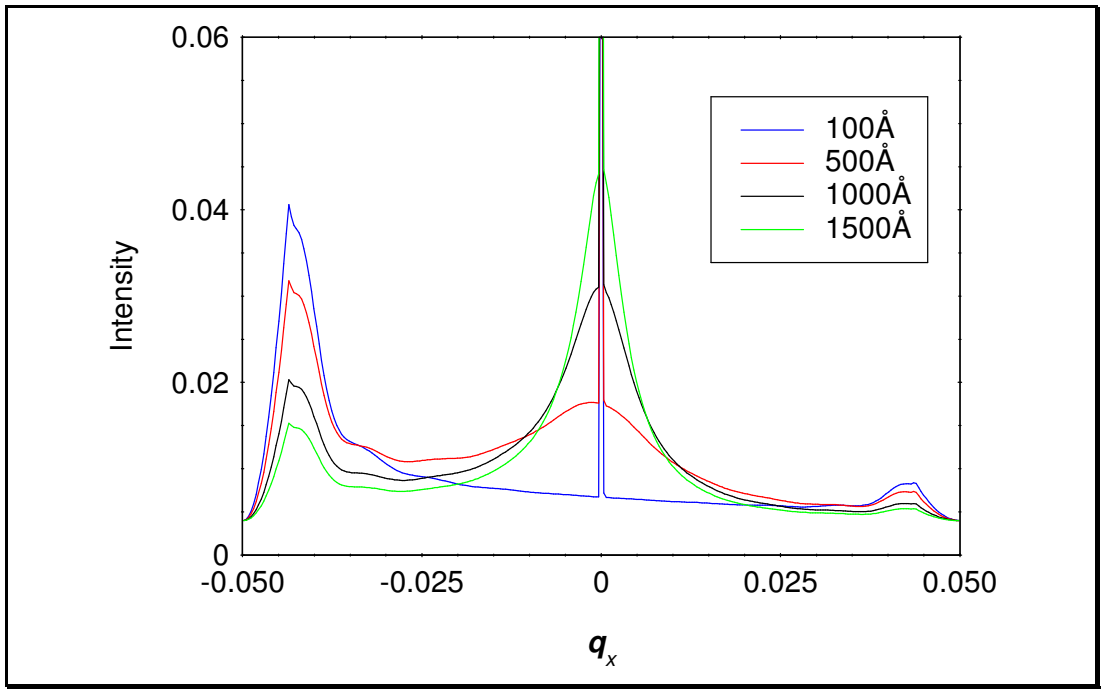

Figure 2.18: The effect of varying of the correlation length on a single layer of Cu (σ=4Å, h=0.3).

In a transverse diffuse scan, the roughness exponent, *h*, alters the size of the Yoneda wings and the general shape of the scatter, as illsutrated in Figure 2.19. Typical values of *h* are 0.2-0.3 for MBE-grown samples, and 0.6-1.0 for sputtered samples.

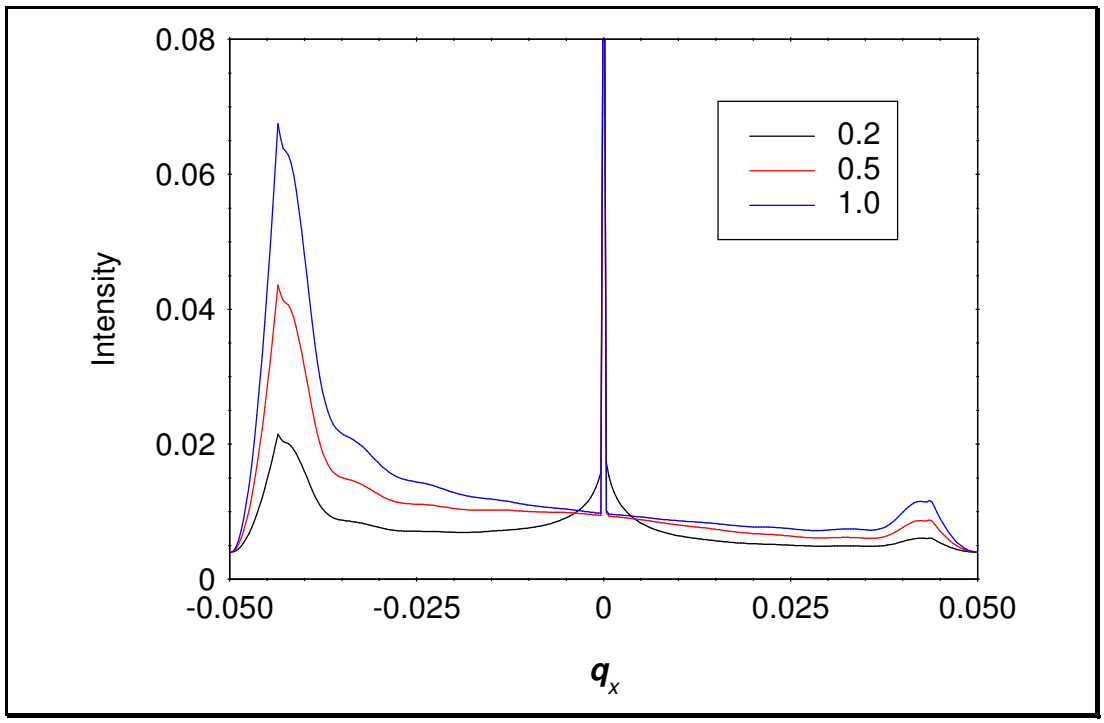

Figure 2.19: The effect of varying the roughness exponent on a single Cu layer (ξ=200, σ=4Å).

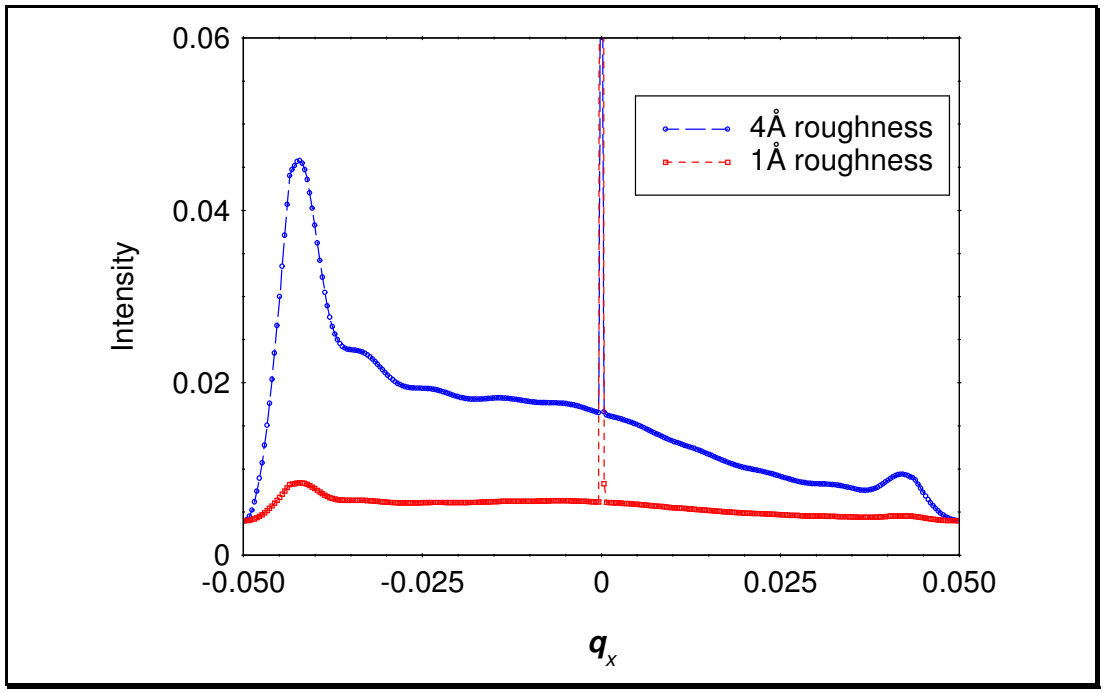

Figure 2.20: Effect of roughness on a single layer (h=0.5, ξ=200Å).

Figure 2.20 demonstrates the effect of increasing the roughness on a 100Å Cu layer. The increase in the roughness increases the amount of diffuse scatter produced, as would be expected.

2.5.6. Diffuse Scatter from Multilayer Structures.

As discussed previously, within a multilayer structure the roughness at an interface can be correlated, where the interface morphology is replicated from layer to layer, and uncorrelated, where the roughness is independent of other layers. These types of roughness have different effects on the diffuse scatter. They can be demonstrated with the use of full reciprocal space maps, constructed from several tranvserse diffuse simulations with the detector angle incremented between each scan.

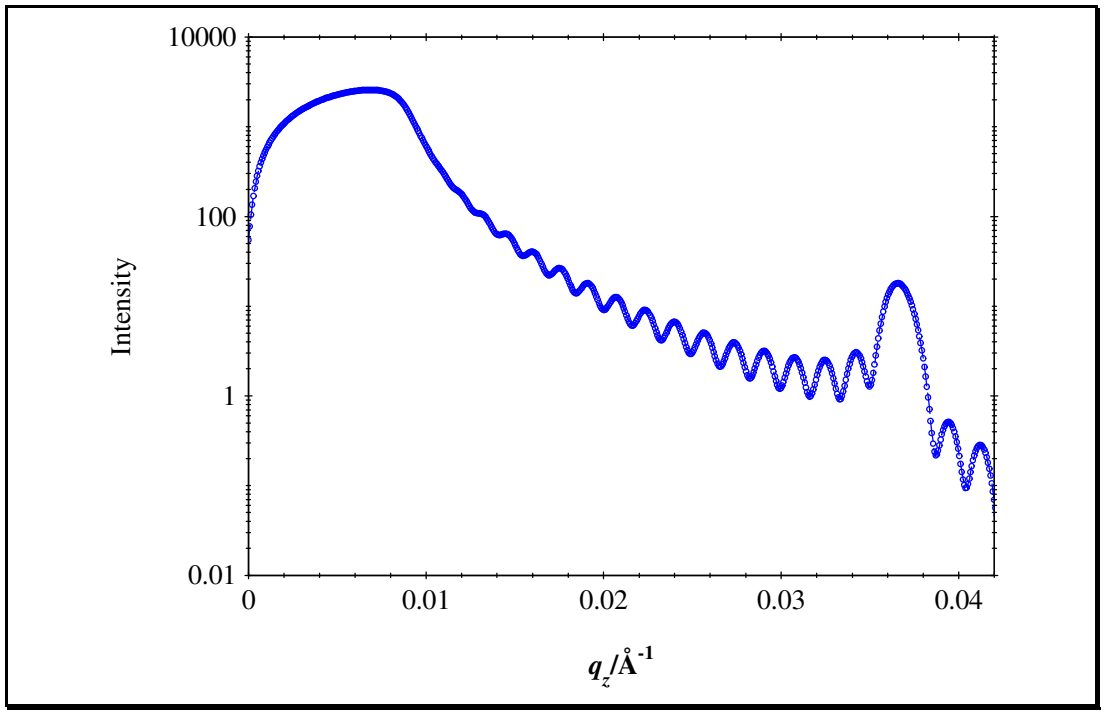

Figure 2.21: Simulation of the specular scatter from the Co/Cu multilayer used for full reciprocal space maps.

Figure 2.21 shows the specular scan of the $\{Co20Å/Cu8Å\}_{20}$ multilayer, with 4Å roughness at all of the interfaces, and 2Å roughness on the substrate. This structure was used to construct the full reciprocal space maps.

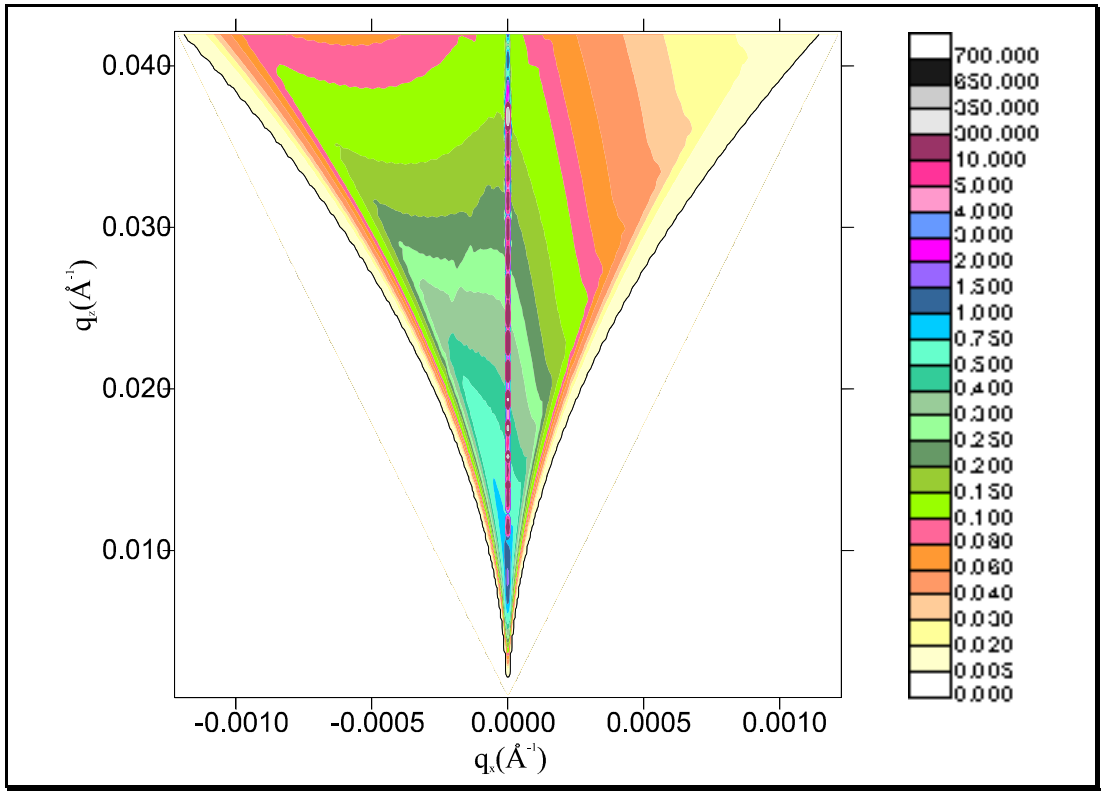

Figure 2.22: Full reciprocal space map of diffuse scatter from a Co/Cu multilayer, where the roughness is totally uncorrelated.

Figure 2.22 is a full reciprocal space map of a $\{Co20Å/Cu8Å\}_{20}$ multilayer, with 4Å uncorrelated roughness at all interfaces, and 2Å roughness on the substrate. As can be seen in the figure, the diffuse scatter decays evenly in reciprocal space, with no features present in the scatter. This is the same pattern as from a single layer, with the intensity scaled to the number of layers present in the sample.

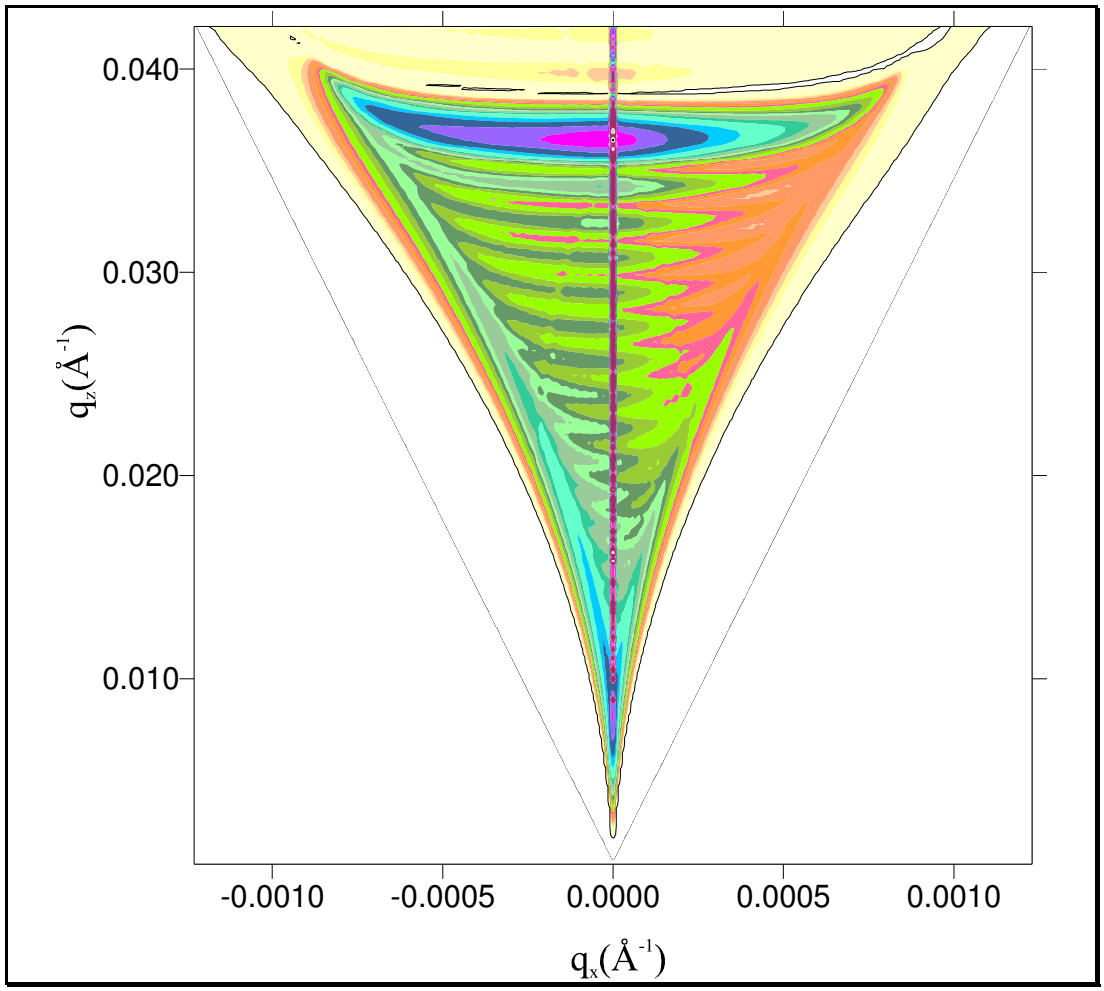

Figure 2.23: Full reciprocal space map of diffuse scatter from a Co/Cu multilayer, where the roughness is totally correlated.

Figure 2.23 shows a full reciprocal space map of the same multilayer, but with totally correlated roughness at the interfaces. In contrast to Figure 2.22, the scatter is confined to regions within reciprocal space. The large increase in intensity is at the Bragg peak position and, if refraction is ignored, extends across constant $\boldsymbol{q}_x$. These sheets of intensity are often called Bragg sheets. V. Holý and T. Baumbach [42] predicted that if refraction is taken into account, these Bragg sheets bend slightly in $\boldsymbol{q}_x$, often called Holý bananas. The scatter is also confined to sheets corresponding to the position of the Kiessig maxima. Therefore, if the roughness is correlated, Kiessig fringes and Bragg peaks are evident in longitudinal diffuse scans.

The different effects of roughness on the diffuse scatter enable the correlated and uncorrelated components of the roughness to be extracted from simulations. The simulations are carried out using commercially available software from Bede Scientific [1], based on the theory outlined above. The parameters are systematically varied until a satisfactory fit is obtained. At least two scans are simulated simultaneously, at different detector angles, and only when both scans are fit by the same set of parameters can the parameters be said to be reliable. The components of the roughness add in quadrature, such that

$$\sigma^2 = \sigma_c^2 + \sigma_u^2 \quad \text{..... (2.21)}$$

The total roughness σ is fixed at the value obtained in the specular simulation.

The simulations are an excellent tool for obtaining reliable parameters to describe the thickness of layers, and the structure and morphology of the interfaces. However, this method of extracting parameters is very time-consuming due to the nature of the iterative procedure used to fit the data, and the complex nature of the calculations.

2.5.7. Born Analysis.

Another method for extracting the correlated roughness from the transverse diffuse data, without recourse to simulation, was developed by Savage *et al* [43]. By assuming that the total roughness σ can be separated out into correlated and uncorrelated components such that

$$\sigma^2 = \sigma_c^2 + \sigma_u^2 \quad \text{..... (2.22)}$$

then the correlated diffuse reflectivity can be written as

$$I_{diff}(correlated) = I_0 \exp\left(-\boldsymbol{q}_z^2 \sigma_u^2\right) \times \left[1 - \exp\left(-\boldsymbol{q}_z^2 \sigma_c^2\right)\right] \quad \text{..... (2.23)}$$

while the true specular reflectivity can be written

$$I_{spec} = I_0 \exp\left[-\boldsymbol{q}_z^2 \left(\sigma_u^2 + \sigma_c^2\right)\right] \quad \text{..... (2.24)}$$

Taking the ratio of these two intensities gives

$$\frac{I_{diff}}{I_{spec}} = \exp\left(\boldsymbol{q}_z^2 \sigma_c^2\right) - 1 \quad \text{..... (2.25)}$$

Therefore, the ratio of the integrated diffuse intensity due to correlated roughness (ie at the Bragg peak) and the true specular intensity at the same point, does not depend on the uncorrelated roughness, but only the correlated component. By determining the total roughness at the interface from the simulations of the specular scatter, it is possible to determine the correlated and uncorrelated components of this roughness.

This analysis assumes an infinite correlation length, and that there is a high degree of correlation throughout the multilayer. This high degree of correlation is important, since there will be a component of the uncorrelated scatter present at the Bragg peak. If this is large, the value for the correlated roughness obtained from this analysis will be an over-estimate.

2.6. Summary.

In this chapter, the use of x-ray scattering as a characterisation tool has been outlined, at both a routine and more advanced level. At the routine level, it is used to gain information about the thickness of the repeat unit within a multilayer, and the total thickness of the sample. This information can then be used in the growth procedure to obtain the required thickness in subsequent samples. At the more advanced level, the diffuse scatter can be utilised, in conjunction with the simulation programs, to determine physical parameters concerning the roughness at interfaces and the length-scale of this roughness. This can be an involved and lengthy process, so it is only undertaken on samples where the structural characteristics play an important role in the physical properties of the samples. Such a study is given in Chapter 4.

Chapter 3: MBE Growth, Magnetic and Electron Transport Properties.

3.1. Introduction.

People have been working for decades on combinations of transition and noble metals, in both thin films and granular alloys. An interaction was predicted between the nuclear spins of clusters of impurities embedded in a metallic host. This interaction was predicted by Rudderman and Kittel [44], and soon afterwards by Kasuya [45] and Yosida [46], so it is known as the RKKY interaction. Where an impurity is present, the conduction electrons of the host rearrange to screen out the impurity. Intuitively one would expect this charge to decay uniformly as a function of distance from the impurity. However, the charge density is predicted to oscillate as a function of distance, due to a sharp cut-off in the momentum distribution of the electrons. These oscillations are known as Friedel oscillations. If the impurity is magnetic, oscillations in the spin density are also observed, leading to an interaction between impurities which is either ferro- or anti-ferromagnetic depending on the separation of the magnetic clusters.

A similar RKKY-type interaction between the magnetic materials in a multilayer would be expected, due to the nature of the de-localised electrons within the metallic multilayers, with the interface being the pertubation instead of the impurity in the alloy. However, in earlier work on magnetic multilayers only a ferromagnetic interaction between the magnetic layers, separated by thin non-magnetic spacers, was observed. With improvements in the structural quality of the layers through improvements in the growth procedures, anti-ferromagnetic (AF) coupling was seen in Gd/Y multilayers [2] in 1986. In addition to this, oscillations in the sign of the exchange coupling as a function of spacer thickness were observed. The same effects were seen in multilayers composed of transition/noble metals in 1990, firstly in Fe/Cr and Co/Ru multilayers [47] and subsequently in Co/Cu multilayers [48]. The AF-coupling can be overcome by an applied magnetic field, which causes the magnetisations of the ferromagnetic layers to lie parallel to the applied field. However, the oscillation period predicted by the RKKY theory was too short to explain the long periods found experimentally. This could be rectified by 'aliasing', as explained in section 3.3.2.

A consequence of the anti-ferromagnetic coupling of the magnetic layers within a multilayer is the Giant Magnetoresistance (GMR). This effect, first observed in 1988 in Fe/Cr multilayers [3], is defined as the difference in the resistivity in zero and saturated field with respect to the saturated value, and can be higher than 100% at room temperature. This effect was attributed to the differences between the scattering rates of the two electron spin channels. Initially it was thought that the GMR required an AF alignment. It was soon realised that this was not a prerequisite; only an imperfect alignment of the magnetisations in zero field was necessary. The mean-free path of the electrons had to be long compared to the thickness of the layers, otherwise no effect would be seen.

In this chapter, an outline of the causes of spin-dependent scattering of electrons and how the GMR arises from these is detailed, along with some of the theories to explain

the GMR and oscillatory exchange coupling. The experimental details of the methods used to characterise the electronic transport and the magnetic properties of the magnetic multilayers are given.

3.2. Giant Magnetoresistance.

In a ferromagnet the two spins of an electron can be considered as independent since the spin-flip scattering process is negligible below the magnetic ordering temperature [49]. With this assumption, the current can be considered as being carried in parallel by two independent spin channels. It is usually assumed that the sp-band electrons are the main carriers as these have a low effective mass due to the broad nature of the band. In contrast, the d-bands are narrow and the effective mass is high. However, these d-bands play an important role in the resistivity as they provide empty states into which the conduction electrons can scatter. The density of states at the Fermi level can be significantly different for each spin for the strong ferromagnetic metals, Co and Ni. This leads to substantially different resistivities for each spin channel. Figure 3.1 illustrates a schematic diagram of the density of states for ferromagnetic Fe, Co and Ni .

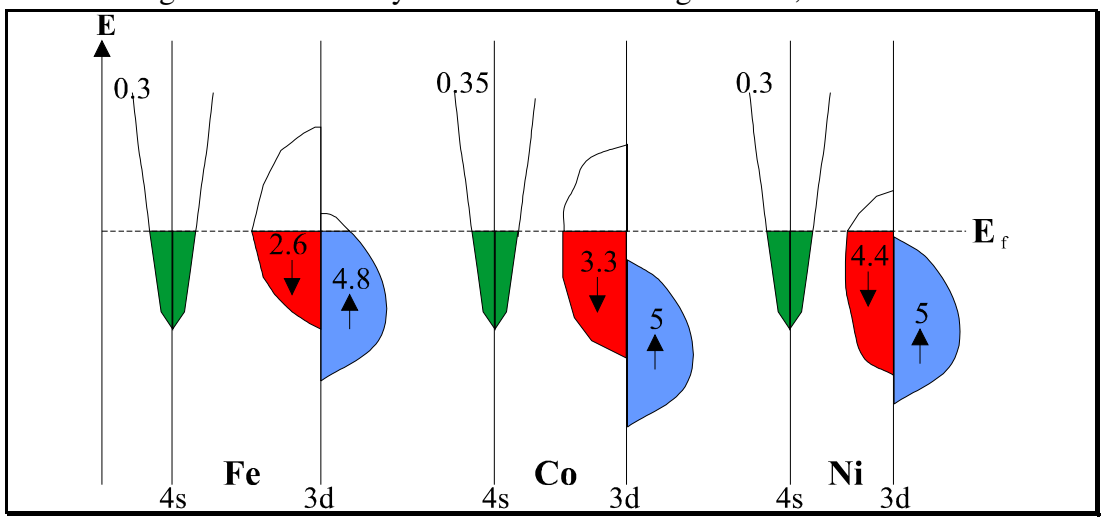

Figure 3.1: Schematic diagram of the density of states in the sp- and d-bands of Fe, Co and Ni (after [50]).

The equivalent resistor network model, developed by J. Mathon [50], gives a simple model of the GMR in magnetic multilayers using these differences in the density of states. The resistivity for each spin channel is equal in the non-magnetic spacer as the density of states does not depend on the spin of the electron. However, the density of states in a ferromagnetic metal is spin dependent, as illustrated schematically in Figure 3.1. Hence, the resistivity is spin-dependent within the ferromagnetic layer. When the magnetic layers are in an anti-parallel alignment, the resistivity of each spin channel is the same. However, when the magnetic layers are in a parallel alignment, the resistivity of the majority spin channel is much lower than that of the minority carriers, so this spin channel produces a low resistance path for the current. This difference in the resistivity between the two alignments is the cause of the GMR.

Although this was developed with the difference in the resistivity due to the differences in bulk scattering rates in the ferromagnet, the same argument for the GMR can be used irrespective of where the spin-dependent scattering occurs. In Fe, the densities of states at the Fermi energy for the majority and minority carriers do not differ as much as in Co, due to a dip in the minority spin at the Fermi level [51]. Therefore, there is very

little difference in the bulk scattering rates; consequently, bulk scattering cannot be a major contributor to the GMR. Experimentally, the scattering of electrons at an interface within a multilayer is thought to dominate the GMR in both Fe-based and Co-based systems [52]. Whether this interface scattering is due to defects, roughness or purely a reflection is not normally important, as long as it is spin-dependent.

There has been much speculation into the underlying reasons why the magnitude of the GMR is much larger in sputtered multilayers than in MBE-grown multilayers. This gives an indication that the structure and interface morphology of the multilayer plays a crucial role in the GMR. There has been a great deal of research into the effect of the structure of Co/Cu multilayers on the GMR. In most cases the interfacial roughness has played a crucial role in the magnitude of the GMR and AF-coupling, with the GMR decreasing with increasing roughness [8,53,54]. However, it is still not clear whether the roughness is the cause of the lower GMR values in MBE-grown multilayers as compared to sputtered systems. Therefore, a careful study of the interface roughness and its effect on the GMR in Co/Cu(111) multilayers grown by MBE is carried out in this thesis using x-ray characterisation techniques.

3.3. Oscillations in the GMR and Exchange Coupling.

3.3.1. Experimental Observations of the Oscillatory Exchange Coupling.

In 1990, Parkin *et al* found that the GMR oscillated as a function of the spacer thickness in Co/Ru multilayers [47] and in 1991 in Co/Cu multilayers [48]. These oscillations were found to coincide with the oscillations in the exchange coupling. The oscillations in the GMR in Co/Cu multilayers are shown in Figure 3.2. The GMR is a maximum when the layers are AF-coupled dropping to low values when there is little AF-coupling.

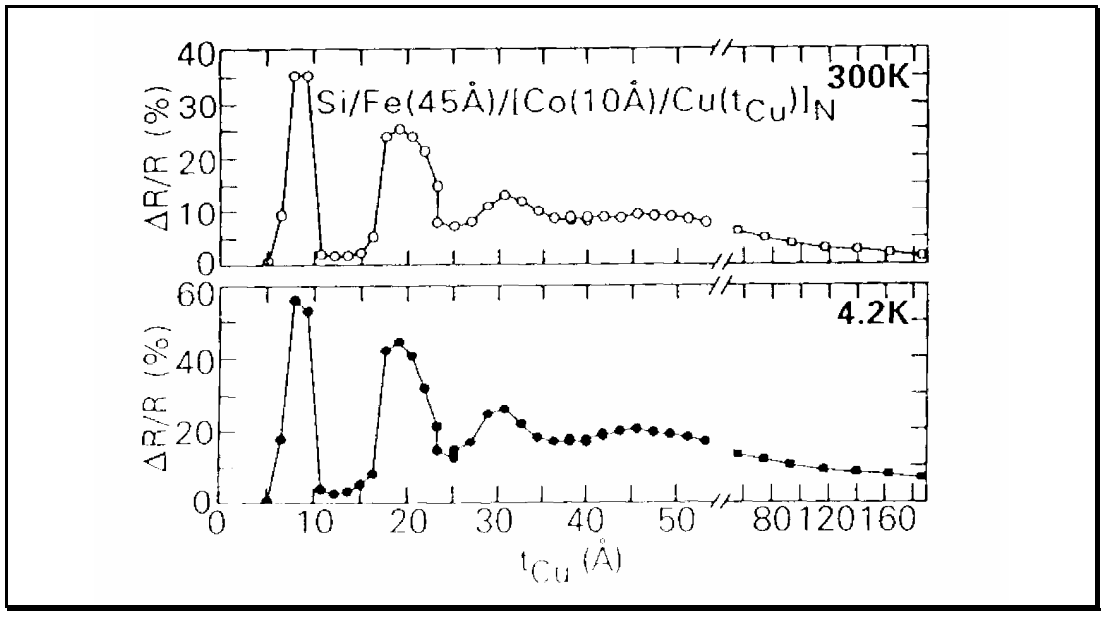

Figure 3.2: Oscillations in the GMR as a function of spacer thickness in Co/Cu multilayers (from [55]).

In the early work on GMR materials the majority of the oscillation periods observed were of the order of 10Å. This led to speculation that the period was independent of the materials used [56]. However, the phase of the oscillations in all of the multilayers was

dependent on the magnetic material. The exception to this 10Å period was when Cr was used as a spacer, when the period was significantly longer. The oscillations in the coupling, with a period of 18Å, were seen directly by Unguris *et al* [57] using SEMPA (Scanning Electron Microscopy with Polarisation Analysis) on an Fe/Cr/Fe wedged sample. It was thought that the long period was due to the anti-ferromagnetic properties of the Cr spacer. Recently however, a period of 17Å for Fe/Au/Fe(100) using the same apparatus has been observed [58], indicating that the long period is a general phenomenon of magnetic multilayers with the period of oscillation dependent on the materials used.

3.3.2. Theoretical Models of the Oscillatory Exchange Coupling.

One theoretical model developed to explain the oscillatory behaviour was the RKKY model. This was based on the model of dilute magnetic impurities in a non-magnetic host. This simple model was applied to magnetic multilayers, where the host metal was now the spacer, and the interfaces the pertubation within the host. However, this free-electron model only predicted a short oscillation period, and not the 10Å period observed experimentally in many systems. To explain this, 'aliasing' was introduced into the RKKY model [59]. In the free electron model, the periodicity of the lattice was not considered. By sampling the short period oscillation at integral points, corresponding to the lattice points, a beating occured between the two frequencies, causing an apparent long period oscillation. This is illustrated in Figure 3.3.

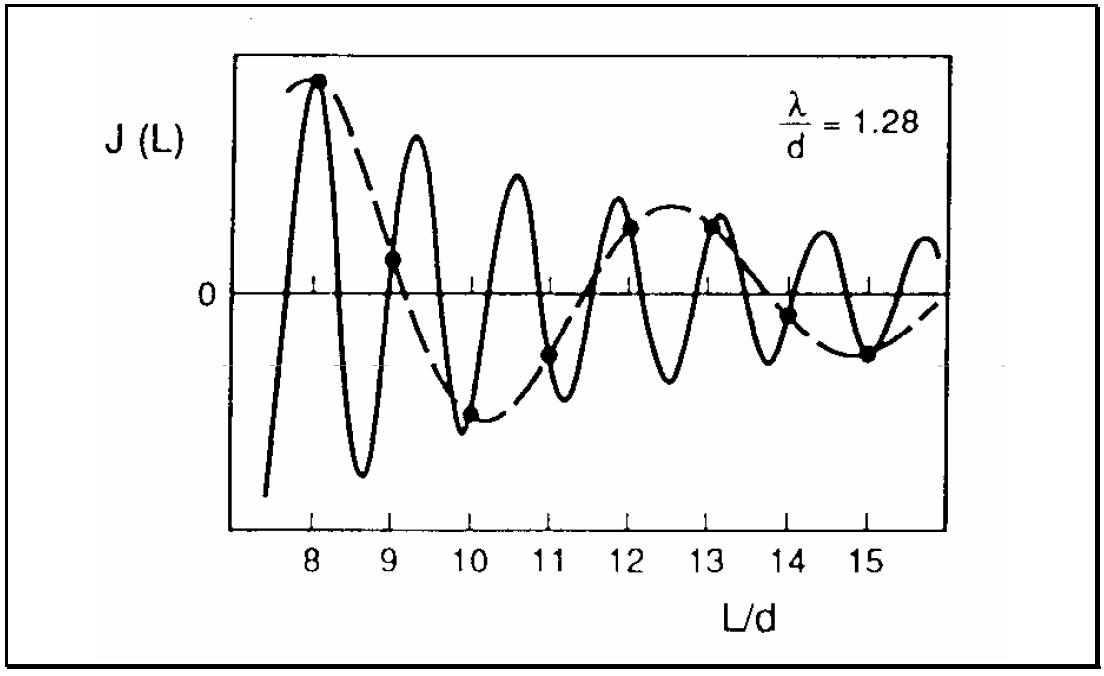

Figure 3.3: RKKY-like oscillations with a period λ (solid line) showing the longer period (dashed line) obtained by sampling the function only at integral spacing, d, between the atomic planes (from [59]).

Bruno and Chappert [60] developed this model to calculate the oscillation periods for many spacer materials. Their calculations of the long period agree well with the experimental data available.

Stiles [61] calculated the oscillation periods for many combinations of metals using a model based on the Fermi surface of the spacer material. This model demonstrated that

the oscillations in the exchange coupling arose directly from the extremal spanning vectors of the Fermi surface of the spacer layer. These spanning vectors corresponded to an oscillation period in the coupling. These predicted both the long and short periods one would expect to observe experimentally, unlike the simple RKKY-like model. The periods calculated agreed well with experiment in most cases.

3.4. Electron Channelling.

Hood and Falicov [12] first suggested that specular scattering of electrons within magnetic multilayers may play an important role in the GMR. A specular reflection is one in which there is no change in the parallel component of the momentum of the electron. These reflections have been observed for many years at the interface of a noble metal and vacuum (see, for example, [13]). Recently, noble metals, such as Ag or Au, have been utilised as the capping layer of both a trilayer [62] and a spin-valve [63] to enhance the GMR by effectively reflecting the electron back through the system. Specular reflections from NiO pinning layers in symmetric spin-valves have also been reported [64]. However, it should be possible to enhance the GMR of certain multilayers by utilising these specular reflections at interfaces within the superlattice.

Stiles [14] calculated the reflection probabilities of the majority and minority electrons. The reflection probabilities averaged over the whole Fermi surface, calculated by Stiles, are given in Table 3.1. However, these probabilities are not constant over the whole Fermi surface. At certain points on the Fermi surface, there may be complete reflection or transmission.

	Into Magnetic layer		From Magnetic layer	
	minority	majority	minority	majority
Ag/Fe (001)	0.84	0.14	0.86	0.64
Au/Fe (001)	0.83	0.16	0.84	0.63
Cu/Co (001)	0.51	0.21	0.63	0.05
Cu/Co (111)	0.46	0.27	0.67	0.06
Cu/Co (110)	0.56	0.34	0.71	0.08
Cu/Ni (001)	0.28	0.27	0.67	0.07
Cu/Ni (111)	0.20	0.33	0.62	0.08
Cu/Ni (110)	0.38	0.37	0.69	0.40

Table 3.1: Reflection probabilities of electrons, averaged over the Fermi surface (after Stiles).

Electron channelling occurs when an electron is confined to a layer due to strong reflections at both interfaces of the layer. A GMR is observed if one electron spin channel is confined to a layer of low resistivity when the magnetic layers are in the parallel alignment, and there is no confinement of electrons for the anti-parallel alignment. This can occur if there is a large asymmetry in the reflection probabilities for the two electron spins at the interface from the spacer into the ferromagnet.

When the magnetisations are anti-parallel, each spin channel has a high reflection probability at only one interface within the spacer, with no confinement of the electron possible in the layer. However, when the magnetisations are parallel, one spin channel may be reflected at both interfaces within the spacer, thus creating confinement of the electron in the spacer layer. This confinement is also known as a quantum well state. If the resistivity of the spacer layer is much less than the magnetic layer, this confinement of a spin channel of electrons becomes a low resistance shunt. Therefore, this spin-dependent specular reflection can create a GMR without spin-dependent defect or bulk scattering. This electron channelling should also cause a decrease in the saturated resistivity.

In the Fe/Au study in chapter 5, the reflection coefficients for the (100) orientation indicate that this is a very good candidate to exhibit electron channelling. It is not possible to calculate the probabilities for the (111) orientation at present as the lattice parameters are not well-matched, but the spin-asymmetry in the reflection coefficients is expected to be much reduced [65]. This gives a system with which to compare the (100) in an attempt to establish whether electron channelling is a mechanism for the GMR in Fe/Au(100) multilayers.

3.5. Multilayer Growth by MBE.

All of the multilayers charaterised in this work were manufactured using the VG-80 MBE machine at the University of Leeds. Full details of the MBE machine have been reported in previous PhD theses from the University of Leeds [66,67] and consequently will not be repeated here. However, it is important to note that Fe and Co are deposited from an e-gun and the Cu and Au from a Knudsen cell.

Due to the nature of the studies, having to investigate the behaviour as a function of the spacer thickness, long pieces of substrate were used and natural wedges were grown. The practical aspects of this are discussed in the following section.

3.5.1. Natural Wedges.

A natural wedge is a method of obtaining a varying layer thickness along the length of a substrate. This variation is obtained by the shape of the flux from the evaporation source. By placing one end of the substrate close to and the other end away from the source, a gradient in the thickness is obtained. The thickness varies as the square of the distance from the source, as shown in Figure 3.4, and approximately doubles over a 50mm long substrate, creating a gradient of approximately 0.1-0.5Å/mm depending on the thickness of the layer. The substrate is then cleaved, using a diamond saw, into pieces 2.5mm wide, as this is convenient for the electron transport measurements. The variation of the thickness across these 2.5mm wide samples was negligible due to the shallow thickness gradient. This is only true from a Knudsen cell with a non-rotating substrate. The substrate is rotated if a layer of constant thickness is required.

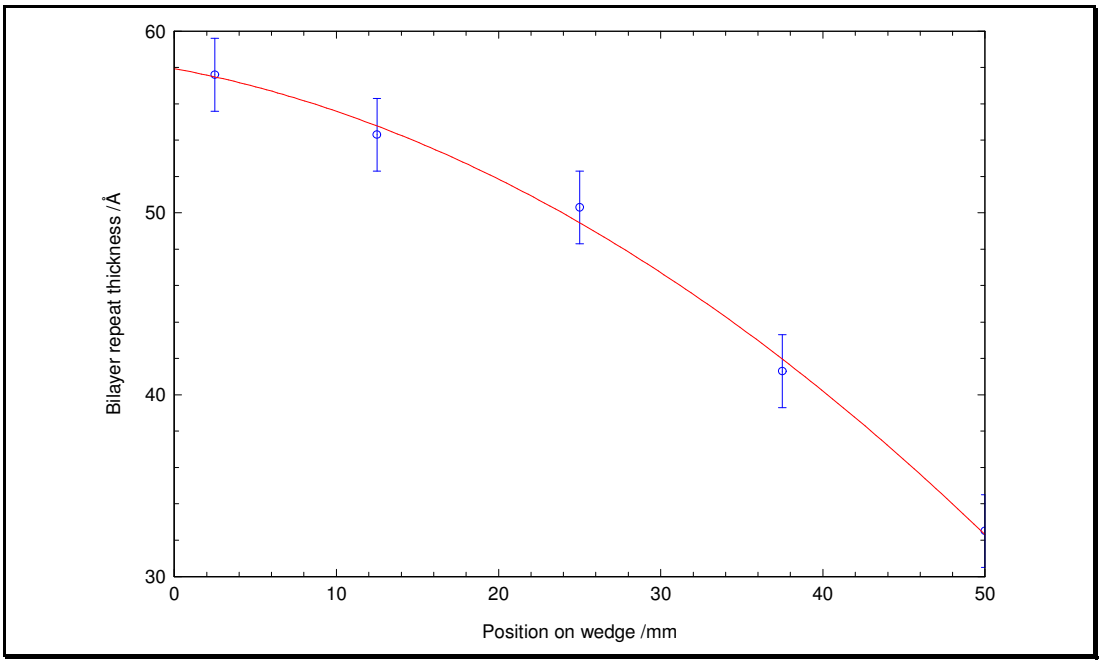

Figure 3.4: The variation of the layer thickness as a function of the position on the wedge.

This growth technique provides an effective method of studying the properties of multilayers as a function of the thickness of a layer.

3.6. Measurement of the GMR.

The GMR measurements were carried out at 4.2K in a Thor cryostat, developed to perform the necessary transport measurements. An outline of the cryostat, and the modifications made to the cryostat are given below, along with the method used to measure the GMR.

3.6.1. The Thor Cryostat.

The cryostat is a gas-flow cryostat, built by Thor in the 1980's. It consists of a nitrogen outer jacket and an inner helium reservoir. There is a vacuum space between the reservoirs and one on the outside of the nitrogen jacket. The vacuum spaces are connected at the top of the cryostat, and are kept at approximately 10^{-6}mbar by a diffusion pump backed by a rotary vane pump. The cryostat has a helium capacity of 4 litres and a nitrogen capacity of 6 litres. A diagram of the cryostat is shown in Figure 3.5.

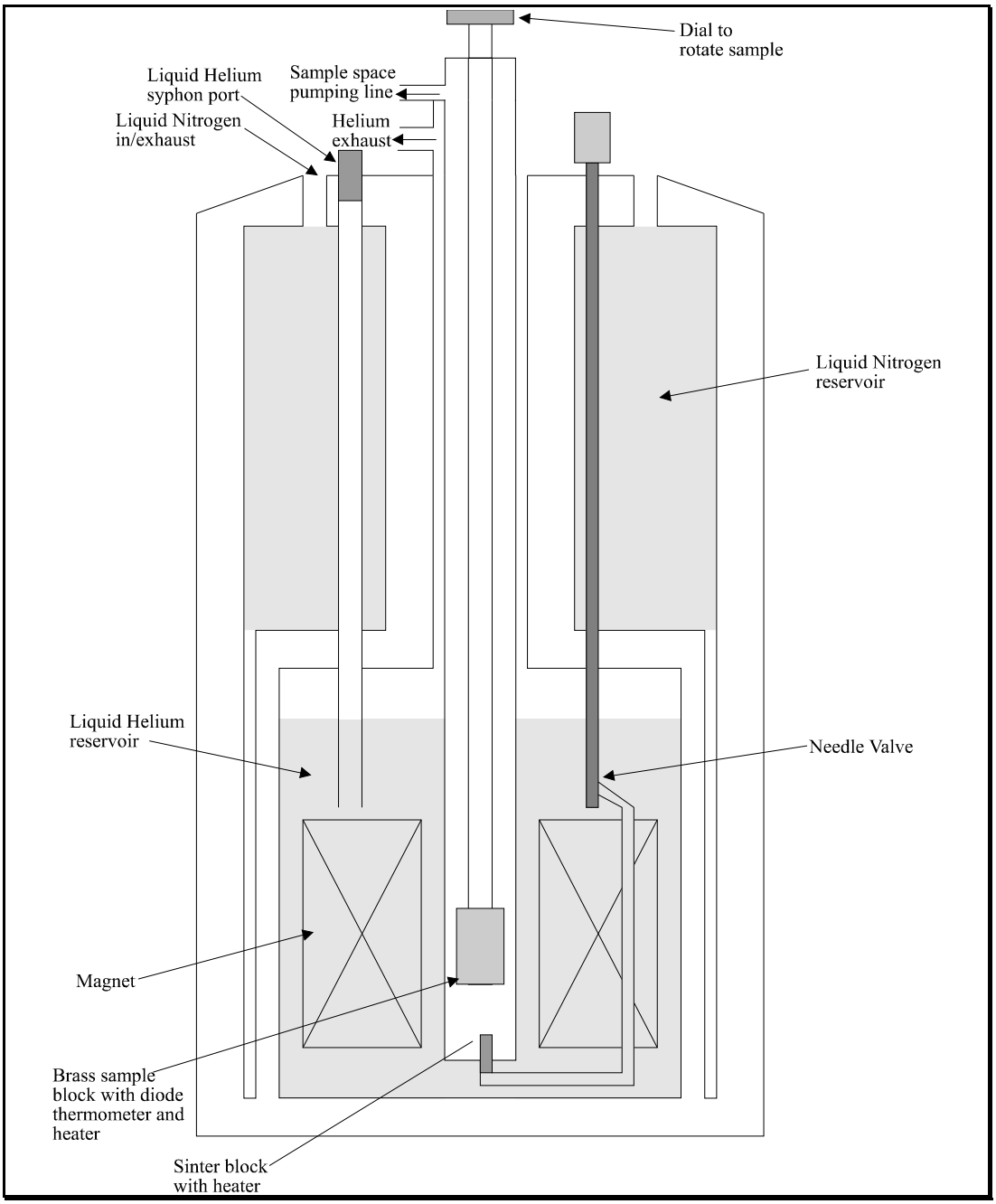

Figure 3.5: Schematic diagram of the Thor cryostat.

Liquid helium is pumped into a sinter block at the bottom of the sample space through a needle valve. The sinter block contains a heater and a thermocouple. The heater controls the temperature of the gas up the sample space, and hence the temperature of the sample. The thermocouple measures the temperature of the gas passing through the sample space. For measurements at 4.2K the heater is left off and the liquid allowed through the needle valve to cover the sample.

The magnet is of the split pair design, and magnetic fields of up to 4T are obtainable. A reversing switch for the magnet power supply has been built, to make field sweeps of -4 to +4T possible. The current is supplied by a Cryogenic 120A power supply, with a current of 24.5A in the magnet producing a field of 1T.

3.5.2. Resistivity Measurement.

The sample stick is composed of a hollow stainless steel tube, with a brass block fixed to the end. The sample, heater and thermometer are situated on this block. The thermometer is a GaAlAs diode thermometer, calibrated using a RhFe secondary standard thermometer. It is possible to mount the samples in two different planes, so the field direction can be varied within the plane of the sample or at different angles to the sample normal.

The resistivity measurement is carried out using a 4-probe pressure contact method, and two samples can be measured during one experiment. The probes are gold-plated contacts equally spaced 2.54mm apart, each with a diameter of 2mm. A current of typically 10mA, from a Lakeshore current supply, is passed through each sample and the voltage across the sample measured. The measurement is repeated with the current reversed to eliminate thermal voltages. The resistivity is given by

$$\rho = \frac{Vt}{I} CF \quad \text{..... (3.1)}$$

where V is the voltage, I the current, t the total thickness of the sample and CF a correction factor. The correction factor is purely a geometrical ratio of the spacing between the voltage probes and the width of the sample. When the spacing between the voltage probes is greater than the width of the sample, $CF=1$. For this reason, the width of the sample was fixed at 2.5mm. The current was parallel to the applied field.

3.6.3. Experimental Control.

Three main types of measurement can be carried out in the cryostat:

(i) the giant magnetoresistance (GMR),
(ii) the anisotropic magnetoresistance (AMR), where the resistance as a function of angle between the current and applied field is investigated,
(iii) resistivity as a function of temperature.

All of these can be carried out at any temperature from 4.2K. A block diagram of the apparatus is shown in Figure 3.6.

The PC utlised software written at the University of Leeds to control the necessary equipment to make measurements. There were several procedures carried out by the PC. Where a voltage was measured, such as across the samples, the thermometry and an output from the magnet power supply, the voltage outputs were connected to a multiplexer. The use of a multiplexer enabled a single voltmeter, a Keighley 182 digital voltmeter, to be utilised for all of the voltage measurements. This voltmeter was read directly by the PC. In addition, the multiplexer supplied the current to the samples, from a Lakeshore current source, and a built-in $10\mu A$ current source supplied the diode thermometer. The software ensured the correct multiplexer channel was selected, and the voltage measurements were recorded. In addition to these, the software was also responsible for the temperature control and the ramping of the magnetic field to the correct value.

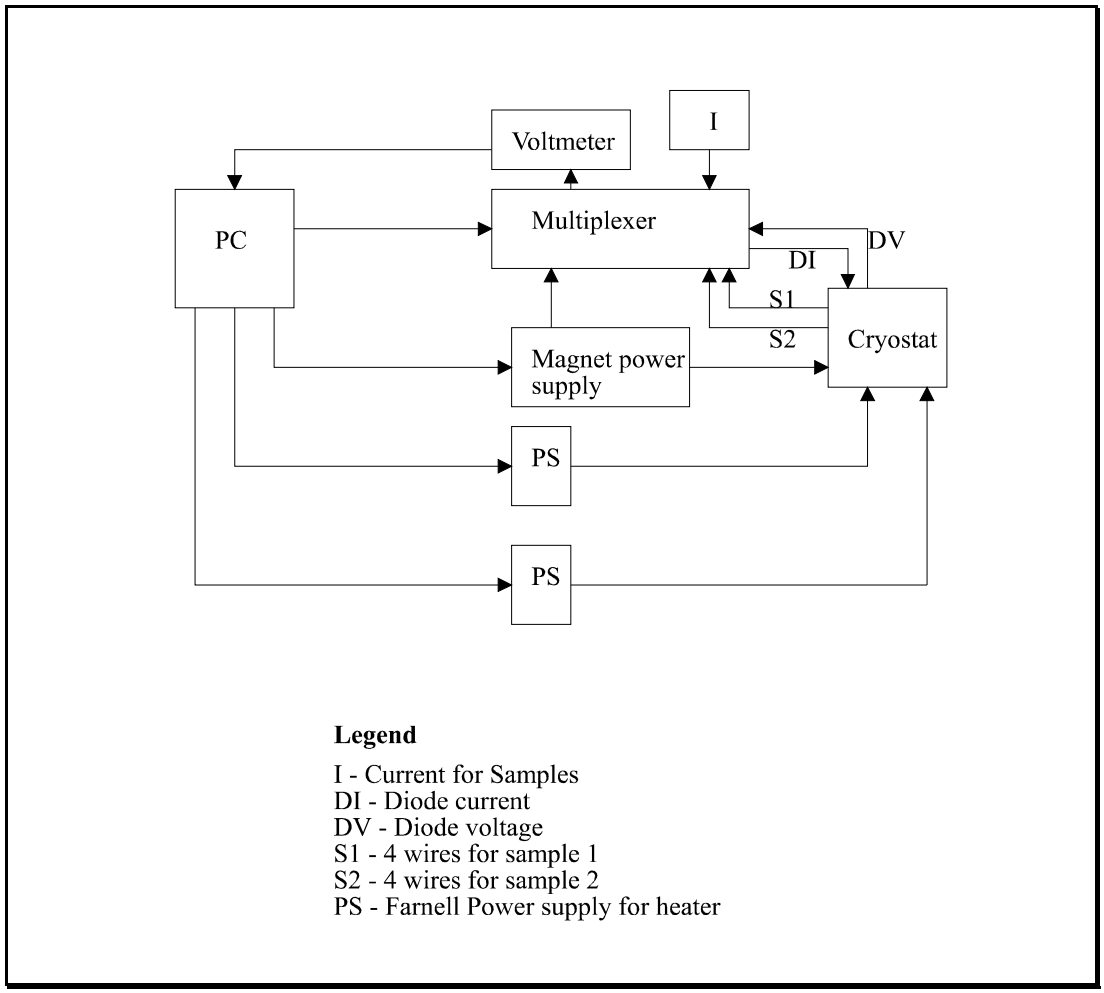

Figure 3.6: Block diagram of equipment for cryostat.

For temperature control, the PC software used PI control to calculate the power necessary to obtain the required temperature. The heaters, one on the sinter block in the cryostat and the other on the sample stick, were each connected to a Farnell 30V-1A power supply, and the required power output of each supply set by the PC.

The software also controlled the ramping of the magnet power supply. The back-emf from the magnet was monitored by the PC, via the multiplexer, and the field ramped at a pre-determined rate on the power supply to the required field.

3.7. Magneto-Optical Kerr Effect (MOKE).

Magnetic measurements were necessary in order to gain information about the magnetic properties of the multilayers. The main measurement performed to obtain this information is the Magneto-Optical Kerr Effect (MOKE). This is a relatively simple experimental technique, utilising the interaction of polarised light with magnetic materials. There are many reviews on this topic [68,69], and the experimental set-up at the University of Leeds is one of the main topics in the thesis of Helen Laidler [70], where a detailed description can be found.

In this thesis, the MOKE data was used to determine the fraction of AF-coupling present in the multilayer. This is determined from the remanence of the hysteresis loop, as this gives a direct measure of the volume fraction of AF-coupling present in the sample. For perfect AF-coupling there is zero magnetic remanence.

3.7.1. MOKE Apparatus.

The apparatus used for this thesis was developed by J. Xu and H. Laidler, and a full account of this development is given in H. Laidler's PhD thesis [70]. A brief overview of the equipment set-up, and the necessary conditions required to perform an experiment are given here.

Magneto-optical effects in ferromagnetic materials occur from the interaction between the electromagnetic wave and the net spin polarisation present in the material. If the incident light is polarised in the s- or p-plane, then the light reflected from a ferromagnetic material will be elliptical and the polariation rotated. The rotation produced is detected by using crossed polarisers.

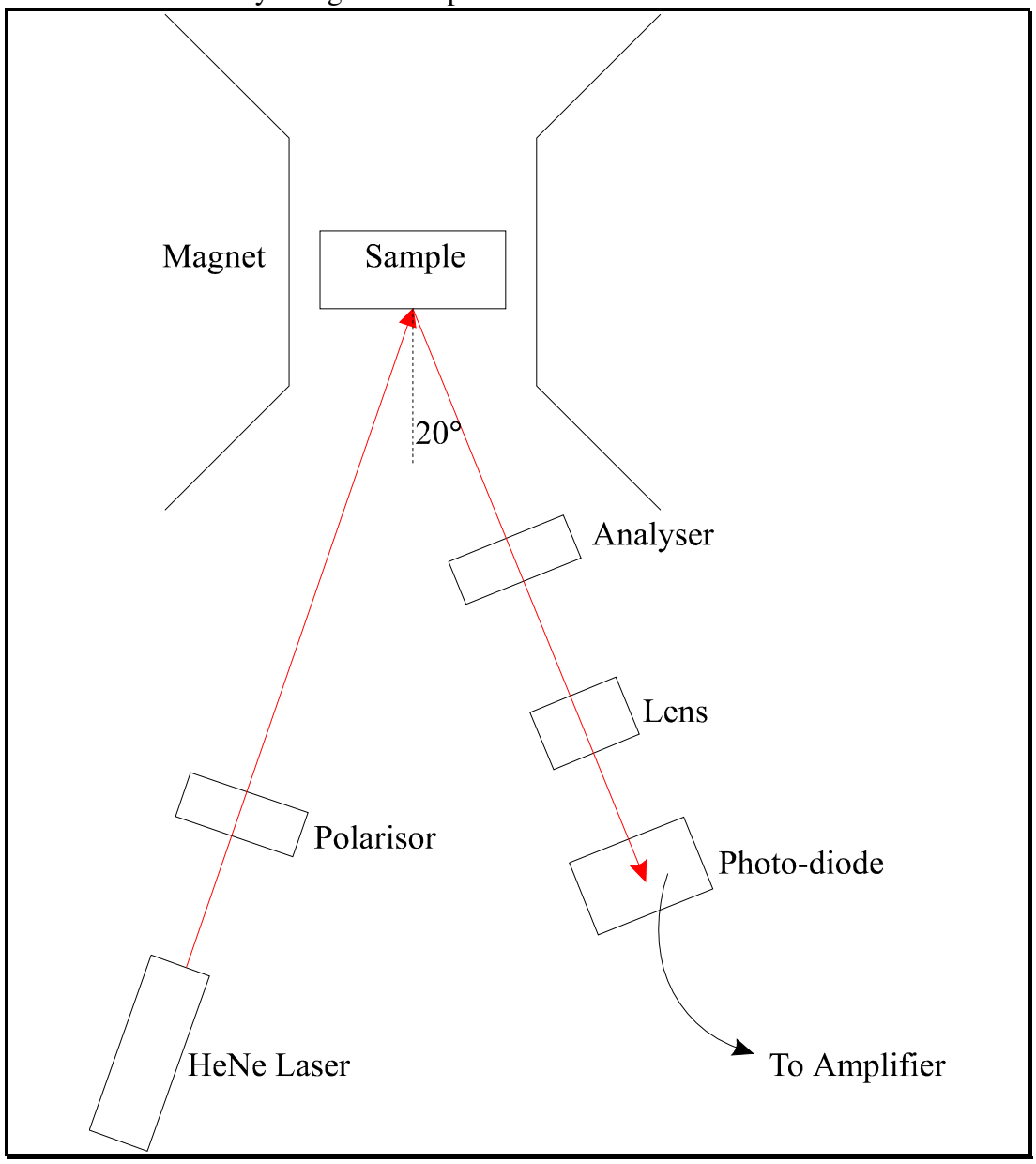

Figure 3.7: Schematic diagram of the MOKE apparatus.

Figure 3.7 shows a schematic representation of the equipment. All of the components, with the exception of the magnet, are mounted on an optical table. The magnet is a water-cooled electromagnet, with fields of up to 2T possible, which is isolated from the

table to prevent problems associated with vibration. The field is read by a calibrated Hall probe, mounted on one of the pole pieces.

Polarised light is produced by a HeNe laser, which is passed through another polarisor to ensure the light is fully p-plane polarised. This light is incident on the sample at approximately 20° to the sample normal. The optimum angle is 45° [69], but this is not possible due to the size of the electromagnet. This means the size of Kerr rotation is smaller than for the optimum angle. The sample is mounted using wax onto a non-magnetic, rigid holder and placed on an optical rail attached to the optical table between the pole pieces of the magnet.

The reflected light is passed through an identical analysing polarisor, set close to extinction. It seems logical that the analyser should be set at extinction, so that no p-plane polarised light is detected. However, Bader and Erskine [69] showed by a calculation of the detected intensity that this was not the case, but that the condition for the offset angle is given by

$$e < \tan^2 \theta_A \quad \text{..... (3.2)}$$

where e is the extinction ratio of the analyser and θ_A is the angle away from extinction. The quoted value for the extinction ratio of the polarisors is 10^{-5}, giving $\theta_A > 0.18°$. In fact, H. Laidler showed that for Co/Cu multilayers the best response was obtained when the analyser was 0.3° away from extinction [70]. If this condition was not satisfied, asymmetry was seen in the hysteresis loop and the values found for the remanence were not valid.

3.8. Summary

This chapter has briefly outlined the development of the theoretical and experimental aspects of the GMR and MOKE. These two techniques are used extensively in this thesis to determine the electrical and magnetic properties of Co/Cu and Fe/Au multilayers. In chapter 4, these are used in a study on Co/Cu(111), and more extensively in chapter 5 where the electron transport and magnetic properties of Fe/Au(100) and (111) are compared.

Chapter 4: The Effect of Correlated Roughness on the GMR in MBE-grown Co/Cu Multilayers.

4.1. Introduction

There have been many studies on different transition/noble metal multilayers since the discovery of the giant magnetoresistance (GMR) in 1988 [3]. One of the most studied is Co/Cu, both grown by sputtering and by MBE. It is generally agreed that smooth, flat interfaces are necessary to produce large GMR values in Co/Cu multilayers. Ueda *et al* [54] annealed Co/Cu multilayers and found the increase in the roughness both reduced the anti-ferromagnetic coupling and the GMR. Harp *et al* [71] deposited multilayers at different substrate temperatures (0°C and 150°C), and found the roughness of the multilayer grown at the elevated temperature was lower that that of the other multilayer. The lower roughness corresponded to the higher GMR. In addition, the amount of AF coupling in these samples was the same, so the differences in the GMR were not due to changes in the AF coupling but to the interface morphology. Other studies have also confirmed this trend of roughness with GMR [72,73]. In contrast to these results, Yoshizaki and Kingetsu [74,75] reported that smoother interfaces actually decreased the GMR. They attributed this to the wavelength of the roughness being of the order of tens of Å, in comparison to hundreds of Å found in other systems. This suggested there was a critical wavelength of roughness for a maximum GMR. Suzuki *et al* [76] also reported that increased interface roughness enhanced the GMR, in line with a theoretical calculation by Oguri *et al* [77].

The grain size within the multilayer has been observed to affect the GMR. Modak *et al* [78] have shown that the GMR increased with increasing grain size. However, the presence of grain boundaries can have another indirect influence on the GMR. It is well established that Co/Cu multilayers grown by sputtering exhibit oscillations in the anti-ferromagnetic exchange coupling between the Co layers [47]. However, these oscillations are not readily observed in MBE-grown multilayers. The GMR in sputtered multilayers is generally much higher than for MBE systems, despite the high crystalline quality of the MBE-grown multilayers. This discrepancy has often been attributed to pin-hole formation in the MBE multilayers [55]. Pin-holes are formed if Co diffuses down grain boundaries during deposition, leading to adjacent Co layers being connected through the Cu spacer layer. This causes the degree of AF-coupling to be reduced. However, Yang *et al* [79] characterised Co/Cu samples using TEM and found no evidence for any pin-hole formation. Recently, signs that these oscillations are present in the exchange coupling have been seen for MBE multilayers [80,41].

In the majority of studies of effects of roughness on the GMR, the measure of interfacial roughness used is the height of the first Bragg peak in the x-ray reflectivity. However, we have already seen that this height can be affected by factors other than the

roughness, so a more detailed measure of the interface roughness is required. Simulations of the specular scatter are used to extract the thickness and roughness of individual layers in the multilayer. By utilising the diffuse scatter, both at grazing incidence and in the high angle geometry, the lateral structure and degree of correlation at buried interfaces can be accurately determined.

In this study, multilayers were grown at different deposition temperatures in an attempt to vary the interface morphology. By varying the interface morphology, it was hoped to understand the effects of roughness on the GMR. Unlike other studies, diffuse scatter was utilised to determine the components of the roughness, and the length-scale of this roughness. By determining these, it was hoped to clarify the effect of the magnitude of roughness on the GMR, and whether there was an optimum length-scale, as suggested by Yoshizaki and Kingetsu.

In a preliminary experiment by J. Xu [81], the mosaic spread present in the samples was found to decrease with increasing GMR. With this preliminary evidence, an extensive characterisation of these multilayers was undertaken, making use of techniques to study transport, magnetic and structural properties of the multilayers. The x-ray scatter was simulated to determine the effect of the interface roughness and the lateral correlation length on the GMR.

4.2. Sample Preparation.

4.2.1. Growth of the Samples by Molecular Beam Epitaxy (MBE).

The samples were growth in a VG-80 MBE machine at the University of Leeds by J. Xu and M.J. Walker, details of which have been reported in other PhD theses [66,67] and consequently will not be repeated here. The samples were of the natural wedge type where the seed, buffer, Co and cap layers were identical, and the Cu spacer layer thickness was gradually increasing along the substrate. The samples covered the first anti-ferromagnetic coupling peak, which occurs at a thickness of Cu = 7-8Å [81]. The Co thickness was 11Å, and the multilayer consisted of 20 Co/Cu repeat units.

The procedure for the growth was as follows. The sapphire substrate was cleaned in acetone and ethanol and mounted using screws onto a molybdenum block. This was then inserted into the MBE system via a fast entry lock and put into the manipulator in the deposition chamber. The substrate was heated to 950ºC and the Nb seed deposited at 1Å/s. The sample was cooled to the temperature at which the buffer was to be deposited and the Cu buffer grown at 0.2Å/s. It was cooled further to the deposition temperature chosen for the multilayer and this was also grown at 0.2Å/s. A capping layer of Au was deposited to prevent degradation of the sample by oxidation. The substrate was cleaved using a diamond saw into samples with different spacer thickness. This caused a fluctuation in the spacer thickness across the width of each sample of approximately 0.5Å. Table 4.1 shows the relevant deposition temperatures of the different parts of each multilayer. The GMR of all of the parts of the wedge for each deposition temperature were measured to determine the samples which were on the first maximum of the AF peak [81], and these samples were chosen for structural analysis.

Sample	Buffer (°C)	Multilayer (°C)	GMR (%)	ρ_o (μΩcm)	$\Delta\rho$ (μΩcm)
1	375	23	50	9.7	3.2
2	375	100	35	11.1	2.9
3	375	150	22	12.3	2.2

4	250	20	31	11.7	2.8

Table 4.1: Substrate temperature during the deposition of different parts of the multilayer in the four different wedges, with electron transport results for these samples.

In the first three samples the effect of a different multilayer growth temperature on the transport properties was investigated. Sample 4 was to determine whether just the multilayer temperature was important, or if the deposition temperature of the Cu buffer also played a role in the characteristics of the multilayer above it.

4.3. Transport and Magnetic Characterisation.

The first part of the investigation was to determine whether the structures exhibited different transport properties due to the different growth temperatures. This was determined by measuring the GMR at 4.2K. An important consideration was that the samples being studied had the same Cu spacer thickness. Variations in this thickness around the 7Å region could cause large changes in the degree of anti-ferromagnetic coupling between the magnetic layers, and hence a large difference in the GMR. It was necessary to rule out any changes in the GMR being due to this coupling change by comparing the MOKE hysteresis loops. The remanent magnetisation found from these loops indicates the volume-fraction of anti-ferromagnetic coupling present in the multilayer. Confirming these are of a similar value would infer that the changes in the GMR were due to structural, and not magnetic, differences.

4.3.1. GMR and Resistivity.

The GMR and resistivity were measured at 4.2K in a cryostat as described in chapter 3 by K.P Wellock. The GMR curves are shown in Figure 4.1 and show a large decrease in the magnitude of the GMR as the growth temperature of the multilayer was increased. The resistivity also showed an increase with increasing growth temperature but the change in resistivity $(\Delta\rho = \rho_o - \rho_s)$ decreased with GMR. This indicates that the increase in the growth temperature increased the amount of spin-dependent electron scattering within the multilayer. These temperature values are given in Table 4.1.

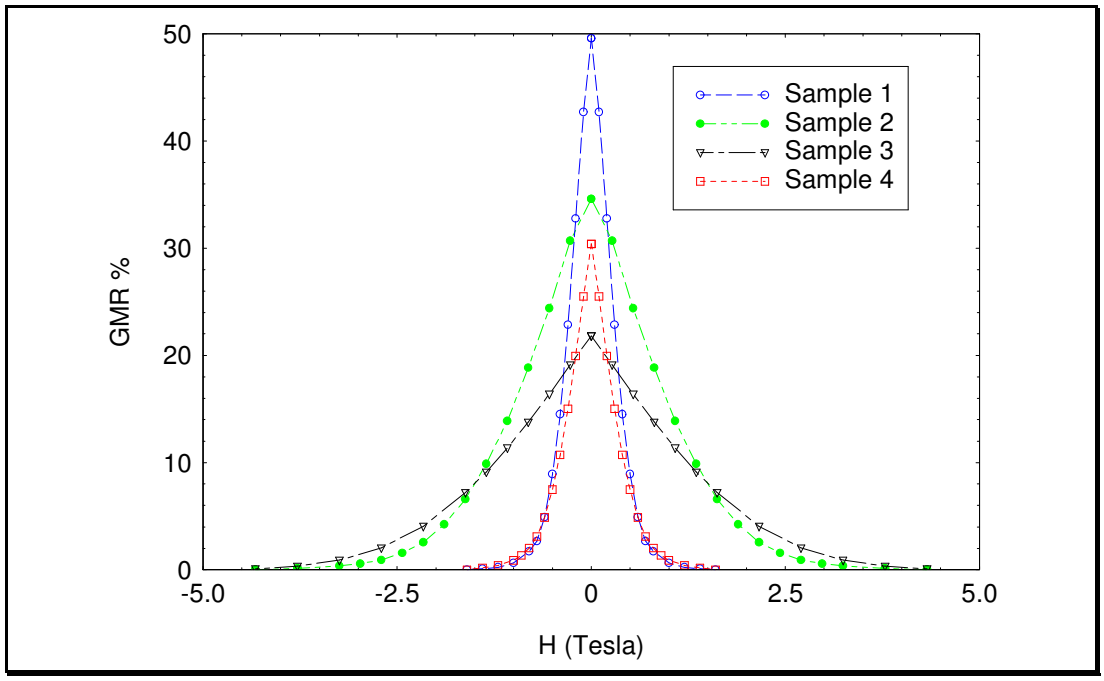

Figure 4.1: GMR at 4.2K, measured by K.P. Wellock at the University of Leeds.

The saturation field of the samples within the series increases with the growth temperature of the multilayer. This indicates the AF-coupling strength is increasing with substrate temperature during deposition. However, the two samples with the similar multilayer growth temperature, but different buffer layer deposition temperature, have the same saturation field, but the magnitude of the GMR is reduced from 50% to 35%. It is evident that there are two different mechanisms for the reduction in the GMR emanating from the deposition temperatures of the different parts of the multilayer.

4.3.2. Magneto-Optical Kerr Effect.

The hysteresis curve at room temperature for sample 3 is shown in Figure 4.2 with the values of the remanent magnetisation for the other samples. The hysteresis loops for all of the samples were very similar with the same saturation field and remanent magnetisation.

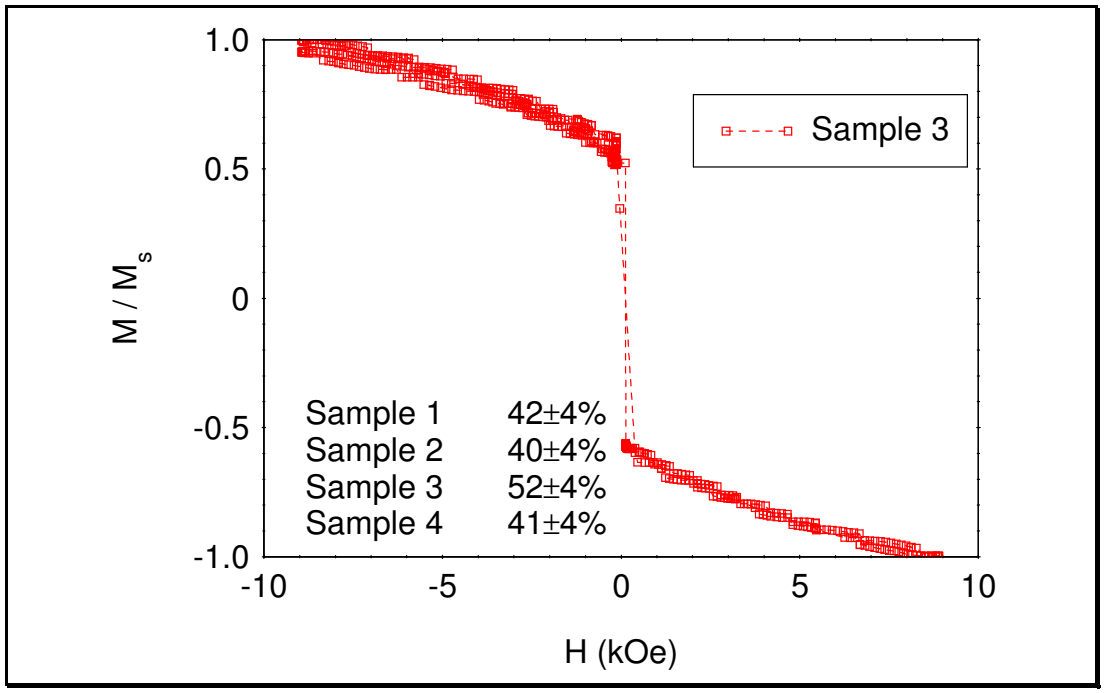

Figure 4.2: MOKE curve for sample 3, measured at room temperature. The other MOKE curves were very similar, and the values of the remanent magnetisation from these curves are given.

From these magnetic results there are large changes in the transport properties of the multilayers at 4.2K with changing growth conditions, but the anti-ferromagnetic coupling at room temperature remains unchanged. A comprehensive x-ray characterisation was carried out to determine whether there were changes in the structure or interface morphology, which could be related to the changes in the GMR.

4.4. X-ray Characterisation.

A full x-ray study was carried out on the samples to determine the structure and investigate if any changes in the structure could be related to the changes observed in the GMR. The experimental work was carried out on a laboratory diffractometer in Leeds, Station 2.3 at the Daresbury SRS and Beamline 16.3 at the ESRF, Grenoble. An outline of the equipment is given in chapter 2, along with a description of the types of scans and the information available.

4.4.1. Observations from the Reflectivity Scans.

The structural characterisation was carried out on the three samples with the same buffer deposition temperature to try and determine the effect of the deposition temperature of the multilayer. A quantitative picture of trends in some structural parameters can be drawn out by direct comparison of the experimental data for different samples. Figure 4.3 shows the specular scans taken at Station 2.3 Daresbury, offset for clarity.

The height of the Bragg peak in the reflectivity scan has been related to the roughness at the interface through the multilayer [82]. In Figure 4.3, the height of the Bragg peak is decreased with decreasing GMR. Therefore, the reduction in the height indicates that the GMR decreases as the interfaces in the multilayer become rougher. However, other layers can affect the height of the Bragg peak within the multilayer, particularly the

thickness of the cap. The cap thickness was expected to be the same in all samples, so the differences in the height of the Bragg peak should be due to the roughness within the multilayer. To confirm the caps were of equivalent thicknesses, and to quantify the trend in the roughness, simulations on the specular and diffuse scatter were performed.

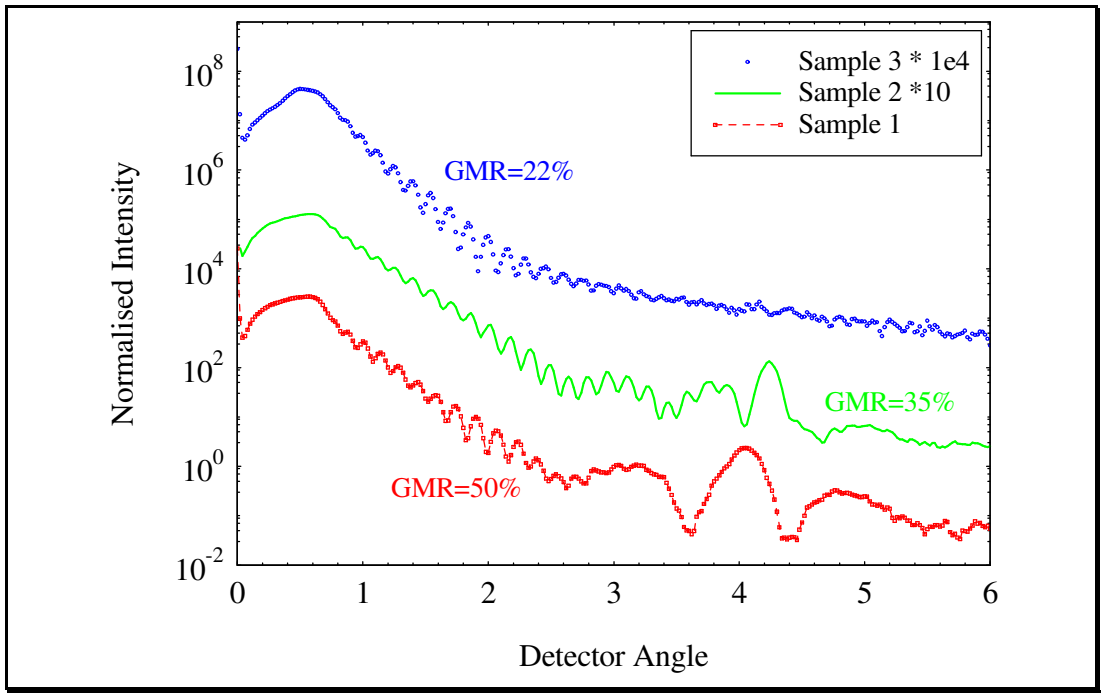

Figure 4.3: Specular scans for samples 1-3, indicating the reduction of the Bragg peak intensity with GMR.

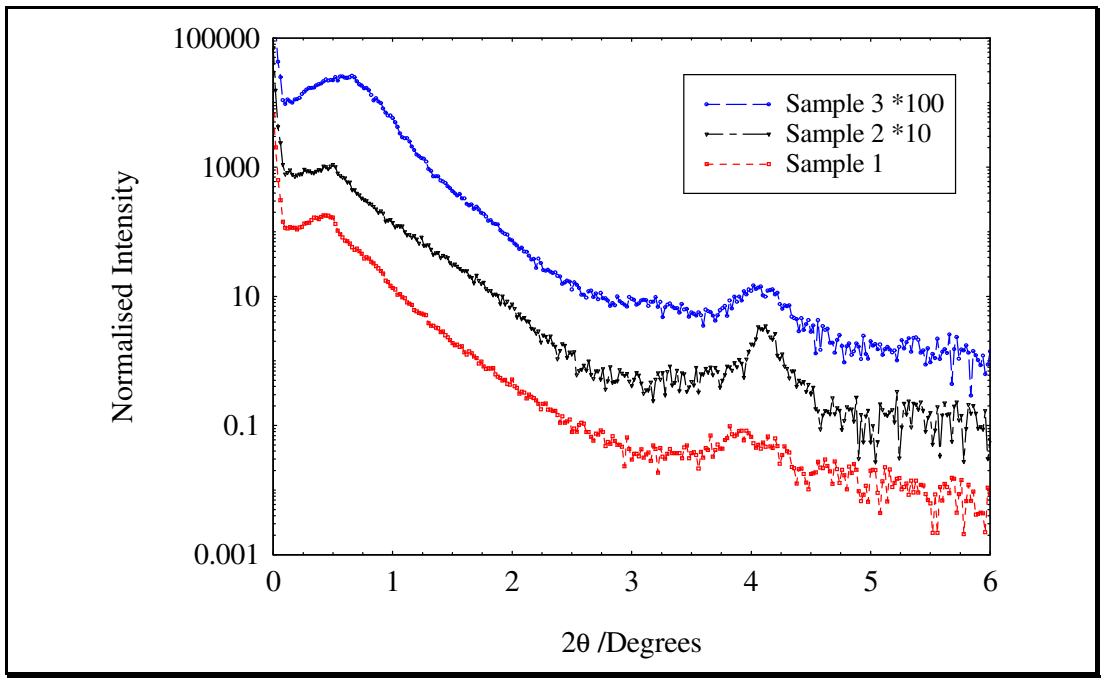

Figure 4.4: Off-specular scans of samples 1-3.

More information can be obtained by looking at the off-specular (or longitudinal diffuse) scans. The longitudinal diffuse scatter is the scatter away from the specular condition. Figure 4.4 shows the off-specular scans. A Bragg peak can be seen in these indicating that some of the scatter from the multilayer is being scattered slightly out of the Bragg condition. This is an indication that there is a large amount of correlated

roughness present throughout the multilayer. By the same argument, Kiessig fringes should be present if the correlated roughness extends from the substrate. However these fringes are not present, so the correlated roughness must originate from within the sample, and not extend from the substrate.

4.4.2. Observations from the High Angle Diffraction Scans.

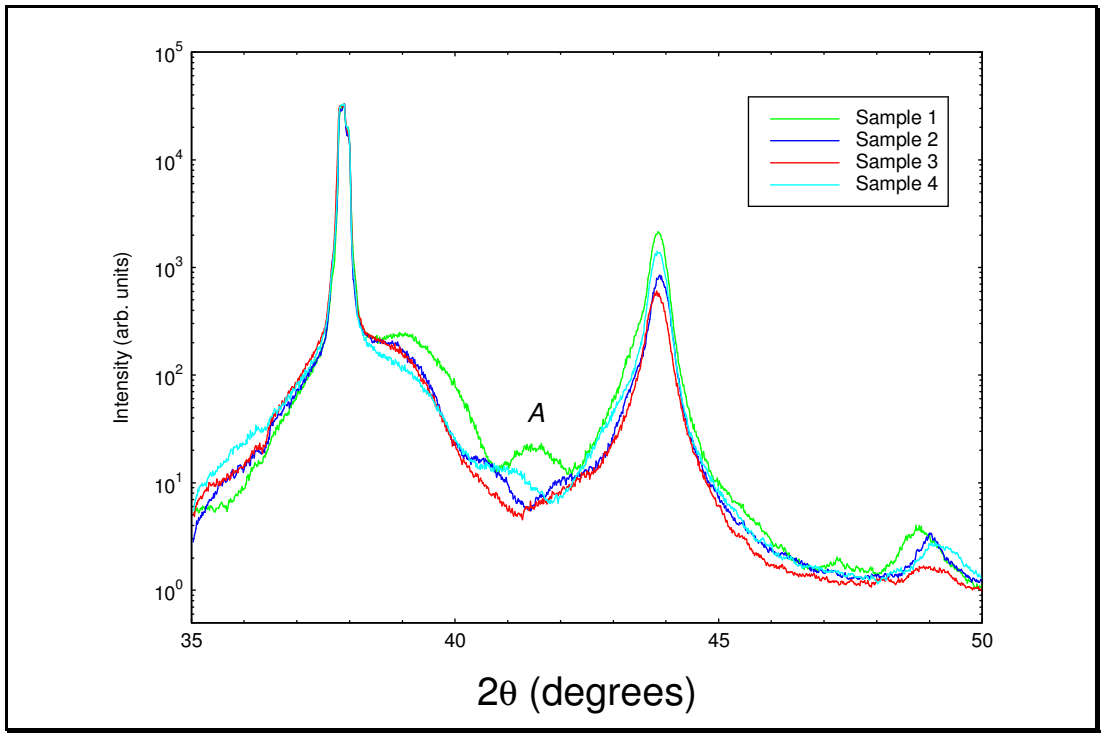

Figure 4.5: High angle diffraction curves, normalised to the substrate peak.

Initially the high-angle diffraction work was carried out on the Siemen's diffractometer in Leeds. A direct comparison of these scans, carried out by H. Laidler and J. Xu, is shown in Figure 4.5.

Differences in the experimental data between the substrate peak and the multilayer peak (marked as *A* on Figure 4.5) can be attributed to the formation of a CuAu alloy at the capping layer. In a previous study carried out by H. Laidler at Leeds, Co/Cu multilayers were annealed but x-ray reflectivity and diffraction were utilised along with the other magnetic and transport techniques [83]. The diffraction profiles showed the same differences between the substrate and multilayer peaks as above. High angle diffraction simulations indicated the formation of an alloy in the cap. The movement in the position of the Yoneda wings in the low angle transverse diffuse scans, caused by the changing electron density in the cap, confirmed this alloy cap.

High angle diffraction was carried out in triple axis configuration at the SRS, Daresbury and the ESRF, Grenoble to attempt to distinguish lateral tilts and mosaic structures within the sample. The tilt angle between the sample and the substrate was investigated by comparing two different $\theta/2\theta$ scans on the same sample, one with the counts maximised on the substrate and the second maximised on the multilayer peak. As can be seen in Figure 4.6, there is a big difference in the intensity of the multilayer peak between the two scans. This difference indicates that the multilayer is tilted with respect

to the substrate, due to a small miscut of the sapphire. This miscut has also been reported elsewhere [84].

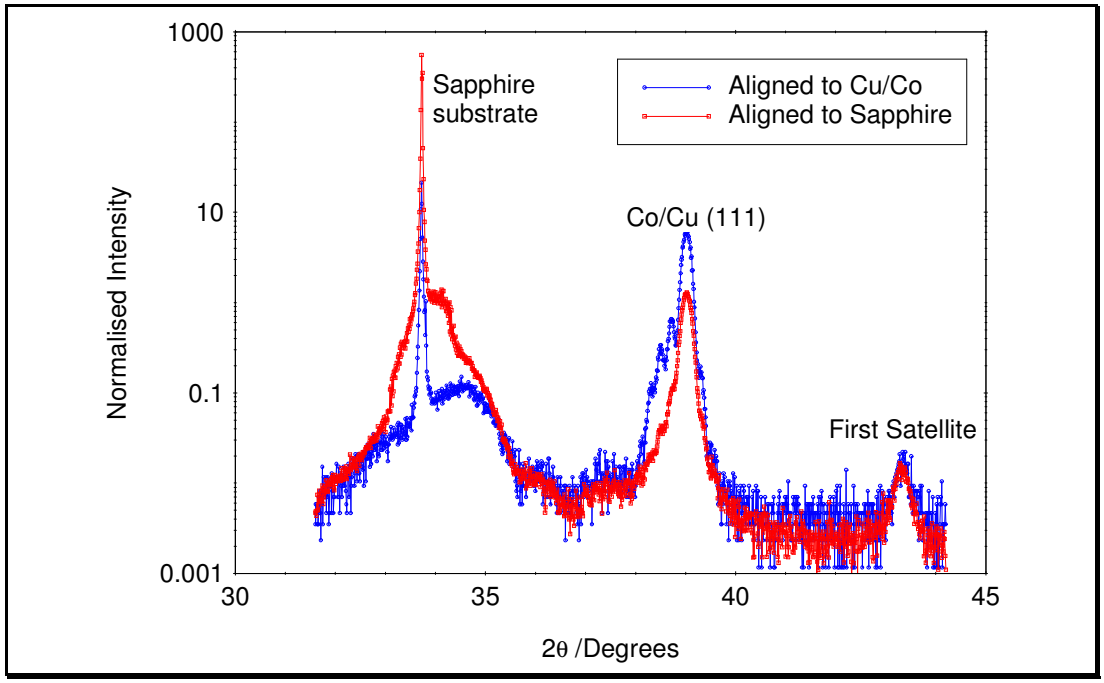

Figure 4.6: Sample 3 aligned on the substrate and the multilayer, indicating the tilt of the multilayer with respect to the substrate.

Quantitative trends have been observed by direct comparison of the experimental data. For a more qualitative comparison, the experimental data for the low angle reflectivity, transverse diffuse and the high angle diffraction were all simulated and the parameters obtained compared to each other, and their general trends compared to the trend in the GMR.

4.5. Simulations of X-ray Scans.

The specular and diffuse scatter at low and high angles was utilised to try to determine the structural and interface morphologies on the different samples. The work was carried out in collaboration with Professor B.K. Tanner's group at Durham University. The specular and transverse diffuse reflectivity was simulated using commercially available software from Bede Scientific [1]. High angle $\theta/2\theta$ scans were simulated by Helen Laidler and David Dekadjevi, using a modified version of the Suprex program [85]. Full details of the modifications to the simulation program and the simulations carried out can be found in Helen Laidler's thesis [70]. Other analysis of the x-ray data was carried out, including Born Analysis of the transverse diffuse at low angles and curve fits to the rocking curves through the multilayer peaks at high angle. Further details of this work are given later in this chapter.

4.5.1. Results from Specular Simulations.

Information about the thickness and roughness of individual layers can be elucidated from the simulations of the specular data. By using the simulation technique outlined in chapter 3, the data was simulated at two wavelengths, at and away from the absorption edge for Cu. These were carried out simultaneously, to obtain consistent parameters

between the two wavelengths. In this way, the parameters obtained were considered to be reliable, provided that they seemed physically viable.

Figure 4.7 shows the experimental data and simulations for sample 1. The strong features in the data make the simulations relatively straightforward. The height of the Bragg peak, indicating the amount of interface roughness, fits well between simulations indicating an accurate value from the simulation. The Bragg peak is broad in the experimental data, indicating fluctuations in the thickness of layers within the bilayer repeat. These slight fluctuations may be caused by the slight gradient induced from the wedged spacer layer, but are not taken into account in the simulations. After the Bragg peak there is another rise in intensity, which could not be fit using the parameters available. This problem has been encountered by others whilst simulating Co/Cu(111) multilayers [86], and is thought to be due to the structure of the bottom layers.

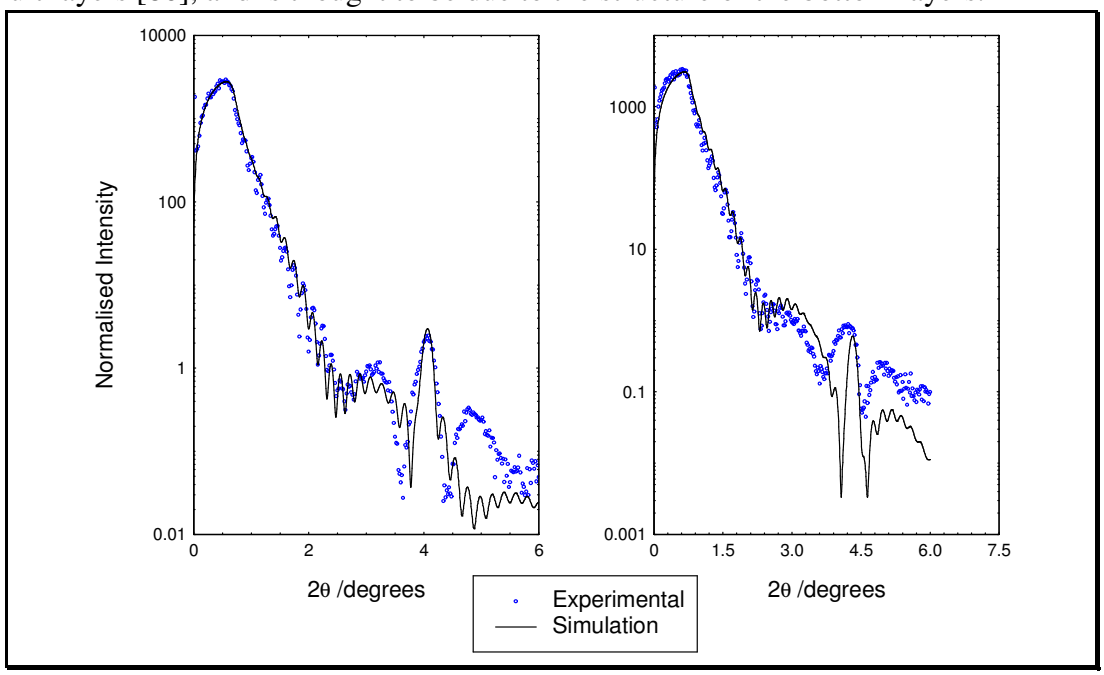

Figure 4.7: Specular simulations for sample 1, at (left) and away (right) from the Cu absorption edge.

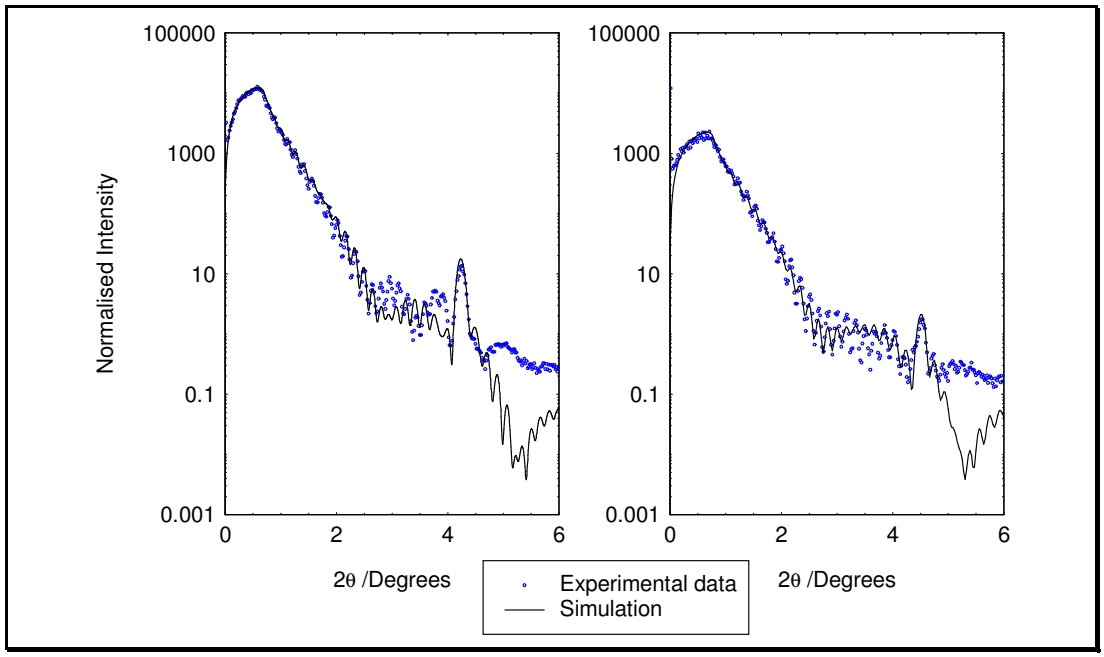

Figure 4.8: Specular simulations for sample 2, at (left) and away (right) from the Cu absorption edge.

The experimental data and simulations for sample 2 are shown in Figure 4.8. The simulation is reasonably good, giving consistent results between the two wavelengths. The height of the Bragg peak fits well in both simulations, indicating that the roughness obtained from the simulation is likely to be reliable.

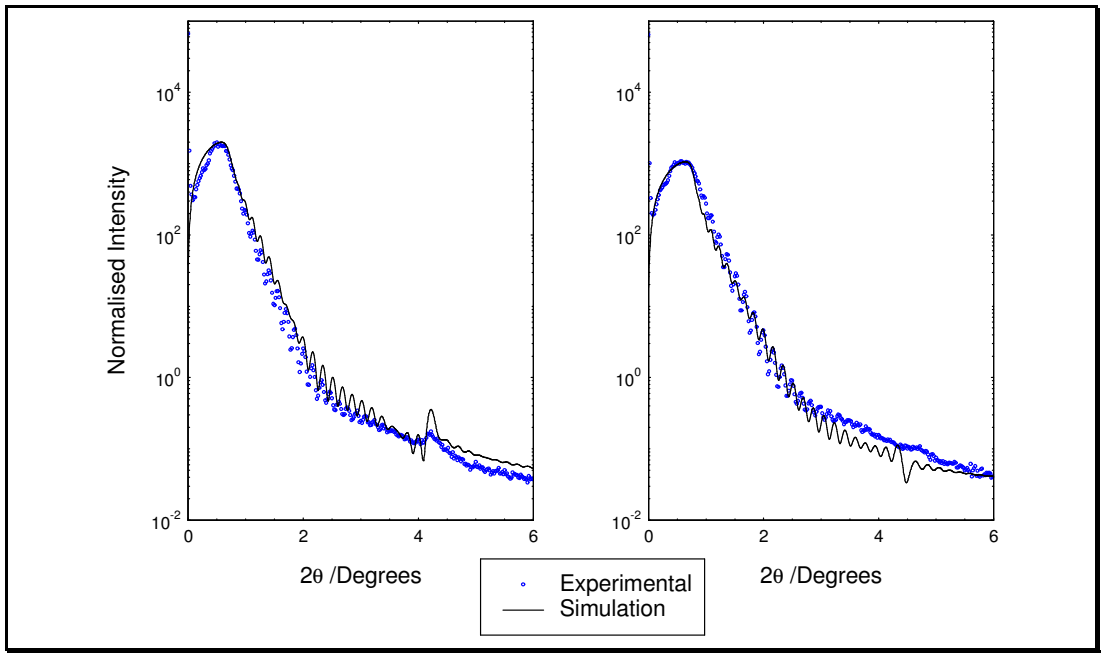

Figure 4.9: Specular simulations for sample 3, at (left) and away (right) from the Cu absorption edge.

Figure 4.9 shows the specular data and simulations for sample 3. The experimental data was very difficult to fit because of the lack of features within the data. The lack of a Bragg peak in the specular scatter indicates that the interface roughness is very large. It also makes fitting the bilayer thickness very difficult. An idea of the position could be obtained from the off-specular scatter, as the Bragg peak appears due to the large

amount of correlated roughness, but this peak is broad and low in intensity. The fall off and magnitude of the Kiessig fringes gave information about the top and bottom layers.

As was expected from the high angle diffraction data, an alloy of CuAu was necessary to be able to simulate successfully the experimental data. The composition of this alloy varied between samples. The thickness of this cap was consistently around 30Å, agreeing well with the expected value from the growth procedure. The roughness of the cap showed a general increase with decreasing GMR. This is not likely to be significant in itself except that, as a large amount of the roughness in the multilayer was correlated, this may be another indication that the roughness throughout the multilayer was increasing with decreasing GMR. Table 4.2 summarise the parameters obtained from the simulations of the reflectivity, along with the high angle parameters for comparison.

		LOW ANGLE					HIGH ANGLE					
		Bilayer		Cap			Cu		Co		Cap	
	GMR%	t /Å ±0.5	σ_{tot}/Å ±1	t /Å ±1	σ_{tot}/Å ±1	Alloy	t /Å ±0.4	σ_{CR}/Å ±0.01	t /Å ±0.4	σ_{CR} /Å ±0.01	t /Å ±1	Alloy
1	50	19.9	7	33	5	$Cu_{66}Au_{34}$	7.9	0.04	10.6	0.04	53	$Cu_{20}Au_{80}$
2	35	18.8	7	30	4	$Cu_{37}Au_{63}$	7.9	0.07	10.6	0.07	35	$Cu_{13}Au_{87}$
3	22	19.2	11	27	10	$Cu_{42}Au_{58}$	7.9	0.08	9.8	0.08	41	$Cu_{13}Au_{87}$

Table 4.2: A direct comparison of the parameters obtained from the low and high angle simulations, where t is the thickness and σ_{tot} is the total rms roughness at the interface.

The parameter σ_{cr} obtained from the high angle simulations is known as continuous roughness. This is a measure of the deviation of the lattice parameter from the mean value. This variation occurs at the interface, and is modelled by Gaussian variations in the lattice parameter. It is directly analogous to roughness in the reflectivity, but on an atomic scale.

The values from the reflectivity simulations obtained here also agree well with the parameters obtained from the high angle simulations by Helen Laidler and David Dekadjevi, considering the differences of length-scale the two techniques probe. However, there are some discrepancies in parameters. A major difference, present in all the samples, is the difference in the alloy composition. The low angle reflectivity is normally sensitive to this parameter, as the electron density of the alloy changes with composition, and hence the critical angle. The determination of the alloy from the high angle is more complicated. The position of the peak corresponding to the alloy gives an average lattice spacing within the cap. From Vegard's law, which states that the lattice spacing of an alloy is proportional to its composition, the percentage of gold in the cap can then be determined. However it has been shown experimentally [87] and theoretically [88] that the lattice constant of the system Cu_XAu_{1-X} show a positive deviation from Vegard's law leading to an over-estimation of the Au concentration. This is consistent with the observation here.

Other differences are confined to individual samples. The capping layer in sample 1 shows a large difference in the values obtained using the two techniques. However, the low angle value is consistent with the values obtained for the other capping layers in different samples. There is unlikely to be large differences in the thickness of this layer, as the expected thickness between samples was the same. The thickness in the high angle simulation is obtained from fitting a shoulder on the right hand side of the substrate peak. This fitting of the shoulder is difficult, and the height may be affected by other factors.

The results obtained from the specular simulations agree well with the trends picked out by the direct comparisons above. The total roughness at the interface of the Co/Cu is increasing with decreasing GMR, as expected from the quantitative conclusions obtained above.

Although values for the interface roughness have been extracted from the specular simulations, utilising the diffuse scatter more information about the type and length-scale of roughness was obtained. The values of the thichness and total roughness obtained in the specular simulations were used as fixed parameters in the transverse diffuse simulations.

4.5.2. Results from the Transverse Diffuse Simulations.

The transverse diffuse simulations were carried out for the wavelength λ=1.3803Å (the Cu absorption edge) at, and away from, the Bragg peak. The scatter at the Bragg peak position is predominately from the Cu/Co bilayers, whereas the scatter away from the Bragg peak is from the sample as a whole. The important parameters are the correlated and uncorrelated components of the roughness at the Co/Cu interfaces, and the length-scale of this roughness. An idea of this length-scale is usually the lateral correlation length, ξ, which is the statistical length over which the information about the height of two points reduces to $1/e$. The roughness exponent, *h*, is also extracted, giving a quantitative picture of how "smooth" or "jagged" the interface is.

Figure 4.10 shows the experimental data and the simulations for sample 1. The simulations use identical parameters, except for the correlation length. To obtain reasonable fits, it was necessary to use a long correlation length for the simulation away from the Bragg peak, but a short correlation length at the Bragg peak.

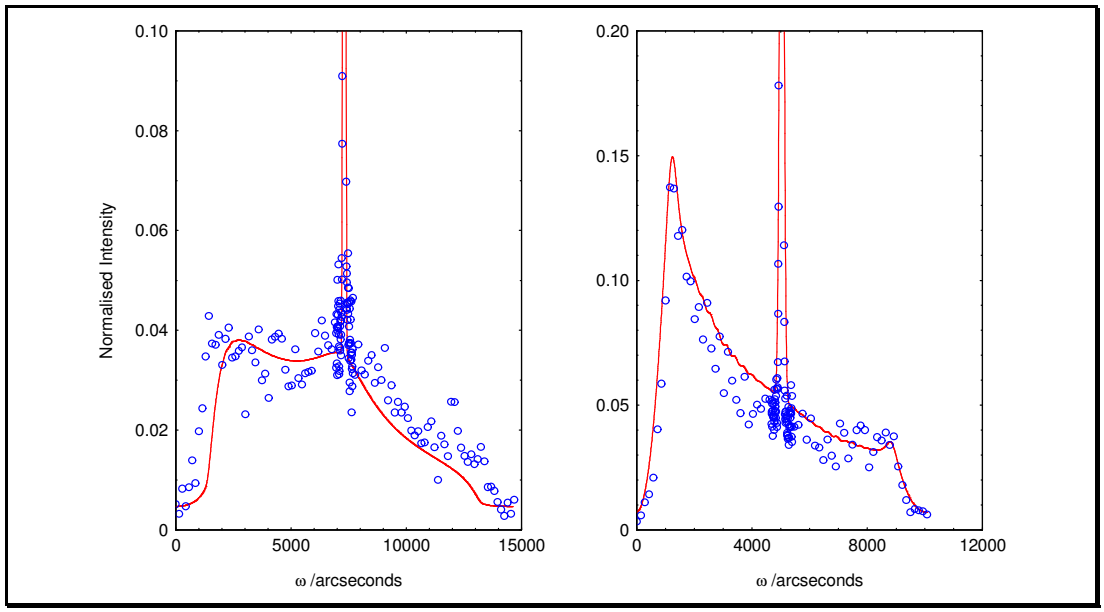

Figure 4.10: Transverse diffuse experimental and simulation for sample 1, at (left) and away (right) from the Bragg peak.

This phenomenon of more than one length-scale being present in the sample has been observed in many other systems, including other Co/Cu multilayer systems [89]. More analysis was necessary on this sample to confirm that two length-scales are indeed present, and this further work is outlined in Section 4.5.4.

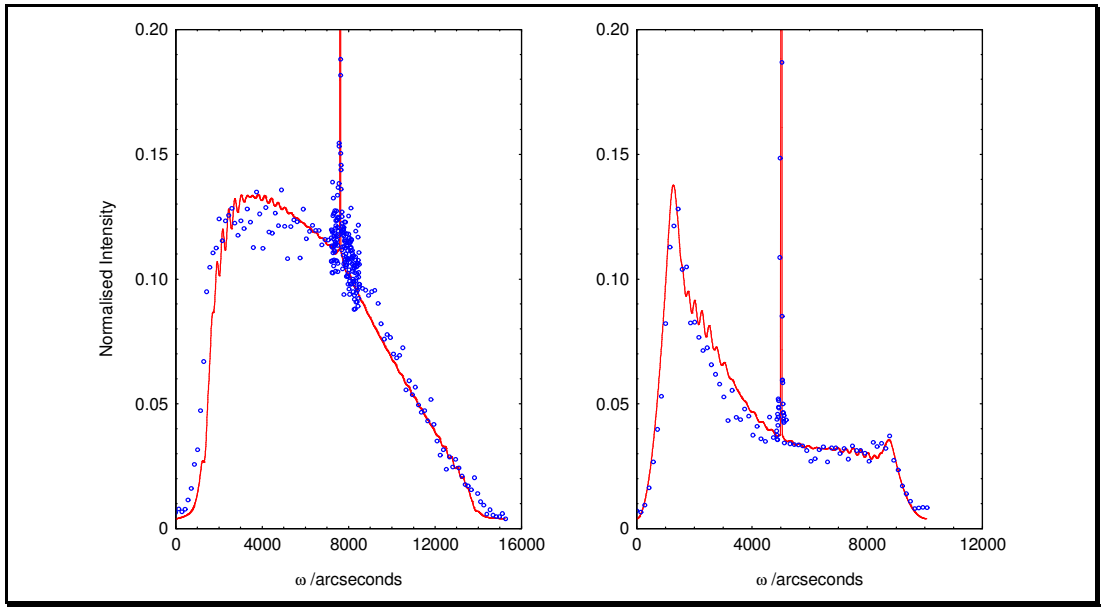

Figure 4.11: Transverse Diffuse for sample 2.

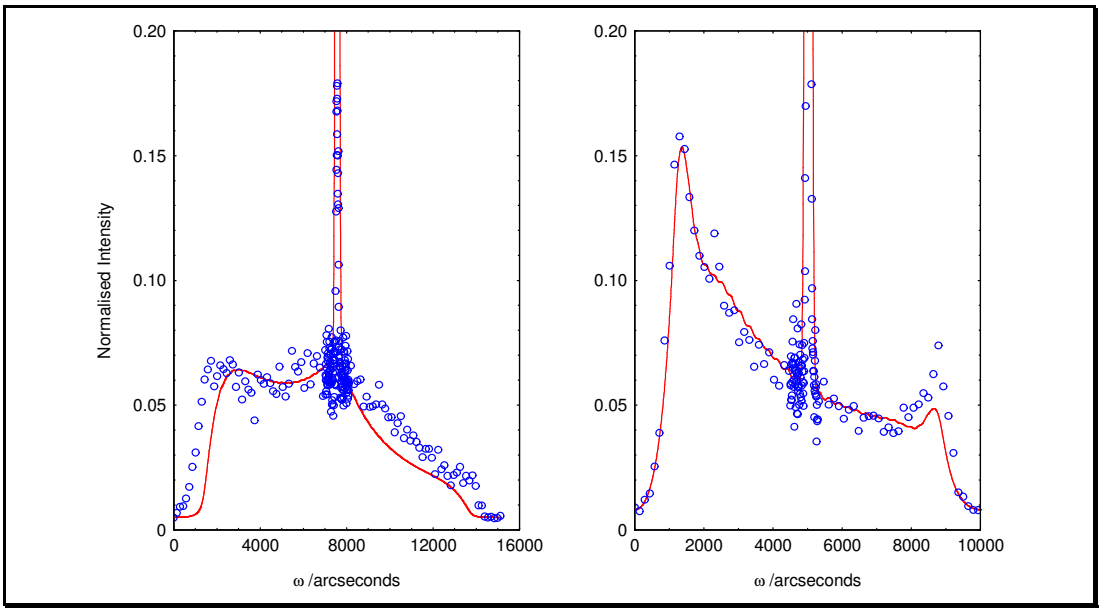

Figure 4.12: Transverse diffuse for sample 3.

Good fits are obtained using the same parameters for each simulation, within experimental uncertainties. Only one length-scale could be seen in these samples. However, if the long length scale is only present in a small fraction of the sample, it may not be seen in the simulations, as diffuse scatter from the other length-scale would dominate. This may be the case in samples 2 and 3 here. A summary of the important parameters deduced from these simulations is given in Table 4.3.

		Copper		Cobalt		Average	Average		
	GMR%	σ_c	σ_u	σ_c	σ_u	σ_c	σ_u	ξ±10 /Å	h±0.05
1	50	3	2	4	5	3.5	3.7	370 & 45	0.25
2	35	5	1	6	3	5.5	2.2	40	0.35
3	22	4	4	9	5	7.0	4.5	42	0.25

Table 4.3: Main parameters obtained from the transverse diffuse simulations.

The average value of the correlated or uncorrelated roughness between layers is calculated as $\overline{\sigma} = \sqrt{\frac{\left(\sigma_{Cu}^2+\sigma_{Co}^2\right)}{2}}$. As can be seen from Table 4.3, the correlated roughness follows the same trend as the total roughness above, but here the trend is much more conclusive. However, the uncorrelated roughness shows no such trend, so it appears that only the correlated roughness has an effect on the GMR of the sample.

Only one correlation length could be specified with the model used in the simulation software so, with the possibility of two length-scales being present, the validity of this function must be called into question. An alternative correlation function for the model, where the correlation length can be specified for each layer, could be used but has some disadvantages. This correlation length replaces the correlated roughness at the interface, with the result that the magnitude of the correlated roughness cannot be deduced. This is one of the main parameters required, so this is a severe limitation. The other major

disadvantage is a purely practical issue. The computation is lengthy with a single correlation length. The computation time scales as N^2, where N is the number of correlation lengths used. There are 43 layers present, consequently this alternative correlation function increases the computation time considerably, without gaining any extra information; although more information about different correlation lengths is obtained, information about the magnitude of the correlated roughness is not extracted.

Born Analysis was carried out on the diffuse scatter at the Bragg peak to confirm the trends in the correlated roughness.

4.5.3. Born Analysis of Correlated roughness.

A large part of this analysis was carried out by Tom Hase at Durham University, and a full description can be found in his PhD thesis [90]. The Born Analysis was developed by Savage *et al* [43] to utilise the diffuse scatter at the Bragg peak to determine a value of the correlated roughness within a multilayer, without the need for simulations. A brief outline of the method is given in chapter 2.

As can be seen in Figure 4.13, the trend in the correlated roughness replicates that found in the transverse diffuse simulations. However the values obtained for the correlated roughness from the Born Analysis are lower than those determined from the simulations of the transverse diffuse. The reason for this is due to an assumption made in the Born Analysis that the correlation length is infinite. This assumption is unphysical but is normally valid when the correlation length is long. In this case the correlation length is short, and this leads to an under-estimate of the correlated roughness component present.

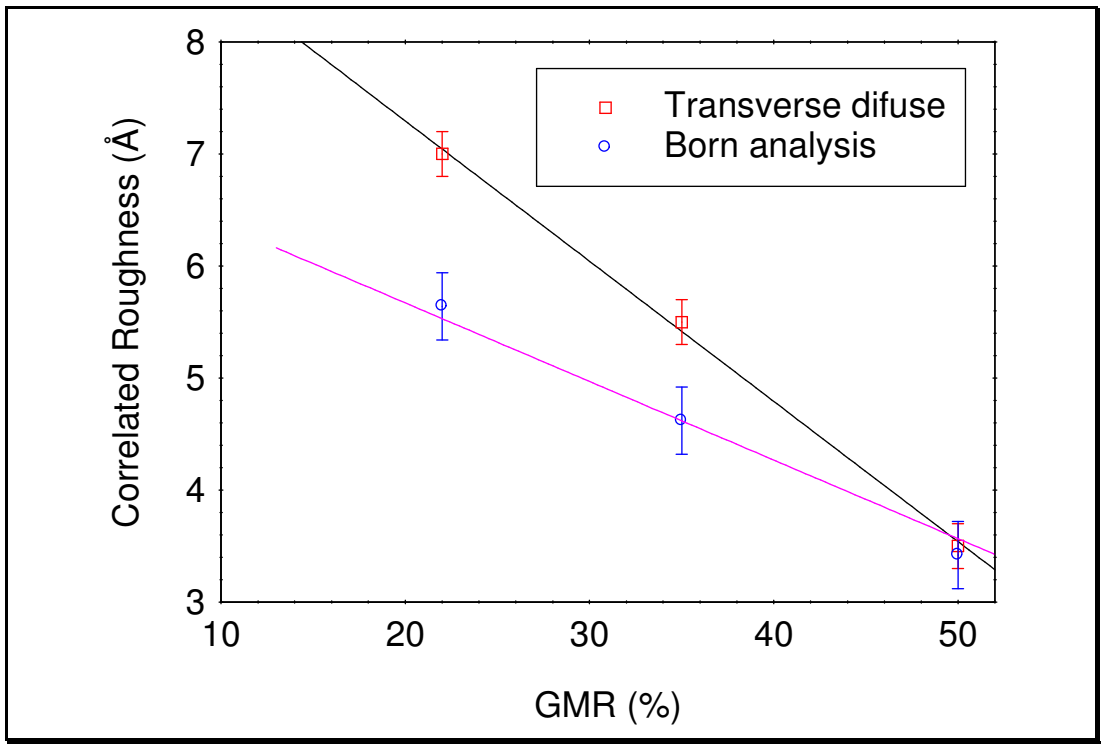

Figure 4.13: Correlated roughness v GMR from Born Analysis and the transverse diffuse simulations.

The Born Analysis away from the Bragg peak gave values of the uncorrelated roughness which indicated that there was no trend with the uncorrelated component of

the roughness and GMR. Therefore, the Born Analysis of the diffuse scatter confirms the trends in the correlated and uncorrelated roughness with the GMR deduced from the transverse diffuse simulations.

4.5.4. High Angle Transverse Diffuse Scatter.

Diffuse scatter was also utilised at high angle, to try to separate out roughness from the tilts and mosaic structure within the sample. By comparing the full width at half maximum height (FWHM) of the rocking curves through the multilayer satellite peaks at high angle, it was hoped to distinguish between roughness and mosaic structure present in the sample, and whether the degree of mosaicity correlated with the trends seen in the GMR.
The distinction between the roughness and mosaicity can be extracted by analysing the FWHMs as follows. The roughness should not affect the width of the zero order multilayer peak, and the width of the satellites should be parabolic as a function of satellite order and constant as a function of $\boldsymbol{q}_x$. If a mosaic structure is present however, the width of the zero order peak will be affected. Again the satellite widths will be parabolic about the zero order, but this time as a function of $\boldsymbol{q}_x$ and constant as a function of order. However, to determine this fully, several satellites either side of the main zero order peak are needed. Due to the similar scattering power of Co and Cu, only one satellite order is seen so it is not possible to determine whether the distribution is parabolic. Although this is not possible, it is still possible to determine whether the FWHM of the zero and first order peaks are changing in each sample, determining whether there is a mosaic structure present.

The fits to these curves have been carried out by T.P.A. Hase at Durham University. Initially a Lorentzian function was used to find the FWHM. This was to determine whether the samples exhibited a mosaic structure. There was no difference between the FWHM of the (111) zero order peak and the first order satellite, indicating a mosaic structure. The degree of mosaicity increased with decreasing GMR, confirming the preliminary results found by J. Xu. The angular width of the transverse scans through the zero order Bragg peak ranged from 1.2±0.1° for the low GMR samples to 0.7±0.05° for the high GMR samples. A similar mosaic width was observed for epitaxial Co/Cu(001) multilayers deposited on sapphire substrates by Di Nunzio *et al*. Here the mosaic spread was found to be 0.7° [91].

Recently, work has shown that lateral tilts in the sample can cause broadening of the rocking curve of the multilayer peak. Gibaud *et al* [84] studied the growth of Nb films on sapphire and found that there were two length-scales. The same correlation function is used in this analysis, and this predicts a Lorentzian-squared line-shape for the rocking curve. The inverse of the FWHM of the rocking curve is the lateral correlation length in the sample. Gibaud determined a correlation length for the Nb layer on sapphire of 76Å. Other systems have been investigated which also exhibit two length-scales. Similar work by Miceli *et al* [92] showed that length scales of a similar order were found for thin films of ErAs and $In_{0.7}Ga_{0.3}P$ on GaAs, using a similar correlation function.

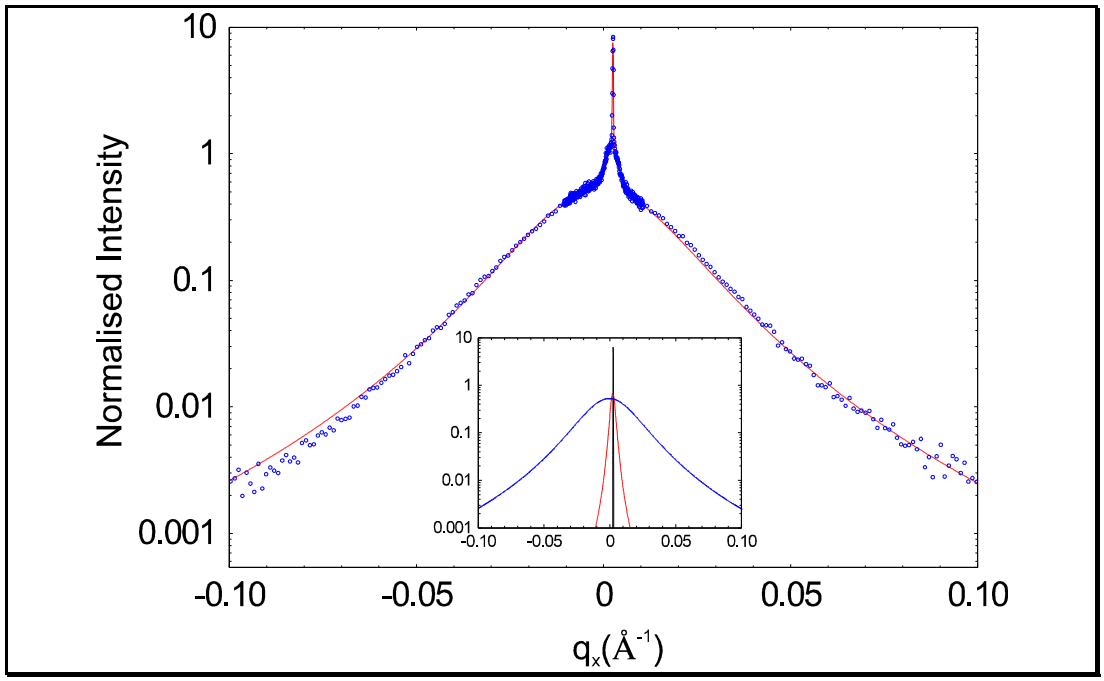

Figure 4.14: Rocking curve at high angles for sample 1.

On closer inspection of the rocking curve for sample 1, shown in Figure 4.14, three distinct peaks are evident. The sharp spike is not seen when an analyser crystal is used, and is thought to be due to the (113) sapphire reflection. Two other peaks can be seen in the data. The broad peak, which dominates the curve, indicates a short correlation length of approximately 35±3Å, but there is a longer correlation length of 370Å present. As the scan is taken through the Co/Cu multilayer peak, the broad peak is thought to be due to a short length-scale within the multilayer, and the long length-scale from the Cu buffer layer.

For sample 2, the same procedure indicated a long correlation length of 100Å present, along with a short correlation length of 25±2Å. For sample 3, a single Lorentzian-squared function is required to fit the data, indicating a single short correlation length of 17±3Å present in sample 3.

The values obtained from this method are consistent with those obtained in the transverse diffuse simulations at low angle, except for the long length-scale in sample 2 is not extracted from the low angle work. This second length-scale present in these data confirms the validity of using different correlation lengths in the transverse diffuse data for sample 1. The long correlation length in the transverse diffuse data was found away from the Bragg peak, indicating that it is not due to the multilayer itself, but to some other part of the sample. The position of the peaks in this analysis also seems to indicate that this is the case, and is most likely due to the buffer layer.

By comparing the integrated intensity of the deconvoluted peaks within each scan, an idea of the amount of a particular correlation length is present. By using this method, the longer correlation length (370Å) in sample 1 can be thought of as being present in 10% of the sample. This can be interpreted as the correlation length being present in the buffer layer, and then replicating into the first few layers of the multilayer, before being washed out and replaced by a correlation length of about 35Å. In the other samples, there is a very small component of a long correlation length present along with a short length-scale. The magnitude of this long correlation length decreases with increasing

multilayer growth temperature. For sample 2 it is approximately 100Å and makes up less than 4% of the sample. This may be the reason that it is not seen in the low angle scans. A single correlation length of 17Å is present in sample 3.

4.6. Discussion.

In this study, the substrate temperature during the deposition of multilayers has been varied to induce structural differences in Co/Cu(111) multilayers. As the substrate temperature increased, the GMR and $\Delta\rho$ decreased but with an increase in ρ_o. These changes indicated the change in structure, due to the increase in the substrate temperature during the deposition of the multilayer affected the magneto-transport properties. As the roughness increases, the decrease in $\Delta\rho$ implies a decrease in spin-dependent scattering of electrons but the total resistivity increases. This indicates that the scattering at the interface is larger for one spin channel, reducing the contrast in the resistivity between spin channels and hence reducing the GMR. A detailed structural characterisation was undertaken to investigate the changes in the structure and interface morphology.

Consistent structural parameters have been found for the series of samples with the utilisation of different x-ray scattering techniques. There are two main trends to observe. As the GMR increases, the amount of correlated roughness decreases and the magnitude of both the long and short correlation lengths increase. In all samples, there is a short correlation length, of order of 20-35Å, which dominates the scatter at the Bragg peak. There is also a long length-scale present in some of the samples, ranging between 100-370Å. These length-scales are consistent with recent work by others working on Co/Cu(111). Christedes *et al* [93] found a bimodal distribution of grain sizes above and below 120Å. Smith *et al* [94] determined a lateral correlation length of 36Å for the same system. Other correlation lengths include 17Å [86], 130Å [10] and grain sizes of 100-250Å [79,95] have been determined. The correlation lengths found within this study compare well with these length-scales.

The magnitude of the roughness has a significant effect on the GMR, but more importantly, the type of roughness seems to be important. In most other studies, only the total roughness from the height of the Bragg peak in x-ray reflectivity, or from scanning microscopy techniques, has been considered. Here, diffuse scatter has been utilised to separate the roughness into correlated and uncorrelated components. There seems to be no connection between the uncorrelated roughness and the GMR. However, the GMR seems to increase linearly with decreasing correlated roughness present at the Co/Cu interface.

These results may explain the discrepancies observed in early work into the effects of roughness on the GMR. As the roughness is often highly correlated this component dominates the total roughness, so the total roughness seems to be inversely proportional to the GMR. However, if there were a large component of uncorrelated roughness present, this component would dominate the total roughness and it may disguise any trends in the correlated roughness with GMR. Analysis of the type of roughness present may reveal the trends found here, that the correlated roughness is inversely proportional to the GMR.

The saturation field for the GMR at low temperatures increased with decreasing GMR. This may indicate that the strength of the AF coupling was stronger in samples with a low GMR. However, from the MOKE data taken at room temperature, the degree or strength of the AF-coupling does not appear to change significantly, unlike other reports of roughness affecting the GMR [54,96]. Clarke *et al* [97] has observed the same phenomenon of changes in the saturation field in the GMR but not in the MOKE hysteresis loops, and postulated the formation of a paramagnetic layer at the interface which influences the GMR. However, this paramagnetic layer should be evident in the MOKE hysteresis loop. No evidence for a paramagnetic layer was seen in the current results.

The temperature of the measurements may be more important. The GMR was carried out at 4.2K, whereas the MOKE was carried out at room temperature. This may explain the differences in coupling at low temperatures but not at room temperature, as the strength of the AF-coupling is known to be highly temperature dependent [98]. Persat and Dinia [99] have found a stronger temperature dependence of the exchange coupling strength in Co/Cu/Co trilayers than predicted by current theory. They attribute this to either a confinement of one spin orientation to the Cu layer, or to the magnetic nature of the interfaces. In the current study, the nature of the interfaces is changing between samples, and this may lead to variations in the temperature dependence of the coupling.

Another sample was grown, denoted sample 4 in the GMR and MOKE figures above, differing from sample 1 only in that the buffer was grown at a reduced temperature (250°C as compared with 375°C for sample 1). This was to investigate whether the temperature of the multilayer was the only important factor in the growth conditions. The GMR curve was of a similar shape, having the same saturation field, but the magnitude of the GMR was reduced from 50% to 31%. Similar characterisation studies were carried out on this sample to those outlined above. The specular simulations found that the interfaces were rougher than sample 1, indicating that a change in the deposition temperature buffer layer had a significant effect on the transport properties of the multilayer. The transverse diffuse reflectivity was very difficult to fit, maybe due to the different length-scales being present, and good quality fits were not possible. However, the high-angle rocking curves revealed correlation lengths of the order of 30Å and a small component of 100Å. The longer correlation length made up approximately 1% of the sample, so an accurate value could not be determined. However, it is substantially lower than that found in sample 1. Therefore, it can be deduced that the temperature of the deposition of the buffer layer is vital in determining both the quality of the buffer layer and of the subsequent layers.

The short correlation length may be due to Co islands formed during growth. There have been differing conclusions of the growth mode of Co on Cu(111). Gonzalez *et al* [100] reported that the Co grows in Co islands for the first monolayer, and then the growth is layer by layer. Island growth has been observed by others [101,102,103,104] and is predicted to be thermodynamically stable [105]. The extent of this island growth may also determine the magnitude of the roughness at the interface.

These results indicate the importance of the substrate temperature in multilayer growth. The long correlation length, thought to be due to the Cu buffer, has a profound effect on the structure of the whole multilayer. This, in turn, affects the magneto-transport properties of the multilayer. This length-scale appears to be controlled by both the deposition temperature of the buffer itself, and that of the subsequent layers. The growth

temperature of the subsequent layers may be important, as this is the temperature to which the buffer is cooled after deposition. This may affect the morphology of the surface of the buffer onto which the multilayer is deposited.

A less detailed study was carried out on other parts of the same wedges, particularly those with a thicker spacer than the main study. Only the Born Analysis and the rocking curves at high angle were carried out, by T.P.A. Hase at Durham University [90]. He found the same trends as the above study, giving further weight to the evidence that the growth temperature has an important effect on the transport characteristics of magnetic multilayers.

4.7. Summary.

A series of multilayers with different growth condition have been grown in this study. The GMR of the samples was inversely proportional to the correlated roughness at the interface of the Co/Cu in the multilayer. The scattering from the interfaces was larger for one of the spin channels, reducing the contrast in resistivity between spins. This led to a decrease in $\Delta\rho$ and hence in the GMR. In each sample there are two length-scales present, the longer scale attributed to the Cu buffer layer and the shorter length-scale to the Co/Cu layers, possibly due to the size of Co island clusters during the growth. The magnitude of these length-scales increases with increasing GMR. The magnitudes of the roughness and correlation lengths found are consistent with previous studies on this system, and reinforce the belief that smoother interfaces produce a larger GMR. The quality of the multilayer is highly dependent on the quality of the buffer layer on which it is grown. To obtain high GMR values, the structure of the buffer is crucial, and should be of low roughness and long correlation length.

Chapter 5: Electron Channelling in Fe/Au Multilayers.

5.1. Introduction.

In recent years, the structural and magnetic properties of thin films of Fe, both single layers and Fe incorporated in multilayers, have been extensively studied but the electron transport properties have normally been neglected. This seems to have arisen from the perception that either very thick Au buffer layers or single crystal Au or Fe wafers are required to obtain the good structure necessary for the GMR to be observed. These thick buffers cause a low resistance shunt for the current, which can mask any GMR effects occurring within the multilayer. Shintaku *et al* [106] have observed a maximum GMR of 2.3% in Fe/Au(100) multilayers at low temperatures, with an Au buffer thickness of 470Å. This is large considering the buffer thickness, but no other studies of the GMR have been reported.

In this chapter, the electron transport and structural characterisation of Fe/Au multilayers of two different orientations is discussed. In chapter 3 the concept of electron channelling was introduced, where an electron spin-channel can be confined to the spacer layer when the magnetisations of the magnetic layers are parallel. The spin asymmetry in the reflection coefficients is important, so that only one spin channel is confined to the spacer in the parallel state, and there is no confinement for either spin in the anti-parallel alignment. As the conductivity of Au is greater than that of Fe, this confinement should give rise to a large GMR in the (100) orientation. The asymmetry for the (111) case is less so the GMR should be less. According to the calculations carried out [60,61], the (100) system should exhibit oscillatory exchange coupling with two periods of 8.6-10.3 and 2.49-2.51 monolayers. The magnitude of the GMR should be large with oscillations as a function of Au thickness, and the saturated conductivity should be much higher than expected. The differences in the transport properties between the orientations is investigated, and discussed in terms of the spin reflection coefficients.

For such a study to be viable, the multilayers were grown on 60Å Au buffer layers. This was thinner than is generally used for these systems, but would reduce the shunting effect of the thick buffer layers typically used by others. Hayashi *et al* [107] studied the MOKE response of Fe(100) layers, and the samples were deposited on a MgO(100) substrate, but with a 2000Å Ag seed and 2000Å Au buffer layer. Nakayama *et al* [108] carried out an x-ray diffraction study on Fe/Au(100) multilayers on samples grown on GaAs(100) with a 1000Å Au buffer. Okuyama [109] investigated the crystallographic and magnetic properties of Fe/Au(100) and (111) multilayers deposited on GaAs(100) and sapphire(111) substrates respectively. The Au buffer thickness was 1000Å in both cases.

As the buffer layers utilised in this study are much thinner than elsewhere increased interface roughness was expected. However, in preliminary experiments, an Au buffer layer of 60Å proved adequate to observe a GMR.

5.2. MBE Growth of Fe/Au Multilayers.

The multilayers were grown in the VG-80 MBE machine at the University of Leeds. Some of the Fe/Au(111) multilayers were grown by J. Xu and M.J. Walker.

5.2.2. (100) Orientation.

The magnetic properties of the Fe/Au(100) system have been extensively studied because of the excellent growth. This growth is due to the Au(110) spacing being close to the Fe(100) lattice parameter

$$\left[d(200)_{Fe} - d(220)_{Au}\right] \Big/ d(220)_{Au} = -0.6\% \quad \text{..... (5.1)}$$

so good growth is obtained by a rotation of the Au lattice by 45° in the interface plane. The Fe has been observed [110,111] to grow layer by layer on Au(100), with Fe(100)[100]//Au(100)[110]. Some groups have reported a thin layer of Au floating on the surface of the Fe during growth [112,113], which they postulate lowers the surface energy and prevents island growth of the Fe. This surfactant growth has been suggested in other systems. Egelhoff *et al* [114] have used Pb as a surfactant in Co/Cu spin valves to smooth the interfaces, thus reducing the ferromagnetic coupling across the Cu spacer layer.

The Fe/Au(100) multilayers were grown on polished MgO(100) substrates. The substrate was first cleaned in a solution of 5% HNO_3 in C_2H_5OH, with ultrasonic cleaning for 1 minute. It was then placed in pure C_2H_5OH, again with ultrasonic cleaning, for another minute. This was repeated twice, and then finally washed in CH_3OCH_3 with ultrasound for one minute. The substrate was mounted onto the molybdenum block using screws in a nitrogen atmosphere and placed into the MBE machine, heated to 950°C and left for 1 hour to complete the cleaning procedure. A 10Å Fe seed and then a 60Å Au buffer layers were deposited at 500°C and 200°C respectively. The multilayer was then deposited at 70°C, with a constant Fe thickness of 10Å and the Au spacer layer as a natual wedge. The multilayer consisted of 20 repeats in all samples. All of the deposition rates were 0.2Å/s. RHEED images of the top surface show sharp streaks, indicating good flat layers.

5.2.3. (111) Orientation.

Fe has been reported to grow in the (110) orientation on Au(111) [115] and Ag(111) [116], but in a growth study at the University of Leeds, J. Xu postulated the growth of fcc Fe on Au(111) for the first three monolayers, with a transition to bcc growth after this thickness [117]. This has also been reported elsewhere on Au(111) [118], and also for the growth of Fe on Cu(111) [119]. This is being investigated in more detail using RHEED, x-ray diffraction and grazing incidence diffraction by D. Dekadjevi in Leeds, and B.D. Fulthorpe at Durham University.

The (111) multilayers were grown on sapphire $(11\bar{2}0)$. J. Xu developed the growth procedure after a study utilising RHEED and x-ray diffraction to analyse the structure of the resulting multilayers. The sapphire was cleaned by washing in CH_3OCH_3 and then C_2H_5OH, and mounted on the molybdenum block using screws. The substrate was heated to 900°C and a 20Å Nb seed was deposited. The growth procedure from this point was the same as the (100) orientation, ie the 60Å Au buffer was deposited at 200°C and the multilayer at 70°C. RHEED was again used at points within the growth

to study the structure of the surface. The top surface was a 5x1 reconstruction, indicating a good Au (111) orientation.

X-ray reflectivity and diffraction was performed using the Siemens diffractometer in the University of Leeds, to check the epitaxy and the thickness of layers within the multilayer. A description of this diffractometer is given in chapter 2.

5.3. X-Ray Characterisation using a Siemens Diffractometer.

Standard x-ray characterisation was performed to confirm the thickness of the layers within the multilayer and that the texture was as required.

5.3.1. X-Ray Reflectivity.

In the low angle regime, information about the bilayer period can be readily obtained. In turn, this gives the thickness of the spacer layer in each sample. A typical reflectivity scan of each orientation is shown in Figure 5.1.

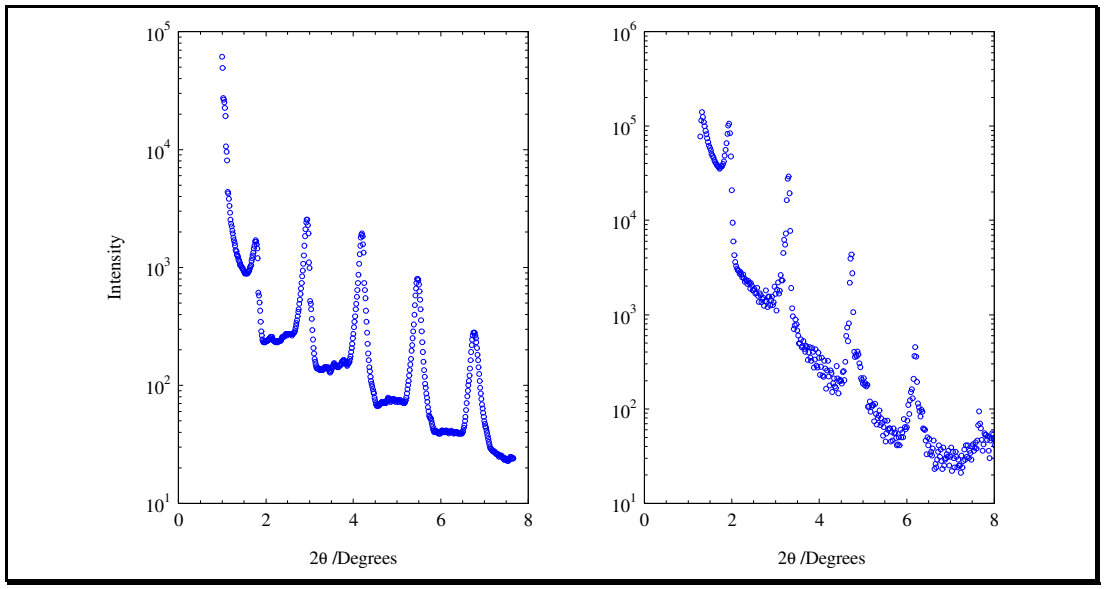

Figure 5.1: X-ray reflectivity of each orientation, on the left the (100) and the right the (111).

The pronounced Bragg peaks in each orientation indicate a well-defined bilayer period, with sharp interfaces. The Au spacer thickness can be deduced, as the Fe thickness is constant throughout the wedge.

5.3.2. X-Ray Diffraction.

Figure 5.2 shows typical x-ray diffraction scans for the two orientations taken at Leeds.

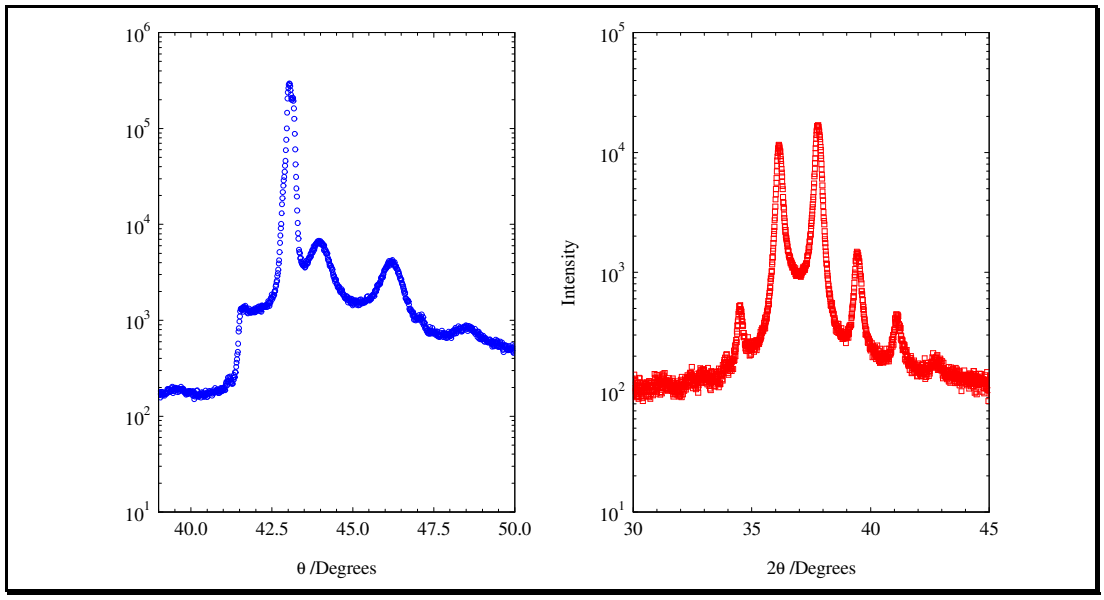

Figure 5.2: High-angle diffraction scans for the two orientations, (100) left and (111) right.

The position of the main multilayer peak was calculated using the weighted average of the Fe and Au lattice parameters. The weighting factor was simply the relative thicknesses of the Fe and Au layers. The strong multilayer peaks in each case correspond to the correct orientations, with no other orientations visible, indicating good epitaxial quality. This was investigated further with the use of synchrotron radiation, where the high intensity and resolution could enable diffuse scatter to be utilised.

The Au thickness obtained from the satellite reflections was in good agreement with the reflectivity. With the quality and thickness of the layers having been confirmed, the electron transport and magnetic properties were studied.

5.4. Comparison of the GMR.

The GMR was measured at 4.2K in a Thor cryostat, with typical GMR hysteresis loops shown in Figure 5.3. Details of the cryostat and measurement technique can be found in chapter 3. Some of these measurements on the (111) samples with thin spacer layers were carried out by J. Xu.

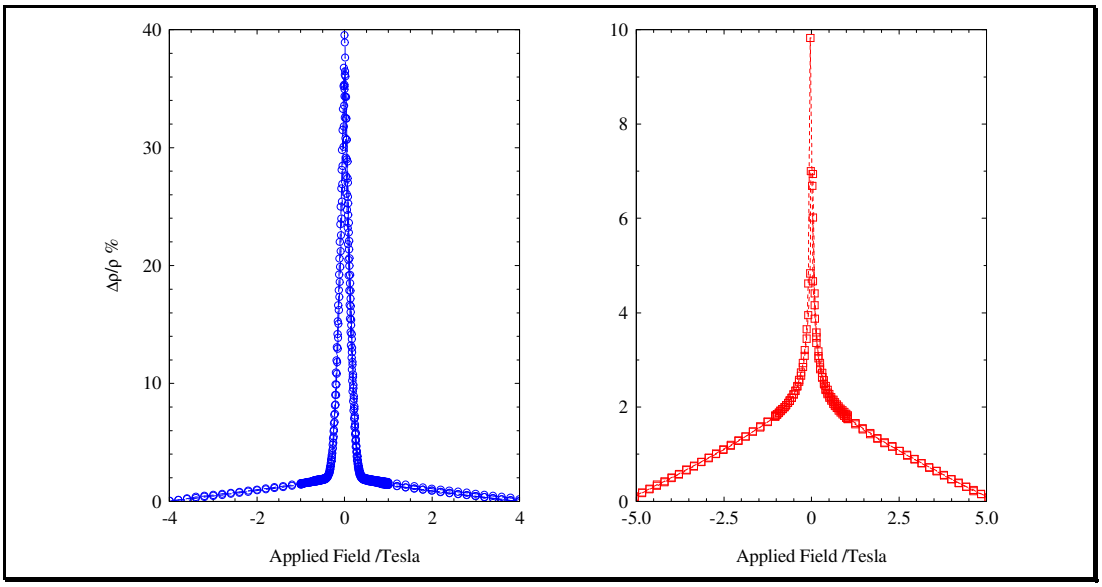

Figure 5.3: GMR hysteresis loops for the (100) (left) and (111) (right) orientations.

The magnitude of the GMR in the (100) sample shown is 40%, compared to the 2.3% for the equivalent sample obtained by Shintaku *et al* [120] with 470Å Au buffers. This indicates the thin Au buffer and the growth procedures utilised were adequate to produce large GMRs. It also emphasises the masking effect a thick Au buffer can have on the transport properties of the multilayer.

The different shapes of the GMR curves in Figure 5.3 are due to a decrease in the resistivity of the multilayers, even after the parallel alignment of the magnetic layers. This tendency was a characteristic of all the GMR curves of both orientations. This has been observed by Honda *et al* [121] for an Fe thickness of $d_{Fe} \leq 9$ Å in Fe/Au multilayers deposited on glass slides, and ascribed it to discontinuous Fe layers. This produced super-paramagnetic behaviour evidenced by the lack of saturation of the GMR and MOKE curves. In our work, the magnitude of this superparamagnetic behaviour is small in comparison to the GMR from the ferrromagnetic alignment of the magnetic layers.

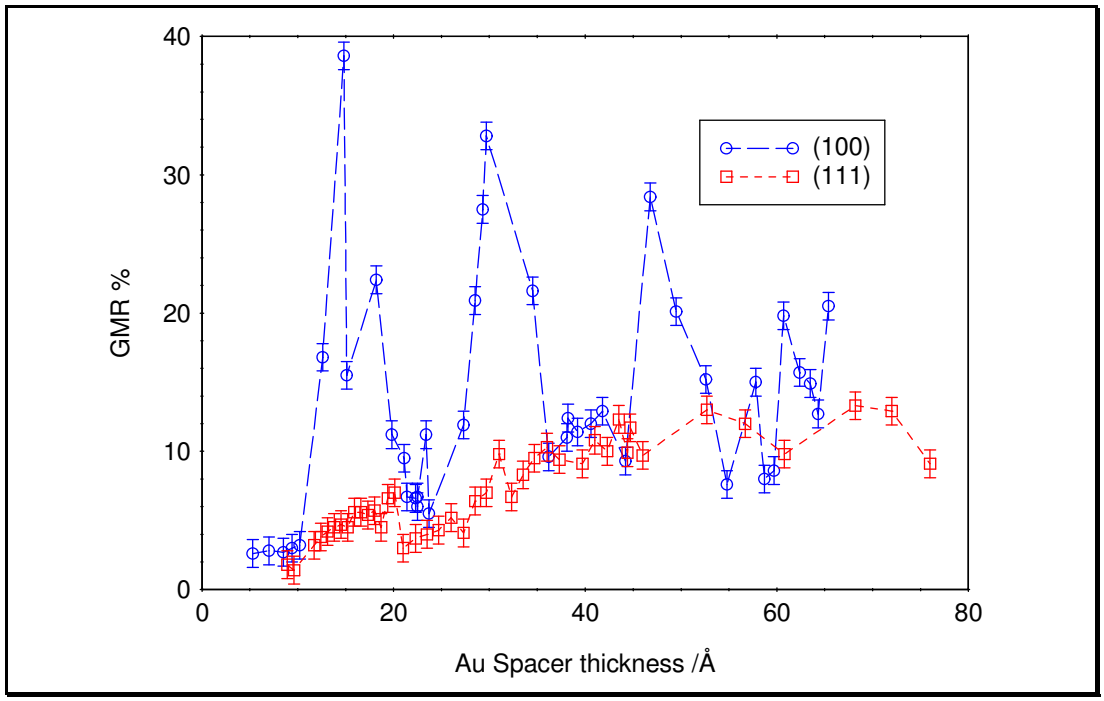

Figure 5.4: GMR as a function of spacer thickness.

The GMR as a function of spacer thickness is shown in Figure 5.4. The (100) orientation exhibits oscillations in the GMR as a function of the spacer thickness. Three clear peaks are shown, and there are indications that a fourth peak is also present. The (111) shows no such oscillations, but just a gradual increase in the GMR with spacer thickness. Shintaku *et al* [106] also observed oscillations in the GMR in the (100) orientation. They studied a Fe/Au system grown on a glass substrate, which was predominately (111) but with a small amount of (100) present, and found no such oscillations. This is again in agreement with the current results.

To confirm these oscillations in the (100) multilayers were due to oscillations in the AF-coupling, MOKE hysteresis loops were obtained.

5.5. MOKE Hysteresis Curves.

The MOKE hysteresis loops were taken to show the nature of the AF-coupling as a function of the spacer thickness. The thin layers of Fe present a problem in the MOKE characterisation, as the Kerr rotation is very small for thin Fe layers [122]. In addition to this, there is a reduction in the signal due to the angle of incidence not being at the optimum angle (see chapter 3). To try to overcome these problems, the data was averaged over 20 loops to improve the statistics. Full details of this are given in the thesis of H. Laidler, who developed the procedure [70]. Typical hysteresis loops are show in Figure 5.5, and Figure 5.6 shows the remanence as a function of thickness for both orientations.

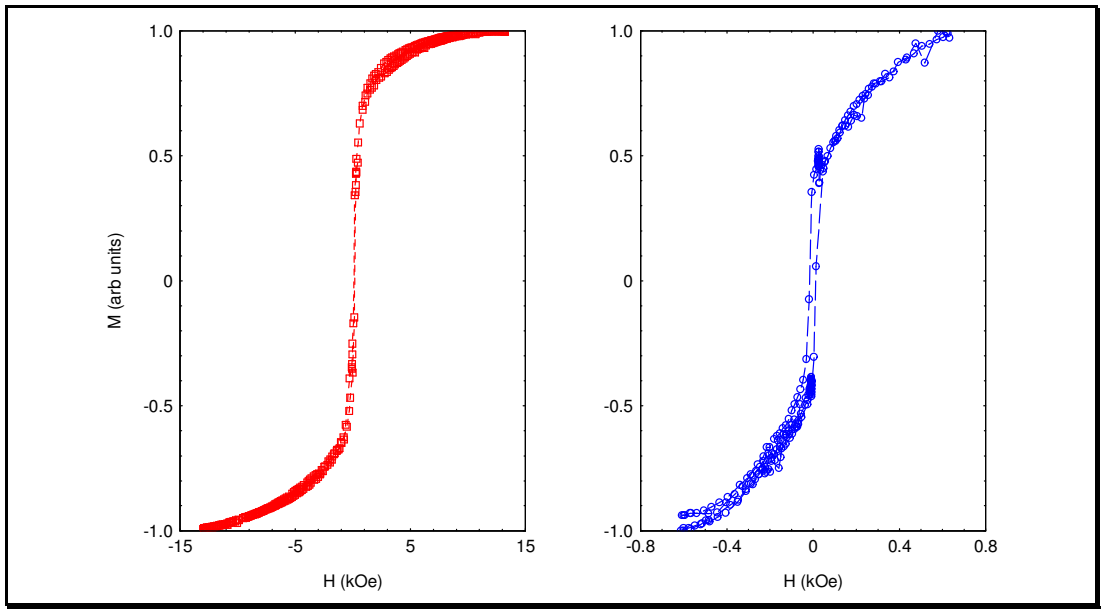

Figure 5.5: Typical MOKE hysteresis loops for the (100) (left) and (111) (right) orientations.

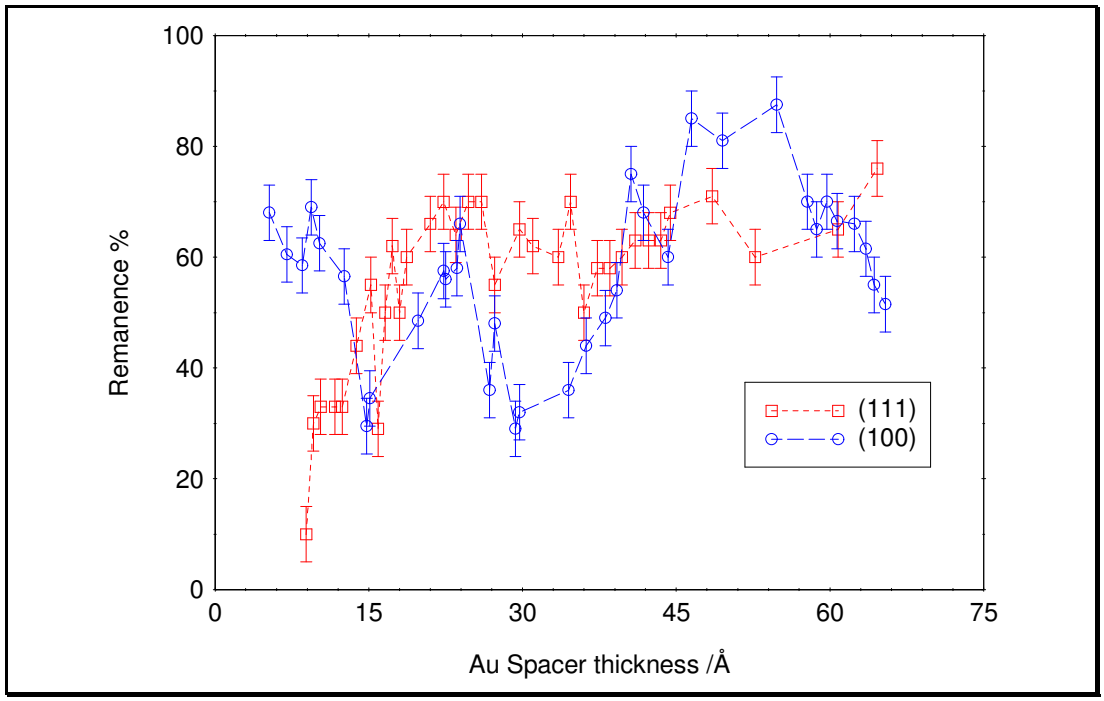

Figure 5.6: Remanence as a function of spacer thickness for each orientation.

The (100) clearly shows oscillations, but even at a maximum in the AF-coupling (a minimum in the remanence), the samples are only 70% coupled. There does not appear to be complete AF-coupling present at any point. The minima in the remanence occur at the same thickness as the maxima in the GMR.

The (111) samples with thin spacer layers have a large degree of AF-coupling, but this is not replicated by a maximum in the GMR. This was also observed in the work by Shintaku *et al* [106]. The reason is unclear, but may be due to the quality of the very

thin films of Au(111) within the multilayer. There does not appear to be oscillations present, again correlating with the results found in the GMR.

To confirm the GMR was enhanced due to the orientation of the sample, multilayers with equal volume fractions of AF-coupled material were compared. One sample from each orientation was chosen with a spacer thickness of 15Å and a 30% remanence. The GMR of the (100) sample was 38% as compared to 6% for the (111) multilayer, indicating a large enhancement due to the orientation of the sample.

These oscillations in the AF-coupling are predicted by electron channelling theory, with the spanning vectors across the Fermi surface corresponding to particular periods. There is a predicted oscillation in the (111) of 4.83 ML [60], but this is very weak and has not yet been observed. As there are two periods predicted for the (100) samples, the GMR data was analysed to extract these periods.

5.6. Modelling of the GMR Oscillations.

In recent years, there have been two main predictions of the oscillation periods in the Fe/Au system. Bruno and Chappert [60] predict two periods, a long period of 8.6 monolayers (ML) and a short period of 2.52 ML (17.5Å and 5.1Å assuming bulk lattice parameters). Stiles [61] predicts 10.3 ML and 2.48 ML (21.2Å and 5.1Å). Two periods have been observed experimentally, using a variety of magnetisation measurement techniques. Unguris *et al* have determined periods of 8.6 and 2.48 ML using SEMPA [58]. Other experimental work has determined periods of 8.0 and 2.0 ML using SMOKE [123], and very recently 8.7 and 2.5 ML using magnetic circular dichroism (MCD) [124]. In this work, in addition to the two periods, a third period of 13.8 ML was observed. The period found from the work on the GMR of Shintaku *et al* [120] was difficult to define, as the peak to peak interval increased with increasing Au thickness (12Å, 14Å and 20Å). This is the only published work on the oscillations of the GMR in Fe/Au(100) multilayers.

In this work, the oscillations in the GMR were modelled with a function used by Unguris *et al* [125] which is simply the sum of two sine waves, with an exponential damping factor:

$$GMR = \exp\left(\frac{-t}{\lambda}\right)\left[A_1 \sin\left(\frac{2\pi t}{d_1} + \phi_1\right) + A_2 \sin\left(\frac{2\pi t}{d_2} + \phi_2\right)\right] \quad \text{..... (5.2)}$$

where t is the Au spacer thickness, λ, d, A and ϕ are adjustable mean-free path, periods, amplitudes and phases respectively. The best fit to the experimental data is shown in Figure 5.7.

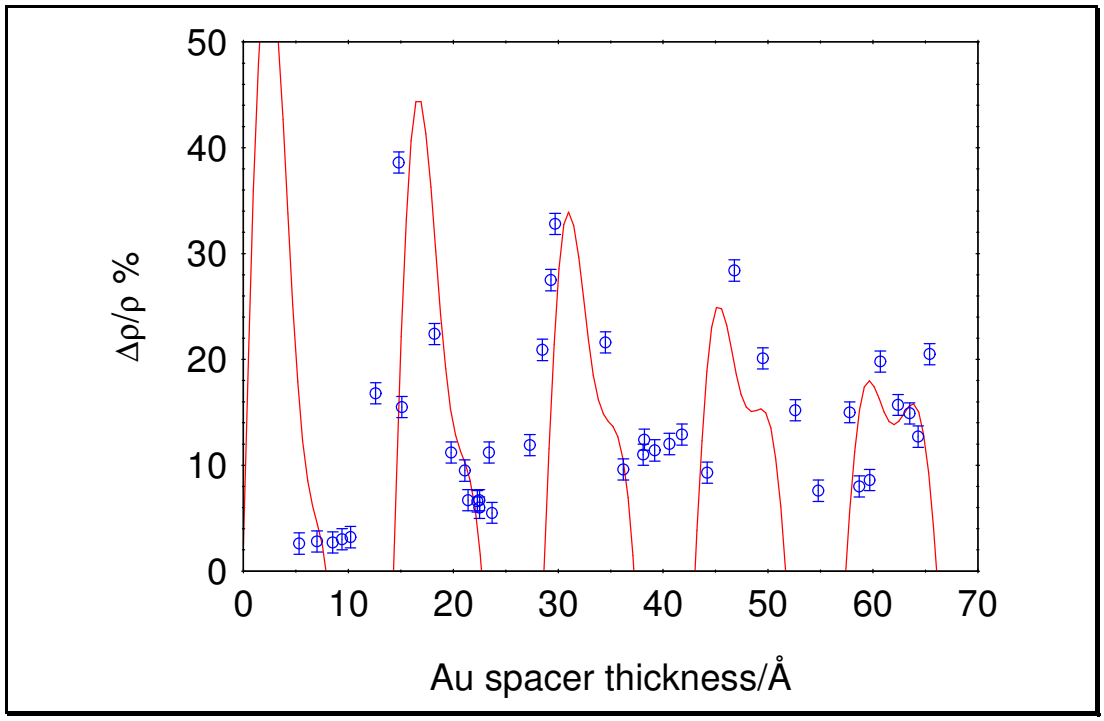

Figure 5.7: Oscillations in the GMR with a best fit function to determine the oscillation periods.

The best fit was obtained with two oscillation periods, determined to be 15±2Å and 7±2Å. This is the first observation of both periods in the GMR, and they are in reasonable agreement with the theory. Although they are not as accurate as the SEMPA analysis, they are comparable to the SMOKE studies. The comparison between periods assumes the bulk lattice parameter, which may not be a valid assumption for ultra-thin layers. There may be strain present at the interface, which could cause deviations away from the bulk Au parameter. The experimental work to determine accurately the coupling periods using magnetic methods utilised thick Au buffers, Fe or Au single crystal whiskers to reduce the effects of strain within the multilayers.

In chapter 4 it was shown that in Co/Cu multilayers the decrease of the GMR is proportional to the interface roughness within the multilayer. Therefore, a detailed x-ray study of the interfaces was required to determine whether the interface roughness was the cause of differences in the magneto-transport data between the two orientations. Due to the time-consuming nature of the x-ray characterisation, one sample of each orientation was chosen, with similar values of the spacer thickness.

5.7. X-Ray Characterisation using Synchrotron Radiation.

The x-ray data was collected at Station 2.3 Daresbury and Beamline 16.3 ESRF Grenoble, in collaboration with Prof. B.K. Tanner's group at Durham University. Low angle specular and transverse diffuse scatter was collected to determine the roughness and correlation length within the multilayer. The fits to the data were carried out by B.D. Fulthorpe at Durham, using the same code as was used in chapter 4.

5.7.1. Low Angle Reflectivity and Simulations.

The specular reflectivity data in Figure 5.1 clearly shows the presence of Kiessig fringes and Bragg peaks for both the MgO and sapphire substrates, from which the thickness of the layers can be immediately determined. The experimental data with the simulations for the specular scatter are shown in Figure 5.8 and the parameters for the fits in Table 5.1.

The specular scatter for the (100) orientation in Figure 5.8 is the true specular scatter, which is obtained by subtracting the longitudinal diffuse scatter from the specular scan. As the roughness is highly correlated, the Bragg peaks are spread into $\boldsymbol{q}_x$. This leads to large Bragg peaks in the diffuse scatter which, when subtracted from the specular scan can reduce the height of the Bragg peaks in the true specular scatter.

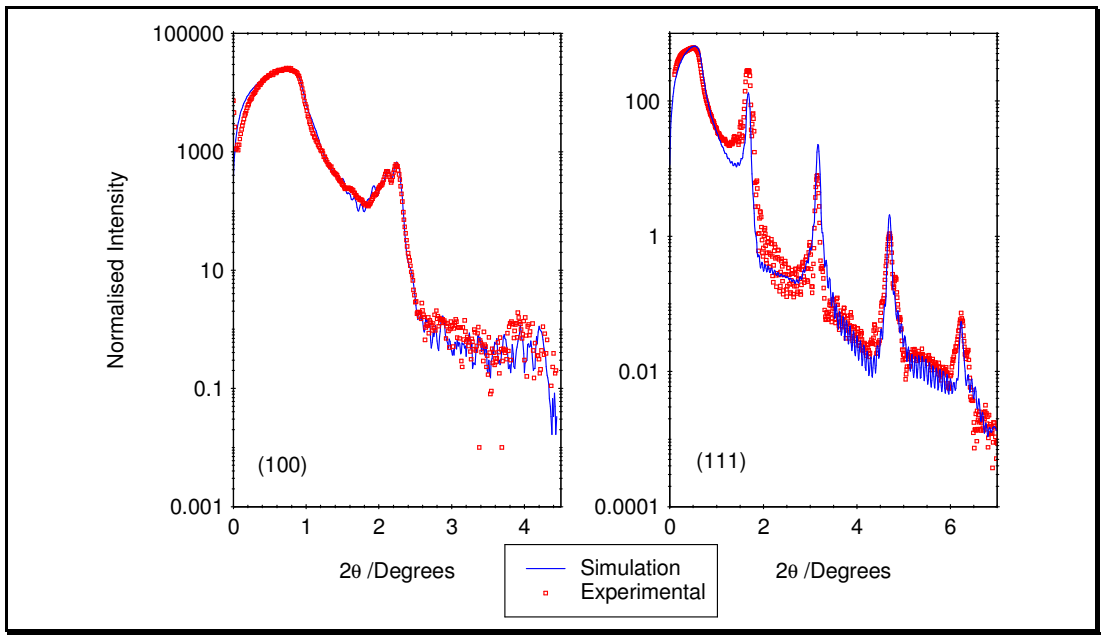

Figure 5.8: True specular scatter and simulations for each orientation ((100) (left) and (111) (right)).

The roughness at the Fe/Au interface within the multilayer was greater for the (100) samples than the (111). This gave an indication that the roughness at the interface was not responsible for the decrease in the GMR and the lack of oscillations in the AF-coupling in the (111) multilayers. Kiessig fringes and Bragg peaks were also observed in the off-specular (longitudinal diffuse) scans, which indicates that a large proportion of the interface roughness is correlated through the multilayer [30].

To obtain a quantitative comparison of the magnitude and nature of the roughness, the transverse diffuse scatter was simulated, again by B.D. Fulthorpe. These simulations gave values of the correlated and uncorrelated components of the interface roughness, and in addition the lateral correlation length and roughness exponent. Some of these simulations are shown in Figure 5.9.

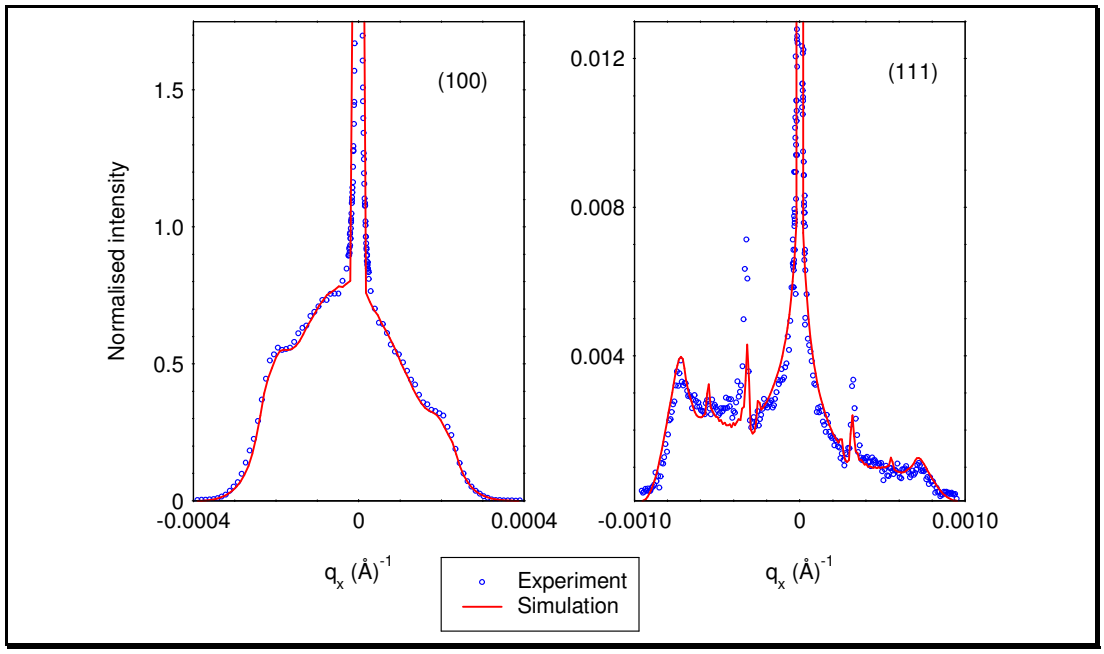

Figure 5.9: Transverse diffuse experimental data and simulations.

	t_{Fe}	t_{Au}	σ_c	σ_u	$\xi \pm 10$	$h \pm 0.05$
(100)	7.8	31.0	9.3	0.9	250	0.28
(111)	8.0	29.0	3.3	0.2	250	0.20

Table 5.1: Parameters from the x-ray simulations of Fe/Au multilayers.

The parameters, shown in Table 5.1, indicate that the roughness was highly correlated in both cases, as was expected from the off-specular scatter. The magnitude of the total roughness in the (100) system was much greater than the corresponding (111) multilayer, so the lower GMR in the (111) system could not be explained by an increase the interface roughness. However, the difference in the GMR between orientations is consistent with channelling theory. The magnitude of the roughness was greater than those found in Fe/Au(100) multilayers grown by other groups due to the thin buffers utilised to enable transport measurements. The correlation length of 250Å is consistent with that found by Paniago *et al* [126] of Fe/Au(100) multilayers deposited on MgO(001).

5.7.2. High Angle X-ray Diffraction.

High angle diffraction in the high resolution double-axis configuration was carried out on the same two samples as above to study the crystallinity and epitaxy of the multilayers. Scans in the specular condition and rocking curves at each satellite position were undertaken, and the FWHM of the zero order peaks in the diffraction scans, and of the rocking curves through these peaks, were determined to obtain values for the vertical and lateral grain sizes in each orientation. Figure 5.10 shows the high angle triple-axis scans carried out on the (100) and (111) orientations.

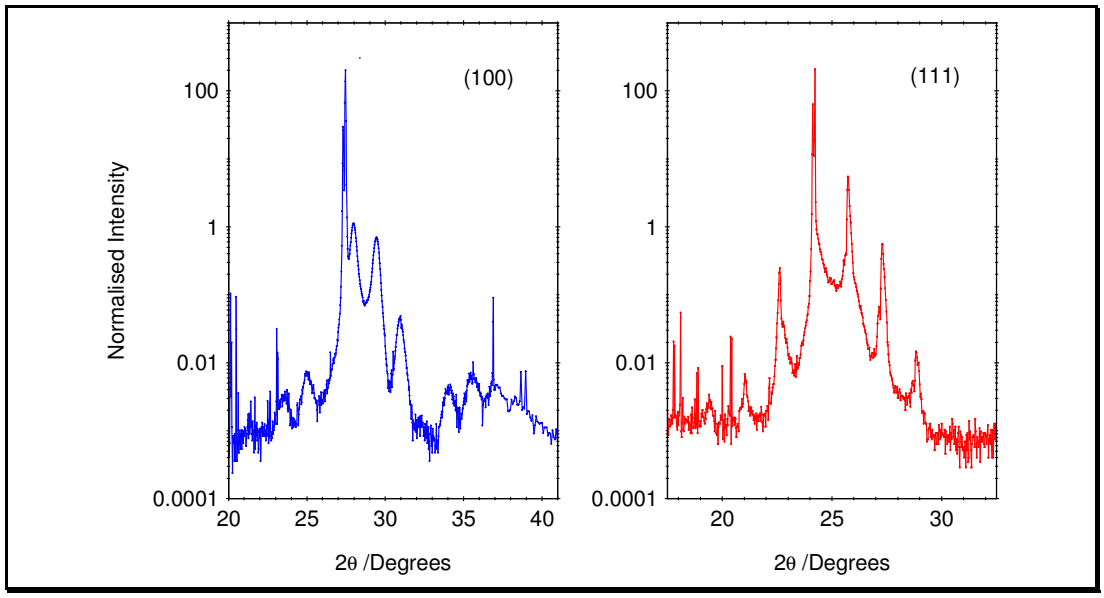

Figure 5.10: High angle triple-axis scans for the two orientations.

The large number of satellite orders and the positions of the zero order peaks in the triple-axis configuration confirmed that the multilayers were of the expected orientation, and the layers were of high epitaxial quality. The FWHM of the zero order peak in the $\theta/2\theta$ scan gave vertical grain sizes of 145±10Å and 590±30Å for the (100) and (111) orientations respectively. Lateral grain sizes, obtained from the FWHM of the rocking curves, were 130±10Å and 540±30Å for the (100) and the (111) multilayers respectively.

5.8. Saturation Conductivity.

Electron channelling should not only manifest itself in the GMR and coupling, but also in the saturated conductivity. As the channelling is due to the specular reflections of electrons at interfaces, this increases the effective mean-free path of the electron within the Au layer and hence the conductivity of the layer. This in turn should increase the conductivity of the (100) multilayers in comparison to the (111) system.

There are three possibilities for the magnitude of the mean-free-path within a multilayer
(i) comparable to a bilayer repeat period
(ii) much greater than the bilayer repeat period
(iii) less than an individual layer.
If the mean-free-path is comparable to the bilayer repeat, the resistances can be added in parallel to obtain the resistance of the multilayer. The conductivity is then the sum of the conductivities of each of the layers (20 Fe and 20 Au layers), weighted by the ratio of the Fe and Au layer thickness to the total thickness:

$$\sigma = \frac{20t_{Au}}{t_{tot}}\sigma_{F\,Au} + \frac{20t_{Fe}}{t_{tot}}\sigma_{F\,Fe} \quad \text{..... (5.3)}$$

where $\sigma_{F_{Au}}$ is the conductivity of the spacer layer. This expression does not fit the conductivity of either orientation, indicating that the mean-free-path is either shorter than the thickness of an individual layer, much greater than the total thickness of the multilayer or that the electrons are confined in some way to a layer within the multilayer. A short mean-free-path would lead to a very low conductivity, which is not observed here. If the mean-free-path is much larger than the multilayer, the resistance of

each layer could be added in series. However, this method does not fit the data either. This indicates that the electrons are confined to a layer that is acting as a low-resistance shunt.

The idea that the electrons are confined to a thin layer is analogous to Fuchs-Sondheimer theory. This was introduced by Fuchs [127] and modified by Sondheimer [128] to explain the variation of the resistivity with thickness of thin metallic films by considering scattering of electrons at boundaries within the film. In our case, the boundaries are the Fe layers either side of the Au spacer layer, and the conductivity of the Au layer can be approximated to [13]

$$\sigma_F \approx \frac{3\sigma_B t}{4\lambda_B}\ln\left(\frac{\lambda_B}{t}\right) \quad \text{..... (5.4)}$$

where σ_B is the bulk conductivity and λ_B the bulk mean-free-path. Although the mean-free-path may be long in these samples, the electrons are confined to the Au spacer for large distances, and so the electron still only samples a small number of bilayer repeats. This implies that the conductivity of the multilayer can be calculated by adding the resistance of each layer in parallel, but with modification to the conductivity of the Au spacer layer. Hence, the conductivity of the multilayer can be written as

$$\sigma \approx \frac{15\sigma_{B_{Au}}}{\lambda_{B_{Au}}}\frac{t_{Au}^2}{t_{tot}}ln\left(\frac{\lambda_{B_{Au}}}{t_{Au}}\right)+\frac{20t_{Fe}}{t_{tot}}\sigma_{F\,Fe} \quad \text{..... (5.5)}$$

This function fits both orientations well. However, from the fitting parameters, the mean-free-path in the (111) multilayers appears larger than the (100) multilayers, in direct contradiction to the measured resistivity. As this parameter is the bulk mean-free-path for Au, the value should be independent of orientation.

The above function assumes that the interfaces are diffuse, and there is no specular scatter at the Fe/Au interface [13]. To account for this, a phenomenological parameter, *N*, is introduced to gain insight into the relative number of specular reflections between orientations.

$$\sigma \approx \frac{15N\sigma_{B_{Au}}}{\lambda_{B_{Au}}}\frac{t_{Au}^2}{t_{tot}}ln\left(\frac{\lambda_{B_{Au}}}{t_{Au}}\right)+\frac{20t_{Fe}}{t_{tot}}\sigma_{F\,Fe} \quad \text{..... (5.6)}$$

The (111) orientation was assumed to exhibit no specular reflections, so *N* was set equal to 1. This fitting determined the mean-free-path of the electron in bulk Au to be 8400±200Å at 4.2K. This value for the bulk Au mean-free-path was then fixed in the simulation of the (100) orientation, to obtain a value for *N* in these multilayers. This method yielded a value of *N=2.6±0.1*, indicating that the differences in the conductivity are consistent with specular reflections at the Au/Fe(100) interface, with a ratio of specular reflections between orientations of 2.6±0.1. The conductivity as a function of the Au spacer thickness and the fits to the data using this model are shown in Figure 5.11.

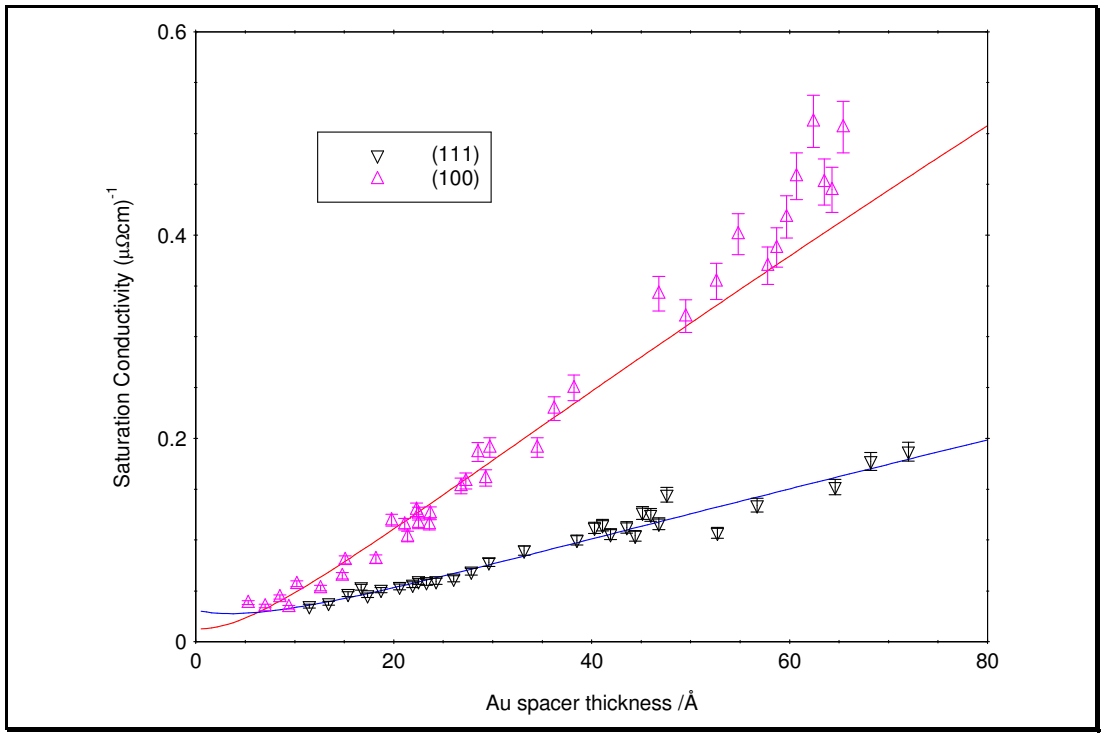

Figure 5.11: Conductivty of the two orientations with fits to the data using model 1.

An alternative model of the conductivity is to attempt to compare the mean-free-paths in the Au layers of each orientation. For thin layers of Au, the mean-free-path within the layer is dependent on the thickness of the layer, and the number of specular reflections of the electrons at the interface, such that $\lambda_{Au} = Nt_{Au}$. N is a constant, dependent on the number of specular reflections, and a geometrical term dependent on the angle of incidence of the electrons within the layer. This geometrical term will be the same for both orientations, so the ratio of the values of N for each orientation will be a direct measure of the ratio of specular reflections in the two systems. From equation 5.3, and using the Drude free-electron model for the conductivity of the layer, the multilayer conductivity becomes

$$\sigma = \frac{20ne^2 Nt_{Au}^2}{mv_f t_{tot}} + \frac{20t_{Fe}}{t_{tot}}\sigma_{F\,Fe} \quad \text{..... (5.7)}$$

The value of $\frac{20ne^2}{mv_f}$ was assumed constant between orientations.

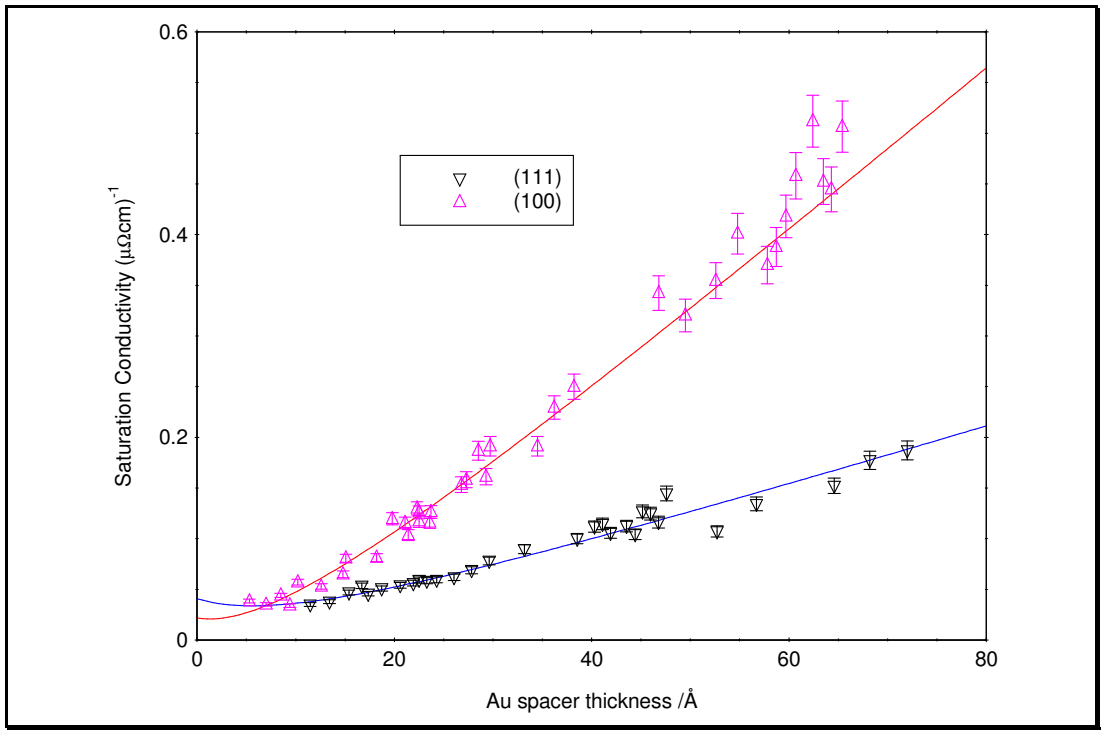

Figure 5.12: Fits to the saturation conductivity using model 2.

Figure 5.12 shows the fits to the data using this model. The fits are surprisingly good, given the simplicity of the model. The value of *N*, which gives the ratio of specular reflections between orientations, is 2.7±0.1, in excellent agreement with the fits using the other model.

In both models, the conductivity without spacers is higher for the (111) than the (100), indicating the combined resistivity of the Fe and buffer layers in the (100) is higher than in the (111) multilayers. This may be due to the smaller grains in the (100) multilayers.

5.9. Discussion.

The magnitude of the conductivity is greater in the (100) compared to the (111) multilayers. These differences could be attributed to three main differences between orientations; (i) roughness of the interfaces, (ii) Au structure or (iii) electron channelling. Any changes in the Fe structure would cause an off-set in the conductivity curves, but the gradients would remain the same for the thicker spacer layers.

An increase in interface roughness would increase the amount of electron scattering, hence decreasing the conductivity. From the low angle reflectivity, the interface roughness in the (100) is a factor of three higher than the (111) multilayers, so the differences in the roughness cannot explain the conductivity data. The correlation length in both orientations was 250Å. The magnitude of the roughness on this length-scale should not affect the specularity of the electrons at the interface.

At low temperatures defect scattering will be dominated by scattering at grain boundaries. If the size of the grains decrease, the increase in grain boundary scattering tends to decrease the conductivity [129]. Bobo *et al* [130] attributed the high resistivity of their Co/Cu multilayers to a grain size of only 20Å, compared to other materials of larger grain-size and lower resistivity. Modak *et al* [78] investigated the effect of grain

size on the GMR in Co/Cu multilayers for grain sizes of 150Å and 300Å, and found small increases in the GMR with grain size, with a corresponding small decrease in the resistivity. Bailey *et al* [131] investigated the effect of the grain size on the GMR and resistivity in top spin-valves. In addition to this, they analysed the variation of the resistivity in Cu layers with varying grain size. They found a strong correlation between grain size and both the GMR in the spin valves, and the resistivity in both systems. In both systems, the resistivity increased with decreasing grain size, with a reduced GMR in the spin-valves for smaller grains.

A comparison of the grain sizes in the two orientations gives an indication of the comparative amounts of defect scattering in the Au spacer layers, and whether these can explain the differences in conductivity. These grain sizes were obtained from both specular and diffuse scatter in the high angle geometry. The grain size in the (111) was 590±30Å normal and 540±30Å parallel to the plane of the sample. In the (100) system, the grain sizes were 145±10Å normal and 130±10Å parallel to the plane. The samples with the higher conductivity have grain sizes ¼ of the size of those in the samples with lower conductivity. Clearly, the differences in the conductivity are not due to more electron scattering within the Au spacer layer. This leads to the conclusion that the differences in the saturation conductivity can be attributed to electron channelling in the (100) multilayers, with a ratio of specular reflections between the (100) and (111) multilayers as 2.6±0.1.

Oscillations in the GMR and the remanence in the MOKE hysteresis loops have revealed oscillations in the AF-coupling in the (100) multilayers, but the same effect was not observed in the (111) system. The GMR oscillations have been modelled using two oscillation periods, which has previously been observed in magnetic studies, but not in the GMR. The periods determined are in reasonable agreement with other experimental results. These oscillations, and the large GMRs observed in the (100), are all predicted by the spin asymmetry in the reflection coefficients.

5.10. Summary.

The purpose of this experiment was to find experimental evidence for electron channelling in magnetic multilayers. Theoretical calculations predict that Fe/Au(100) is a system in which there should be strong electron channelling, whereas in Fe/Au(111) the same effect should not be observed [65]. A detailed study of the two orientations of the Fe/Au multilayers was undertaken to uncover evidence for electron channelling. It has been found that the transport, structural and magnetic properties of the systems vary. The GMR exhibits oscillations in the (100) but not in the (111) orientation, the conductivity is much increased and the interface roughness is increased. The changes in the conductivity are attributed to electron channelling in Fe/Au(100). With improved interface quality, the magnitude of the GMR may be increased further as the channelling becomes more effective.

Chapter 6: Summary of Results and Further Plans.

6.1. Summary of Results.

The main aim of this thesis was to investigate the role of the interface on the magnitude of the GMR in different magnetic multilayers grown by MBE. Co/Cu(111), Fe/Au(100) and Fe/Au(111) multilayers have been prepared by MBE and the electron transport, magnetic and structural properties of these multilayers have been investigated utilising a range of techniques. In Co/Cu(111) multilayers, it has been shown that the magnitude and type of interface roughness plays an important role in the magnitude of the GMR. However, in Fe/Au multilayers, the predominant factor in the magnitude of the GMR is not so much the magnitude of the interface roughness, but the crystallographic orientation of the multilayer itself. The (100) orientation was the favoured orientation for high GMR and conductivity values.

In chapter 4, Co/Cu(111) multilayers were grown at different substrate temperatures, in order to vary the interface roughness in the resulting multilayers. The GMR, resistivity and MOKE hysteresis loops were measured for each sample. Decreasing the deposition temperature of the multilayer caused an increase in the GMR. The saturation field in the GMR indicated changes in the AF-coupling at low temperatures. However, these changes were not replicated in the room temperature MOKE. This discrepancy may be due to the different experimental temperatures.

Simulations of the grazing incidence specular and transverse diffuse scans were undertaken using commercially available software. The parameters obtained were used, in conjunction with parameters from analysis of the high angle x-ray diffraction, to explain the differences in the transport properties in terms of changes in the structure.

The structural analysis revealed several interesting features. In all of the samples, the roughness was highly correlated, and the magnitude of the correlated roughness component was inversely proportional to the GMR. The uncorrelated component of the roughness did not appear to affect the magnitude of the GMR.

Another characteristic of these samples was the presence of two length-scales within the multilayer: (i) a long length-scale was associated with the Cu buffer layer and (ii) a short correlation length associated with the island growth of Co. The sample with the longest correlation length exhibited the largest GMR, highlighting the importance of the quality of the buffer layer in producing a large GMR. Changing the deposition temperature of the buffer layer caused a change in the GMR. However, even when the buffer layer was deposited at the same temperature in two different samples but the multilayer deposition temperature was altered, the long correlation length associated with the buffer layer changed. This may indicate the quality of the buffer was not only affected by its deposition temperature, but on the temperature the buffer was cooled to before the deposition of subsequent layers. The short correlation length was attributed to the size of the islands formed by the Co during growth, and the magnitude of this correlation length was proportional to the GMR.

In chapter 5, the effect of the orientation of Fe/Au multilayers on the electron transport properties was studied. The main aim of these experiments was to gather evidence for electron channelling in Fe/Au(100) multilayers. The simulations of the low angle x-ray scans, and high angle x-ray diffraction scans indicated that the Au layers in both systems were of good epitaxial quality. Again, the interface roughness in both systems was highly correlated, but the magnitude of the roughness in the (100) system was three times greater than that in the (111). Both the vertical and lateral grain sizes in the (111) orientation were greater than in the (100) multilayers.

From differences in the structure, it was expected that the GMR and conductivity in the (111) multilayers would be higher. The conductivity was expected to be a function of the spacer thickness in each case, as the spacer thickness was less than the bulk mean-free-path of the electrons. However, as the Au spacer thickness was increased, the conductivity and the rate of increase of the conductivity in the (100) was three times greater than that of the (111). This difference in the conductivity could not be attributed to differences in the structural quality of the interfaces or the layers. Therefore, this must be due to specular reflections of electrons at the Au/Fe(100) interface within the multilayer.

Another consequence of the specular reflections was the enhancement of the GMR in equivalently coupled samples. In addition to this enhancement, oscillations were observed in the AF-coupling of the (100) samples, which was modelled using two periods in reasonable agreement with the theory and other experimental work performed on these types of samples by other authors.

6.2. Further Plans.

Work is already underway on the characterisation of thin Fe layers on Au(111), to determine the growth mode and structure of the initial monolayers of this system. This work is being carried out by D. Dekadjevi at the University of Leeds, using in-situ RHEED analysis, and B.D. Fulthorpe using grazing incidence x-ray diffraction to determine the in-plane lattice structure.

To confirm electron channelling is present in the Fe/Au(100) system, trilayers of Fe/Au/Fe(100) and Fe/Au/Co(100) will be deposited, and the saturation conductivity of each type of sample measured as a function of spacer thickness. The quality of Au in each sample should be identical, as identical growth procedures will be used until the deposition of the final layer. However, the Au/Co(100) interface is not expected to reflect the electrons as efficiently as the Au/Fe(100) interface. If specular reflections are the mechanism for the high conductivity in the Fe/Au(100) multilayers, the saturation conductivity in the Fe/Au/Co should be lower compared to the Fe/Au/Fe trilayer.

Another experiment to confirm the presence of electron channelling is being undertaken, using Fe/Au multilayers but with the GMR measured in the CPP geometry, where the current is passed perpendicular to the layers. Rather than measuring the reflection probabilities of the electrons, this technique can study the transmission probability of the electron at the interface. However, if there is a large spin asymmetry in the reflection there must be, by definition, the same asymmetry in the transmission probabilities, and the same effects on the GMR and conductivity should be observed. This work is being undertaken by D. Bozec at the University of Leeds.

Systematic studies of the effect of roughness on the GMR using several complementary characterisation techniques, as shown in chapter 4, are rare. In previous studies on multilayers, results concerning the effects of interface roughness are contradictory. However, most studies utilised only the specular x-ray scatter to extract roughness parameters, which is not sufficient to obtain reliable results. By implementing a detailed study, using specular and diffuse scatter at both low and high angles, the interface morphology could be extracted. Differences in the interface morphology could then be related to any changes in the electron transport measurements.

References.

[1] Grazing Incidence X-Ray Analysis, Bede Scientific (1995).

[2] C.F. Majkrzak, J.W. Cable, J. Kwo, M. Hong, D.B. McWhan, Y. Yafet, J.V. Waszczak and C. Vettier, Phys. Rev. Lett. **56**, 2700 (1986).

[3] M.N. Baibich, J.M. Broto, A. Fert, F. Nguyen Van Dau, F. Petroff, P. Etienne, G. Creuzet, A. Friederich and J. Chazelas, Phys. Rev. Lett. **61**, 2472 (1988).

[4] P.M. Levy, S. Zhang and A. Fert, Phys. Rev. Lett. **65**, 1643 (1990).

[5] *http://www.ibm.com/*

[6] *http://www.nve.com/*

[7] C.H. Marrows, *PhD Thesis*, University of Leeds (1997).

[8] T.P.A. Hase, I. Pape, B.K. Tanner, H. Laidler, P. Ryan and B.J. Hickey, J. Magn. Magn. Mater. **177-181**, 1164 (1998).

[9] *Binary Phase Diagrams*, ed. T.B. Massalski (ASM International, CITY, 1990), Vol.2 p. 1189.

[10] P. Bödecker, A. Abromeit, K. Bröhl, P. Sonntag, N. Metoki and H. Zabel, Phys. Rev. B **47**, 2353 (1993).

[11] M. Safa and B.K. Tanner, J. Magn. Magn. Mater. **150**, L290 (1995).

[12] R.Q. Hood and L.M. Falicov, Phys. Rev. B **46**, 8287 (1992).

[13] K.L. Chopra, *Thin Film Phenomena*, (Robert E. Krieger Publishing Company, New York, 1979) and references therein.

[14] M.D. Stiles, J. Appl. Phys. **79**, 5805 (1996).

[15] C. Kittel, *Introduction to Solid State Physics*, (John Wiley & Sons, 1996).

[16] B. Lengeler, *Photoemission and Absorption Spectroscopy of Solids and Interfaces with Synchrotron Radiation*, p157, eds M Campagna and K Rosei, (North Holland, 1990).

[17] P. Lee, Optics Commun. **43** 237 (1982).

[18] A. Segmüller, Thin Solid Films **18**, 287 (1973).

[19] K. Temst, M.J. Bael, B. Wuyts, C. Van Haesendonck, Y. Bruynseraede, D.G. De Groot, N. Koeman and R.P. Griessen, Appl. Phys. Lett. **67**, 3429 (1995).

[20] M. Wormington, I. Pape, T.P.A Hase, B.K. Tanner and D.K. Bowen, Phil. Mag. Letters **74**, 211 (1996).

[21] Y. Waseda, *Novel Application of Anomalous (Resonance) X-ray Scattering for the Structural Characterisation of Disordered Materials*, (Springer, Berlin, 1984).

[22] N. Nakayama, I Moritani, T. Shinjo, Y. Fujii and S. Sasaki, J. Phys. F: Met. Phys. **18**, 429 (1988).

[23] M. Wormington, XAFS, Bede Scientific (1995).

[24] B.D. Cullity, *Advances in X-ray Diffraction*, (Addison-Wesley Publishing Company, 1956).

[25] M.J. Hall, *PhD Thesis*, University of Leeds (1993).

[26] C.C. Tang, M. Miller, D. Laundy, *Station 2.3 Manual*, CCLRC Daresbury Laboratory.

[27] S. Cockerton and B.K. Tanner, *Advances in X-ray Analysis* **38**, p371 (Plenum Press, New York, 1995).

[28] I. Pape, *PhD Thesis*, Durham University (1997).

[29] D.E. Savage, N. Schimke, Y.-H. Phang and M.G. Lagally, J. Appl. Phys. **71**, 3283 (1992).

[30] V. Holý, J. Kubena, I. Ohlídal, K. Lischka and W. Plotz, Phys. Rev. B **47**, 15896 (1993).

[31] Y. Yoneda, Phys. Rev. **131**, 2010 (1963).

[32] L.G. Parrat, Phys. Rev. **95**, 359 (1954).

[33] J.M. Eastman, Phys. Thin Films **10**, 167 (1978).

[34] L. Névot and P. Croce, Rev. Phys. Appl. **15**, 761 (1980).

[35] S.K. Sinha, E.B. Sirota, S. Garoff and H.B. Stanley, Phys. Rev. B **38**, 2297 (1988).

[36] B.B. Mandelbrot, *The Fractal Geometry of Nature*, (Freeman, New York, 1982).

[37] T. Salditt, T.H. Metzger, Ch. Brandt, U. Klemradt and J. Peisl, Phys. Rev. B **51**, 5617 (1995).

[38] M. Wormington, *PhD Thesis*, University of Warwick.

[39] D.K.G. de Boer, Phys. Rev. B **49**, 5817 (1994).

[40] J. Kwo, D.B. McWhan, M. Hong, E.M. Gyorgy, L.C. Feldman and J.E. Cunningham, *Layered Structures, Epitaxy and Interfaces*, eds. J.M. Gibson and L.R. Dawson, MRS Symposia Proceeding No. 37 (Materials Research Society, Pittsburgh, 1985).

[41] A. Schreyer, K. Brohl, J.F. Ankner, C.F. Majkrzak, T. Zeidler, P. Bodeker, N. Metoki and H. Zabel, Phys. Rev. B **47**, 15334 (1993).

[42] V. Holý and T. Baumbach, Phys. Rev. B **49**,10668 (1994).

[43] D.E. Savage, J. Kleiner, N. Schimke, Y.-H. Phang, T. Jankowski, J. Jacobs, R. Karotis and M.G. Lagally, J. Appl. Phys. **69**, 1411 (1991).

[44] M.A. Rudderman and C. Kittel, Phys. Rev. **96**, 99 (1954).

[45] T. Kasuya, Prog. Theoret. Phys. (Kyoto) **16**, 45 (1956).

[46] K. Yosida, Phys. Rev. **106**, 893 (1957).

[47] S.S.P. Parkin, N. More and K.P. Roche, Phys. Rev. Lett **64**, 2304 (1990).

[48] S.S.P. Parkin, R. Bhadra and K.P. Roche, Phys. Rev. Lett **66**, 2152 (1991).

[49] N.F. Mott, Adv. Phys. **13**,325 (1964).

[50] J. Mathon, Contemp. Phys. **32**, 143 (1991).

[51] V.L. Moruzzi, J.F. Janak and A.R. Williams, *Calculated Electronic Properties of Metals*, (Permagon Press, New York, 1978).

[52] P.M. Levy, J. Magn. Magn. Mater. **140**, 485 (1995).

[53] J. Ben Youssef, K. Bouziane, O. Koshkina, H. Le Gall, M. El Harfaoui, M. El Yamani, J.M. Desvignes and A. Fert, J. Magn. Magn. Mater. **165**, 288 (1997).

[54] H. Ueda, O. Kitakami, Y. Shimada, Y. Goto and M. Yamamoto, Jpn. J. Appl. Phys. **33**, 6173 (1994).

[55] S.S.P. Parkin, Section 2.4 in *Ultrathin Magnetic Structures II*, eds. B. Heinrich and J.A.C. Bland, (Springer-Verlag, Berlin, 1994).

[56] S.S.P. Parkin, Phys. Rev. Lett. **67**, 3598 (1991).

[57] J. Unguris, R.J. Celotta and D.T. Pierce, Phys. Rev. Lett. **67**, 140 (1991).

[58] J. Unguris, R.J. Celotta and D.T. Pierce, J. Appl. Phys. **75**, 6437 (1994).

[59] R. Coehoorn, Phys. Rev. B **44**, 9331 (1991).

[60] P. Bruno and C. Chappert, Phys. Rev. Lett. **67**, 1602 (1991).

[61] M.D. Stiles, Phys. Rev. B **48**, 7238 (1993).

[62] Y. Kawawake and H. Sakakima, J. Magn. Magn. Mater. **184**, 49 (1998).

[63] W.F. Egelhoff, P.J. Chen, C.J. Powell, M.D. Stiles, R.D. McMichael, J.H. Judy, K. Takano, A.E. Berkowitz and J.M. Daughton, I.E.E.E. Trans. Mag. **33**, 3580 (1997).

[64] H.J.M. Swagten, G.J. Strijkers, P.J. Bloemen, M.M.H. Wilekens and W.J.M. de Jonge, Phys. Rev. B **53**, 9108 (1993).

[65] M.D. Stiles, *private communication*.

[66] M.J. Hall, *PhD Thesis*, University of Leeds (1993).

[67] N.J. Flynn, *PhD Thesis*, University of Leeds (1996).

[68] S.D. Bader, J. Magn. Magn. Mater. **100**, 440 (1991).

[69] S.D. Bader and J.L. Erskine, Chapter 4 in *Ultrathin Magnetic Structures II*, eds. Bland and Heinrich, (Springer-Verlag, 1994).

[70] H. Laidler*, PhD Thesis*, University of Leeds (1997).

[71] G.R. Harp, S.S.P. Parkin, R.F.C. Farrow, R.F.Mars, M.F. Toney, Q.H. Lam, T.A. Rabedeau and R.J. Savoy, Phys.Rev. B **47**, 8721 (1993).

[72] R.J. Highmore, W.C. Shih, R.E. Somekh and J.E. Evetts, J. Magn. Magn. Mater. **116**, 249 (1992).

[73] H. Kano, K. Kagawa, A. Suzuki, A. Okabe, K. Hayashi and K. Aso, Appl. Phys. Lett. **63**, 2839 (1993).

[74] F. Yoshizaki and T. Kingetsu, Thin Solid Films **239**, 229 (1994).

[75] T. Kingetsu and F. Yoshizaka, Jpn. J. Appl. Phys. **33**, 6168 (1994).

[76] M. Suzuki, Y. Taga, A. Goto and H. Yasuoka, J. Magn. Magn. Mater. **126**, 495 (1993).

[77] A. Oguri, Y. Asano and S. Maekawa, J. Phys. Soc. Japn. **61**, 2652 (1992).

[78] A.R. Modak, D.J. Smith and S.S.P. Parkin, Phys. Rev. B **50**, 4232 (1994).

[79] Z.J. Yang and M.R. Scheinfein, Phys. Rev. B **52**, 4263 (1995).

[80] M.A. Howson, B.J. Hickey, J. Xu, D. Greig and N. Wiser, Phy. Rev. B **48**, 1322 (1993).

[81] J. Xu, B.J. Hickey, M.A. Howson, D. Greig, M.J. Walker and N. Wiser, J. Magn. Mag. Mat. **156**, 69 (1996).

[82] D.E. Savage, N. Schimke, Y.-H. Phang and M.G. Lagally, J. Appl. Phys. **71**, 3283 (1992).

[83] H. Laidler, I. Pape, C.I. Gregory, B.J. Hickey and B.K. Tanner, J. Magn. Magn. Mater. **154**, 165 (1996).

[84] A. Gibaud, R.A. Cowley, D.F. McMorrow, R.C.C. Ward and M.R. Wells, Phys. Rev. B **48**, 14463 (1993).

[85] E.E. Fullerton, I.K. Schuller, H. Vanderstraeten and Y. Bruynseraede, Phys. Rev. B **45**, 9292 (1992).

[86] T. Gu, A.I. Goldman and M. Mao, Phys. Rev. B **56**, 6474 (1997).

[87] P. Weinberger, V. Drchal, L. Szunyogh, J. Fritscher, B.I. Bennet, Phys. Rev. B **49**, 13366 (1994).

[88] W.B. Pearson, *Lattice Spacings and Structures of Metals and Alloys*, (Pergamon, London, 1958).

[89] K.Y. Kok, M.J. Hall and J.A. Leake, J. Magn. Magn. Mater. **156**, 51 (1996).

[90] T.P.A. Hase, *PhD Thesis*, University of Durham (1998).

[91] S. Di Nunzio, K. Theis-Bröhl and H. Zabel, Thin Solid Films **279**, 180 (1996).

[92] P.F. Miceli, C.J. Palstrøm, Phys. Rev. B **51** (8), 5506-5509 (1995)

[93] C. Christides, S. Stavroyiannis, N. Boukos, A. Travlos and D. Niarchos, J. Appl. Phys. **83**, 3724 (1998).

[94] D.J. Smith, A.R. Modak, T.A. Rabedeau and S.S.P. Parkin, Appl. Phys. Lett. **71**, 1480 (1997)

[95] J.D. Kim, A.K. Petford-Long, J.P. Jakubovics, J.E. Evetts and R. Somekh, J. Appl. Phys. **76**, 2387 (1994).

[96] Y. Saito, K. Inomata, M. Nawate, S. Honda, A. Goto and H. Yasuoka, Jpn. J. Appl. Phys. **34**, 3088 (1995).

[97] R. Clarke, D. Barlett, F. Tsui, B. Chen and C. Uher, J. Appl. Phys. **75**, 6174 (1994).

[98] J.D.E. Castro, J. Mathon, M. Villeret and A. Umerski, Phys. Rev. B **53**, 13306 (1996).

[99] N. Perat and A. Dinia, Phys. Rev. B. **56**, 2676 (1997).

[100] L. Gonzalez, R. Miranda, M. Salmerón, J.A. Vergés and F. Ynduráin, Phys. Rev. B **24**, 3245 (1981).

[101] M.Ø. Pederson, I.A. Bönicke, E. Lægsgaard, I. Stensgaard, A. Ruban, J.K. Nørskov and F. Besenbacher, Surface Science **387**, 86 (1997).

[102] Th. Eckl, G. Reiss, H. Brückl and H. Hoffmann, J. Appl. Phys. **75**, 362 (1994).

[103] C. Prieto, R. Castañer, J.L. Martínez, A. de Andrés, J. Trigo and J.M. Sanz, J. Magn. Magn. Mater. **161**, 31 (1996).

[104] J. de la Figuera, J.E. Prieto, C. Ocal and R. Miranda, Phys. Rev. B **47**, 13043 (1993).

[105] M.T. Kief and W.F. Egelhoff, Phys. Rev. B **47**, 10785 (1993).

[106] K. Shintaku, Y. Daitoh and T Shinjo, Phys. Rev. B **47**, 14584 (1993).

[107] M. Hayashi, T. Katayama, Y. Suzuki, M. Taninaka, A. Thiaville and W. Geerts, J. Magn. Magn. Mater. **126**, 547 (1993).

[108] N. Nakayama, T. Okuyama and T. Shinjo, J. Phys.: Cond. Matter **5**, 1173 (1993).

[109] T. Okuyama, Jpn. J. Appl. Phys. **30**, 2053 (1991).

[110] T. Kawagoe, K. Nakamura, T. Terashima, H. Kaihoko and T. Mizoguchi, J. Magn. Magn. Mater. **148**, 185 (1995).

[111] R. Germar, W. Dürr, J.W. Krewer, D. Pescia and W. Gurdat, Appl. Phys. A **47**, 393 (1988).

[112] S.D. Bader and E.R. Moog, J. Appl. Phys. **61**, 3729 (1987).

[113] Y.L. He and G.C. Wang, Phys. Rev. Lett. **71**, 3834 (1993).

[114] W.F. Egelhoff, Jr., P.J. Chen, C.J. Powell, M.D. Stiles, R.D. McMichael, C.-L. Lin, J.M. Sivertsen, J.H. Judy, K. Takano and A.E. Berkowitz, J. Appl. Phys. **80**, 5183 (1996).

[115] T. Okuyama, Japn. J. Appl. Phys. **30**, 2053 (1991).

[116] J.C. Walker, H. Tang, M.D. Wieczorek, D.J. Keavney, D.F. Storm, C.J. Utierrez and Z.Q. Qiu, Hyperfine Interactions **68**, 271 (1991).

[117] J. Xu, M.A. Howson, P. Hucknall, B.J. Hickey, R. Venkataraman, C. Hammond, M.J. Walker and D. Greig, J. Appl. Phys. **81**, 3908 (1997).

[118] B. Voigtlander, G. Meyer and N.M. Amer, Surf. Sci. **255**, L529 (1991).

[119] M.T. Kief and W.F. Egelhoff, J. Vac. Sci. & Tech. A **11**, 1661 (1993).

[120] K. Shintaku, N. Hosoito and T Shinjo, J. Magn. Magn. Mater. **121**, 413 (1993).

[121] S. Honda, K. Koguma and M. Nawate, J. Appl. Phys. **82**, 4428 (1997).

[122] E.R. Moog, S.D. Bader and J. Zak, Appl. Phys. Lett. **56**, 2687 (1990).

[123] Q. Leng, V. Cros, R. Schäfer, A. Fuß, P. Grünberg and W. Zinn, J. Magn. Magn. Mater. **126**, 367 (1993).

[124] Y. Suzuki, T. Katayama, P. Bruno, S. Tuasa and E. Tamura, Phys. Rev. Lett. **80**, 5200 (1998).

[125] J. Unguris, R.J. Celotta and D.T. Pierce, J. Magn. Magn. Mater. **127**, 205 (1993).

[126] R. Paniago, R. Forrest, P.C. Chow, S.C. Moss, S.S.P. Parkin and D. Cookson, Phys. Rev. B **56**, 13442 (1997).

[127] K. Fuchs, Proc. Cambridge Phil. Soc. **34**, 100 (1938).

[128] F.H. Sondheimer, Phys. Rev. **80**, 401 (1950).

[129] A.F. Mayadas and M. Shatzkes, Phys. Rev. B **1**, 1382 (1970).

[130] J.F. Bobo, B. Baylac, L. Hennet, O. Lenoble, M. Piecuch, B. Raquet and J.C. Ousset, J. Magn. Magn. Mater. **121**, 291 (1993).

[131] W.E. Bailey, D. Guarisco and S.X. Wang, I.E.E.E. Trans. Mag. **34**, 957 (1998).